Demonstration of a
Dual Atom Trap Trace Analysis
Setup for ^{39}Ar and ^{85}Kr

single ^{39}Ar atom

triple ^{85}Kr atom

Lisa Elfriede Ringena

Issued 2021

Dissertation

submitted to the

Combined Faculties of the Natural Sciences and Mathematics

of the Ruperto-Carola University of Heidelberg, Germany

for the degree of

Doctor of Natural Sciences

Put forward by

Lisa Elfriede Ringena

born in Emden, Germany

Oral examination: 20 July 2021

Demonstration of a
Dual Atom Trap Trace Analysis
Setup for ^{39}Ar and ^{85}Kr

Referees: Prof. Dr. Markus K. Oberthaler
           Prof. Dr. Norbert Frank

Demonstration of a Dual Atom Trap Trace Analysis Setup for ^{39}Ar and ^{85}Kr

Atom Trap Trace Analysis (ATTA) detects rare isotopes within a huge background of abundant ones by exploiting specific optical transition frequencies of the desired atoms. ATTA utilizes the high number of photon-scattering processes in a magneto-optical trap for a distinct capture of the desired isotope alone. The Heidelberg ATTA collaboration successfully employed this technique on the environmental tracer ^{39}Ar. This thesis demonstrates the first setup of a dual ATTA (D-ATTA) experiment for the two radio-isotopes ^{39}Ar and ^{85}Kr. The measurement of both tracers within a short time span enables a more thorough study of an environmental sample. In the course of 24 h, count rates of 1420(40) a/h for ^{85}Kr and 1.8(3) a/h for ^{39}Ar were obtained with a sample volume of 60 μL and 600 μL, respectively. These results demonstrate the feasibility of radio-isotope dating of both tracers within short times in the same apparatus and sample. Improvements to the vacuum system enabled a count rate of 140 a/h for 1 μL krypton gas which corresponds to a 10 L water sample. Additionally, this thesis presents ^{39}Ar detection in a new dating facility. This second apparatus was built up to increase sample throughput and evolve the machine to a more modular and robust design.

Demonstration eines dualen Atom Trap Trace Analysis Aufbaus für ^{39}Ar und ^{85}Kr

Atom Trap Trace Analysis (ATTA) detektiert seltene Isotope vor einem riesigen Hintergrund häufiger Isotope und nutzt dabei spezifische Übergangsfrequenzen in den gewünschten Atomen aus. ATTA verwendet die hohe Anzahl von Photonenstreuprozessen in einer magneto-opischen Falle für ein selektives Fangen des gewünschten Atoms. Die Heidelberger ATTA Kollaboration hat diese Technik bereits erfolgreich auf den umweltphysikalischen Tracer ^{39}Ar angewandt. Diese Arbeit zeigt die erste Umsetzung eines dualen ATTA (D-ATTA) Experiments für die zwei Radioisotope ^{39}Ar und ^{85}Kr. Das Messen beider Tracer in einer kurzen Zeitspanne ermöglicht eine detailliertere Studie einer umweltphysikalischen Probe. Innerhalb von 24 h wurden dabei Zählraten von 1420(40) a/h für ^{85}Kr und 1.8(3) a/h für ^{39}Ar erzielt, bei einem Probenvolumen von 60 μL, beziehungsweise 600 μL. Diese Ergebnisse demonstrieren die Durchführbarkeit der Radioisotopendatierung mit zwei Tracern innerhalb der gleichen Probe und Anlage und in einer kurzen Zeitspanne. Verbesserungen am Vakuumsystem ermöglichten eine Zählrate von 140 a/h für 1 μL Krypton Gas, welches einer Wassermenge von 10 L entspricht. Zusätzlich wird in dieser Arbeit die Detektion von ^{39}Ar in einer neuen Datierungs-Anlage präsentiert. Der Aufbau dieser zweiten Maschine dient dem Erhöhen des Probendurchflusses und der Weiterentwicklung des Geräts zu einem modulareren, robusteren Design.

Contents

Preface

Laser cooling and trapping of atoms is a widely used technique in experimental atomic physics. This optical cooling is based on the manipulation of atoms with light quanta, photons, which carry a momentum proportional to their wavelength. In 1887, Heinrich Hertz was the first to study the effects of photons on charged objects [1], in 1921, Albert Einstein was awarded with the Nobel Prize for the theoretical description of this photoelectric effect caused by the photons' momenta [2].

The momentum transfer on the atom is caused by absorption and emission of photons. The employment of this effect paved the way towards various new techniques. After the cooling of neutral atoms with laser light was introduced by Ted Hänsch in 1975 [3], its application on a beam of sodium atoms was demonstrated by Bill Philips in 1982 [4]. After the first purely optical trapping in 1985, which was the first realization of what is now called an optical molasses [5], the first trapping of neutral sodium atoms in an optical-magnetic-hybrid trap was realized in 1987 [6]. These advances were also awarded with the Nobel Prize in 1997 [7, 8].

Nowadays, this so-called magneto-optical trap (MOT) is utilized in many laboratories all over the world. It has proven to be a very robust and viable technique for creating a cloud of cold atoms [9]. It can for example be used as a pre-cooling stage for the generation of Bose-Einstein condensates [10]. However, the experiment shown in this thesis is a rather uncommon application of a MOT.

Usually, a MOT is used to slow and trap a huge amount of atoms to further cool them or manipulate them in other ways. In the atom trap trace analysis (ATTA) experiment, the MOT rarely captures more than one atom at a time. In this experiment, the MOT is used to filter specific isotopes of a gas from an extremely large background of abundant ones. This is achieved by employing the isotope shift and the large amount of scattering events inside a magneto-optical trap. This ensures the perfect selectivity of this detection method [11].

The ATTA experiment has been successfully used to detect and measure the content of radioactive isotopes in argon and krypton [12, 13]. These desired isotopes are tracers, which are typically atoms or particles of interest for environmental applications. The amount of a certain tracer inside a sample is characteristic and is used for further studies. Therefore, this unique experiment creates an unusual connection between atomic and environmental physics. The collaboration with environmental physics opens the way to many possible applications of the ATTA experiment, whereas the atomic physics department can design and realize new atom optical

tools to enhance the flux into the MOT and therefore the detection performance of the apparatus.

This thesis aims to expand the applications of the Heidelberg ATTA collaboration towards the detection of new tracers and to enhance the throughput of samples for detection.

1 Introduction

The hydrosphere contains untapped information on environmental and anthropogenic processes, such as groundwater flow dynamics, ocean ventilation and climate change. These can be extracted by studying the concentration of specific tracers in the water. Samples taken from oceans, groundwater, ice and lakes can reveal the tracer composition and enable a deeper understanding of these processes. Measuring the concentration of the enclosed environmental tracers therefore unlocks profound knowledge on our environment [14].

Tracers can be atoms, molecules or even large particles which have a known input into the atmosphere. Diffusion of these into water, which is in contact with the surrounding air, causes a conditioning of the tracer's concentration. Extracting a sample later and measuring the tracer content reveals the moment of its last contact with the atmosphere. Defining this so-called age of the sample opens the door for environmental studies and models [14].

Tracer detection is already a standard procedure to gain insight on dynamics in a system. Various tracers are available and need to be adapted to each study, since they all have individual features [15]. The tracers can be of anthropogenic origin, purely environmentally produced, stable, or radioactive [16].

In this thesis the radioactive isotopes ^{39}Ar and ^{85}Kr of the noble gases argon and krypton are studied. Another radio-active tracer which will soon be included in this portfolio is ^{81}Kr. Whereas ^{39}Ar and ^{81}Kr are produced naturally in the atmosphere by cosmic rays, ^{85}Kr is mainly of anthropogenic origin [17]. This results in a constant ^{39}Ar and ^{81}Kr content in the atmosphere while ^{85}Kr, as a fission product from plutonium production, rises in concentration [18]. The input can be of civilian origin, from nuclear reprocessing plants, as well as caused by clandestine military plutonium production.

1.1 Radio-isotope dating

The usual procedure for radioactive tracer analysis is best understood when considering an example. The ocean's uppermost layer is steadily in contact with air, therefore atmospheric gas diffuses into the water, resulting in a tracer concentration conditioning. As this water parcel sinks below the surface, the radioactive atoms inside the solved gas begin to decay. Since their initial concentration c_0 relative to the abundant isotopes in the atmosphere is well known, a later extracted sample
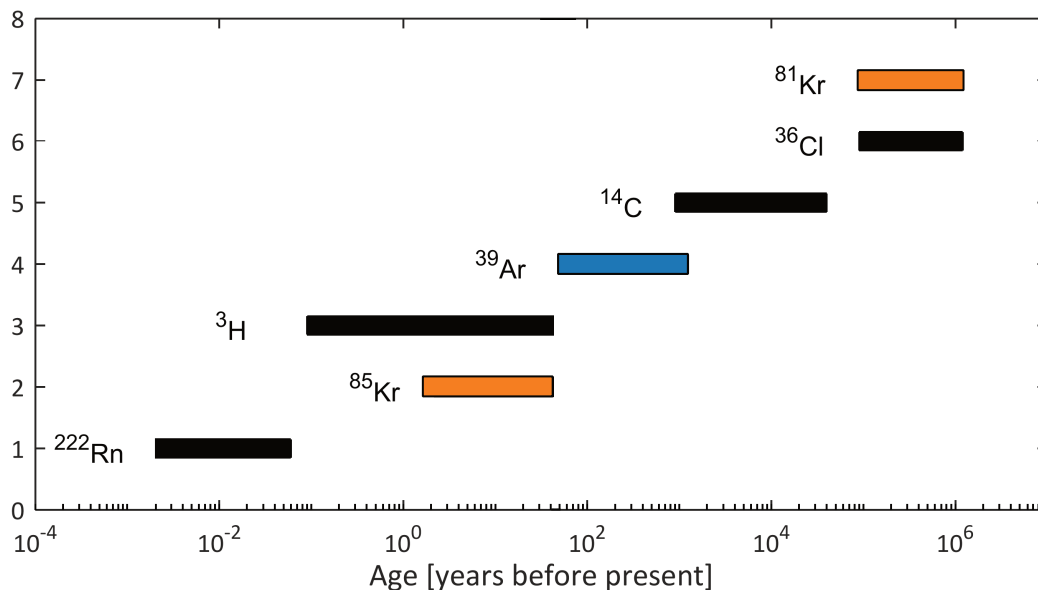
Figure 1.1: Dating ranges of radioisotopes used in hydrospheric studies. Each time window represents the dating range of the specific isotope and is defined by its unique half-life. The highlighted radioisotopes are also detected by the ATTA method. Figure taken from [19].

concentration c_s can be referenced onto this, yielding, together with the isotopes half-life $T_{1/2}$ and the resulting mean lifetime $\tau = T_{1/2}/ln(2)$, the time-span t during which the water body was cut off from air. The extraction of t is then given by the exponential decay law

$$c_s = c_0 e^{t/\tau}. \tag{1.1}$$

This time-span t is referred to as the 'age' of a sample, whereas the process of extracting the age information is called 'dating'[1] [14].

Roughly 0.1 to 10 times the half-life is the typical age application window for radioactive tracers. The most important ones can be seen in figure 1.1.

One subgroup of radioactive tracers are radioactive isotopes of noble gases. These are very favorable because, due to their chemical inertness, interaction with other particles in the water or sediment is negligible [21]. Unfortunately their relative abundance is extremely low. The krypton isotopes ^{81}Kr and ^{85}Kr are represented in the atmosphere with a concentration of 5×10^{-13} and 2×10^{-11}, respectively, compared to the most abundant isotope ^{84}Kr [14]. For ^{39}Ar the abundance relative to the most common argon isotope ^{40}Ar is even lower with 8×10^{-16} [19].

---

[1]Change in concentration of the desired tracer might also be caused by underground production in the sediment and could complicate the dating [20].

1.2 Detection of rare isotopes

This thesis specifies on the detection of long-lived radioactive isotopes of noble gases. In krypton these are ^{81}Kr and ^{85}Kr, in argon ^{39}Ar. While ^{81}Kr and ^{39}Ar are cosmogenic, the short-lived krypton isotope ^{85}Kr is fissiogenic and therefore mainly of anthropogenic origin [14].

1.2.1 Approaches

The arousing interest in these tracers caused different approaches towards their detection. Unfortunately the radioactive isotopes are very rare compared to the abundant ones of the same gas. Therefore the distinction of the desired atom is a huge challenge in dating. One liter of modern water typically contains $\sim$1000 ^{81}Kr, $\sim$6500 ^{39}Ar, and $\sim$41000 ^{85}Kr atoms, which is only a tiny fraction of the 10^{25} water molecules [22]. Current experiments implement a differentiation due to the atomic mass [23], the optical spectrum [12] or the radioactivity of the isotope [24].

Low Level Counting

Starting with the radioactivity of the isotope as the distinguishing feature, the technique of Low Level Counting (LLC) has been developed and is still used at the University of Bern. LLC counts the decays inside a sample of known volume and draws conclusions on its age from the measured activity and the known half-life of the tracer [24].

Measurements are conducted in a very peculiar underground laboratory 30 meters below ground. Also, its unique shielding is made from old shipwrecks' ^{210}Pb-depleted lead, all in order to decrease the radiation background [24].

Depending on the isotope a measurement can take about three weeks since many decay events are needed to obtain good statistics. This setup enables the measurement of ^{39}Ar and ^{85}Kr [25], while the activity of the extremely long-lived isotope ^{81}Kr ($T_{1/2} = 2.29 \times 10^5$ a) is too low to be investigated. Another drawback of this measurement scheme is the huge required sample size of up to 1000 L of water. One liter of young water produces only 17 ^{39}Ar decays per year [22].

Accelerator Mass Spectrometry

Another approach for separating noble gas isotopes is utilizing their mass difference by Accelerator Mass Spectrometry (AMS). The sample atoms are ionized and accelerated to very high energies on the order of hundred MeV to remove ambiguities in separation of ions with the same mass. They are then deflected by magnets and detected in a measurement region [23].

AMS has been successfully applied to ^{81}Kr [26] and ^{39}Ar [22] for groundwater studies. The background caused by the stable isotopes complicates the analysis

significantly and requires the acceleration of the atoms to high energies. Therefore big and costly facilities are needed, making AMS a rather challenging experiment [22].

Atom Trap Trace Analysis

Atom Trap Trace Analysis (ATTA) selects the isotopes by their unique optical properties. The specific atomic level structure is exploited by addressing transitions in the atoms with narrow-band laser light. An optical transition in the desired isotope is used to cool and capture it inside a magneto-optical trap (MOT). Since an atom needs to scatter many photons in order to be trapped, it is impossible to capture and detect another isotope featuring a different transition frequency. This high selectivity enables ATTA to extinguish the background of abundant isotopes [12].

The ATTA technique was first applied on the radio-isotopes in krypton in the Argonne National Lab (ANL) in Chicago [11]. In the Heidelberg ATTA lab a machine for detecting the argon isotope ^{39}Ar was set up and put to use for various tracer studies [13, 27, 28]. As of now, another ATTA experiment is running in Hamburg [29], some at the University of Science and Technology China [30] and one in Australia [31]. The interest in these dating machines is very high, since they promise an effective and feasible way towards noble gas tracer studies.[2]

1.3 Radio-argon dating

Argon is the third most abundant gas in the atmosphere, contributing 1% of total gas [33]. However, only one in 1.2×10^{15} atoms is the desired radioisotope for dating, ^{39}Ar [14]. The rare ^{39}Ar is generated in the atmosphere by cosmic ray induced spallation of ^{40}Ar or underground by rocks high in ^{39}K and radioactive sources like uranium or thorium [17]. Its concentration was measured to be stable within 7% over the last 1000 years [34].

The dating of a sample is achieved by measuring the ^{39}Ar concentration inside and comparing it to a known reference. Via the exponential decay the sample age can be directly derived from sample and reference measurement. With a half-life of $T_{1/2} = 269$ a and a resulting dating range of 50 to 1000 a the radioisotope is the ideal tracer to study the ventilation of oceans since the corresponding processes happen on a comparable time scale [14].

A study of this ventilation has already been achieved at the Heidelberg argon ATTA (ArTTA) apparatus [28]. Challenging about ^{39}Ar is the especially low relative abundance of the radioisotope and the lack of other stable isotopes with odd mass number. This results in a lack of abundant isotopes with a nuclear spin, which would

---

[2]ATTA can also be used for tracer studies of non-noble gases, like the rare ^{41}Ca [32].

enable easier referencing and machine stability monitoring.[3]

1.4 Radio-krypton dating

Compared to argon, krypton is a rather rare gas in the atmosphere. With only 1.099(9) ppm krypton gas [18], the corresponding amount of radioisotopes is even lower for krypton than for argon. However, gas extraction methods enable the separation of krypton from argon and can therefore annihilate this effect.

Krypton gas contains a variety of different isotopes, whereas the most abundant one, ^{84}Kr has a relative abundance of only 57 %. The stable isotope ^{83}Kr has a relative abundance of 11.5 % and is a powerful tool in performance testing for a krypton dating apparatus because of the presence of a nuclear spin.

^{85}Kr is a very versatile and apt tracer with a wide range of applications. For the water analysis, it is a perfect extension to the existing tracer ^{39}Ar, since it enables the detection of a possible contamination with atmospheric gas while sampling or extraction [18], but it is also a perfect extension for ocean water dating [17]. With the transit time distribution and dating ages for ^{39}Ar and ^{85}Kr the mixture of different water origins can be studied.

The radio-isotope ^{85}Kr can also be used for monitoring the Treaty on the Non-Proliferation of nuclear weapons, since it is a byproduct of nuclear reprocessing and plutonium production [36, 37]. It enables the discovery of clandestine production of weapon grade plutonium for example in North Korea [38, 39]. However, ^{85}Kr is also used in very different setups, for example in industry as a leak testing gas [40] or in manufacturing light bulbs [41].

^{81}Kr with its extremely long half-life of $T_{1/2} = 2.3 \times 10^5$ a is limited to applications in very old water bodies and ice cores. As the input of this isotope is only natural, anthropogenic sources are insignificant [18]. However, underground production of ^{81}Kr might complicate the dating [42]. It was successfully applied for dating of old groundwater in the Sahara desert [43] and ice cores in Antarctica [44].

---

[3]Machine monitoring and referencing is still done for argon, but with abundant isotopes which feature no nuclear spin and therefore no hyperfine splitting as opposed to ^{39}Ar [35].

2 Fundamentals

This chapter provides the theoretical background for the processes in the ATTA experiment. It is kept general in the beginning and will then focus on the desired noble gases argon and krypton. The atoms interaction with light and the influence of external magnetic fields on their internal energy structure will be discussed, leading towards the capture of atoms.

The second half introduces adjustments on the ArTTA machine used for the modification towards the krypton ATTA (KrypTTA) apparatus. The theoretical description of these tools is presented in this chapter to precede their following experimental study.

2.1 Interaction of atoms with light

Throughout the experiment, atoms are manipulated with laser beams of certain wavelength, polarization, and power. Each individual beam acts on the atoms differently and various effects can be observed. In this section, the behavior of atoms in radiative fields is mathematically described giving an introduction towards the experimental approach of laser cooling.

2.1.1 Density matrix model

The density matrix is a common approach in describing a system of atom and narrow-band laser light whilst including the effects of spontaneous emission. The results will be the optical Bloch equations and the scattering rate of the laser field's photons. More detailed description of the concepts is found in [45] and [46].

All information about a studied system in a pure state is stored in its normalized wavefunction $|\Psi\rangle$. In a Hilbert space of dimension n, the wavefunction $|\Psi\rangle$ can be, with the coefficients c_i, expanded in the basis $\{\Phi_n\}$ resulting in

$$\Psi = \sum_{i=1}^{n} c_i \Phi_i. \tag{2.1}$$

Alternatively, the system can be described with the density operator $\hat{\rho}$ which is defined as

$$\hat{\rho} = |\Psi\rangle \langle\Psi|. \tag{2.2}$$

With equation 2.1 one can write the elements of this $n \times n$ matrix as

$$\rho_{ij} = \langle \Phi_i | \, \hat{\rho} \, | \Phi_j \rangle = \langle \Phi_i | \Psi \rangle \langle \Psi | \Phi_j \rangle = c_i c_j^*. \tag{2.3}$$

However, with introduction of random spontaneous emission, the system is no longer in a pure state described by a single wavefunction $|\Psi\rangle$. The system transforms into a statistical mixture of several states $\{\Psi_n\}$ which can still be represented by the density operator

$$\hat{\rho} = \sum_i p_i \, |\Psi_i\rangle \langle \Psi_i| \, . \tag{2.4}$$

Now various $|\Psi_i\rangle$ can be occupied each with a probability p_i.

Considering a two-level atom with exited state $|e\rangle$ and ground state $|g\rangle$ the density matrix constructed with equation 2.3 will write as

$$\hat{\rho} = \begin{pmatrix} \rho_{ee} & \rho_{eg} \\ \rho_{ge} & \rho_{gg} \end{pmatrix} = \begin{pmatrix} c_e c_e^* & c_e c_g^* \\ c_g c_e^* & c_g c_g^* \end{pmatrix} \tag{2.5}$$

for a pure state $|\Psi\rangle = c_e \, |e\rangle + c_g \, |g\rangle$ [45].

The scattering rate γ_s for absorbing and emitting photons of the laser light frequency ω_l can be extracted from the time evolution of the density matrix elements. Typically, the laser light is detuned from the atomic resonance frequency ω_0 by the frequency $\delta = \omega_0 - \omega_l$. Spontaneous emission effects can be added separately as an exponential decay with a rate $\gamma/2$ [46]. The natural line-width γ is specific to each transition. Another specific number is the transition's Rabi frequency Ω of the transition which is defined as

$$\Omega \equiv -\frac{eE_0}{\hbar} \, \langle e | \, \hat{r} \, | g \rangle \tag{2.6}$$

with the laser light field amplitude E_0. It is used to describe the evolution of each ρ_{ij} by a differential equation similar to

$$\begin{aligned} \frac{\mathrm{d}\rho_{gg}}{\mathrm{d}t} &= \frac{\mathrm{d}c_g}{\mathrm{d}t} c_g^* + c_g \frac{\mathrm{d}c_g^*}{\mathrm{d}t} \\ &= i\frac{\Omega^*}{2} c_e e^{i\delta t} c_g^* - c_g i\frac{\Omega}{2} c_e^* e^{i\delta t} \equiv i\frac{\Omega^*}{2} \tilde{\rho}_{eg} - i\frac{\Omega}{2} \tilde{\rho}_{ge} \end{aligned} \tag{2.7}$$

with the substitute $\tilde{\rho}_{ge} \equiv \rho_{ge} e^{i\delta t}$. The description of the c_i in equation 2.7 is achieved by solving the two-level Rabi problem. Its solution is extensively discussed in [46].

Since the derivation is neglected in this thesis only the results are shown

$$i\hbar \frac{\mathrm{d}c_g(t)}{\mathrm{d}t} = \frac{\hbar\Omega^*}{2} c_e(t) e^{i\delta t}$$

$$i\hbar \frac{\mathrm{d}c_e(t)}{\mathrm{d}t} = \frac{\hbar\Omega}{2} c_g(t) e^{-i\delta t}. \tag{2.8}$$

Combining all this yields the optical Bloch equations (OBEs):

$$\frac{\mathrm{d}\rho_{gg}}{\mathrm{d}t} = \gamma\rho_{ee} + \frac{i}{2}(\Omega^*\tilde{\rho}_{eg} - \Omega\tilde{\rho}_{ge})$$

$$\frac{\mathrm{d}\rho_{ee}}{\mathrm{d}t} = -\gamma\rho_{ee} + \frac{i}{2}(\Omega\tilde{\rho}_{ge} - \Omega^*\tilde{\rho}_{eg})$$

$$\frac{\mathrm{d}\tilde{\rho}_{ge}}{\mathrm{d}t} = -\left(\frac{\gamma}{2} + i\delta\right)\tilde{\rho}_{ge} + \frac{i}{2}\Omega^*(\rho_{ee} - \rho_{gg})$$

$$\frac{\mathrm{d}\tilde{\rho}_{eg}}{\mathrm{d}t} = -\left(\frac{\gamma}{2} - i\delta\right)\tilde{\rho}_{eg} + \frac{i}{2}\Omega(\rho_{gg} - \rho_{ee}). \tag{2.9}$$

Here also the spontaneous emission is included as

$$\left(\frac{\mathrm{d}\rho_{eg}}{\mathrm{d}t}\right)_{spont.} = -\frac{\gamma}{2}\rho_{eg}. \tag{2.10}$$

These equations are now solved for a steady-state. In this case, the population difference u between the excited state and ground state is constant in this case, resulting in $u \equiv \rho_{gg} - \rho_{ee} = $ constant. From the OBEs one obtains

$$\frac{\mathrm{d}u}{\mathrm{d}t} = \frac{\mathrm{d}(\rho_{gg} - \rho_{ee})}{\mathrm{d}t} = -\gamma w - i\left(\Omega^*\tilde{\rho}_{eg}^* - \Omega\tilde{\rho}_{ge}\right) + \gamma. \tag{2.11}$$

For the steady-state the off-diagonal elements vanish, $\mathrm{d}\rho_{eg}/\mathrm{d}t = 0$ and the constant population difference results in $\mathrm{d}u/\mathrm{d}t = 0$. This allows one to solve the equations for

$$u = \frac{1}{1+s} \tag{2.12}$$

$$s \equiv \frac{|\Omega|^2}{2(\delta^2 + \gamma^2/4)} \equiv \frac{s_0}{1 + (2\delta/\gamma)^2} \tag{2.13}$$

$$s_0 \equiv \frac{2|\Omega|^2}{\gamma^2} \equiv \frac{I}{I_s}. \tag{2.14}$$

The total scattering rate γ_s of photons from the light source is given by the sponta-

neous decay rate γ and the population of the excited state ρ_{ee} as

$$\gamma_s = \gamma\rho_{ee} = \gamma\frac{(1-w)}{2} \tag{2.15}$$

since a higher population in the excited state leads to a higher total scattering rate. Here also the population conservation $\rho_{ee} + \rho_{gg} = 1$ was used.

Finally, with equations 2.12 and 2.15 one can find an expression for the total scattering rate, including the excited state decay rate γ, laser detuning δ and saturation parameter s_0

$$\gamma_s = \frac{\gamma}{2}\frac{s_0}{1 + s_0 + (2\delta/\gamma)^2}. \tag{2.16}$$

As laser intensity and therefore s_0 increases, γ_s saturates to $\gamma_s = \gamma/2$ which is the maximum achievable scattering rate. This result gives a measure for the interaction between atom and light field, scaled by the tunable laser parameters δ and s_0. How this rate affects the control on an atom is discussed in the following.

2.1.2 Light induced forces

Deriving the scattering rate was the first step towards determination of laser-induced forces acting on the atoms. The amount of emission and absorption cycles results together with the scattered photon's momentum in a net force on the atom.

Each photon carries a momentum given by $\vec{p} = \hbar\vec{k}$ which is transferred on the atom in the absorption or emission process [46]. The atom is converted to the excited state in which it stays until it de-excites by emission of another photon. In the case of spontaneous emission the radiation is distributed randomly over all spatial directions, therefore the averaged recoil due to emission becomes zero for many cycles. However, as the momentum transfer from the absorbed photons is defined by the propagation direction $\vec{k}$ of the laser light a net force $\vec{F}$ can be observed:

$$\vec{F} = \hbar\vec{k}\gamma_s. \tag{2.17}$$

The magnitude of this force is given by the amount of absorption-emission cycles per time defined by the previously introduced total scattering rate γ_s. Together with equation 2.16 one finds

$$\vec{F} = \hbar\vec{k}\gamma\frac{s_0/2}{1 + s_0 + (2\delta/\gamma)^2}. \tag{2.18}$$

This force can be increased by laser intensity but saturates for very high powers to $\vec{F}_{max} = \hbar\vec{k}\gamma/2$. Note that the detuning δ between the laser frequency the atom's internal resonance frequency can experience various shifts caused for example by the Doppler effect or magnetic fields. Both will be introduced in the following.

Doppler Shift

The Doppler effect causes a frequency shift δ_D depending on the relative velocity between laser and atom. In the atom's rest frame the laser frequency appears to be shifted by

$$\delta_D = -\vec{k} \cdot \vec{v} \tag{2.19}$$

with the atom's velocity $\vec{v}$ and the wavevector $\vec{k}$ [47].

Since δ_D is given by the scalar product of the vectors $\vec{k}$ and $\vec{v}$ the shift becomes zero for an orthogonal relation between the two and maximal for a parallel relation.

The atom's velocity changes with increasing amount of scattered photons. Depending of the beam's angle of incidence, this results in a shift of laser detuning based on equation 2.19.

If the atom's velocity is changed by a larger amount, this detuning shift needs to be compensated by tuning of the laser frequency or the atoms internal energy structure. A great example for the latter is the magnetic shift inside a Zeeman slower, which will be introduced in the next section.

2.2 Interaction of atoms with magnetic fields

The manipulation of an atom's internal structure is a major step towards its control with narrow-band laser light. Position dependent changes in the level structure can introduce spatial confinement of atoms, as will be shown in the next section. This section introduces the tools for atom control with magnetic fields and provides the necessary background. Further information can be found in [48].

2.2.1 Zeeman Shift

When introducing an atom into an external magnetic field $\vec{B}_0$ it experiences a potential energy depending on the atom's magnetic moment $\vec{\mu}$. The strength of this Zeeman effect is described with the potential energy gain

$$\Delta E_{pot} = -\vec{\mu} \cdot \vec{B}_0. \tag{2.20}$$

The total angular momentum of the atom, whether it might be $\vec{L}$, $\vec{J}$, $\vec{S}$, or $\vec{F}$ makes up the magnetic moment via $\vec{\mu}_F = -\mu_B g_F \vec{F}/\hbar$ with the Landé-factor g_F and the Bohr magneton μ_B. Here, the magnetic moment of the hyperfine structure $\vec{\mu}_F$ is chosen as substitute for any magnetic moment $\vec{\mu}_{L,J,S,F}$.

For an external magnetic field in z-direction $\vec{B}_0 = \vec{e}_z B_z$ the vector $\vec{\mu}_F$ can only have discrete projections on the z-axis which are denoted by the quantum number

m_F. Therefore the z-component of the magnetic moment simplifies to

$$(\vec{\mu}_F)_z = -\left(\mu_B g_F \vec{F}/\hbar\right)_z = -\mu_B g_F m_F \tag{2.21}$$

and the energy gain can be written as

$$\Delta E(F, m_F) = \mu_B g_F m_F B_z \tag{2.22}$$

whereas [49] provides a more detailed derivation.

Since often only energy differences are considered one can use equation 2.22 to calculate the detuning δ_Z of a transition from $|g\rangle$ to $|e\rangle$ due to Zeeman splitting as

$$\delta_Z = \frac{1}{\hbar}[\Delta E(F_e, m_{F_e}) - \Delta E(F_g, m_{F_g})] = \mu_B(g_e m_e - g_g m_g)\frac{B}{\hbar} \equiv \frac{\mu'}{\hbar}B. \tag{2.23}$$

The newly introduced μ' is the effective magnetic moment of the transition. Equation 2.23 now provides the calculation of a magnetic field dependent detuning of a transition.

2.3 Cooling and trapping of atoms

The in equation 2.18 displayed force is commonly used for atom cooling. Additionally, the manipulation of the atom's internal structure with magnetic fields, as shown in equation 2.23, can be employed for position dependent cooling. This section provides the theoretical introduction towards cooling and trapping schemes used in the ATTA apparatus.

2.3.1 Optical molasses

Previously, the force of a single laser beam on an atom was derived from its scattering rate. Now this concept is extended to multiple beams. Considering a case of small laser power, an atom might be excited to a higher level by a laser beam but stimulated emission does not take place. This allows to calculate the total force acting on an atom by addition of the forces introduced by each laser beam.

In one dimension the total force on an atom of velocity $\vec{v}$ due to illumination by two counter-propagating laser beams with wavevectors $\vec{k}$ and $-\vec{k}$ can therefore be derived from equation 2.18 and 2.19 to be

$$\begin{aligned} \vec{F} &= \vec{F_+} + \vec{F_-} \\ &= \frac{\gamma\hbar\vec{k}s_0}{2}\left[\frac{1}{1 + s_0 + (2(\delta - \vec{k}\cdot\vec{v})/\gamma)^2} - \frac{1}{1 + s_0 + (2(\delta + \vec{k}\cdot\vec{v})/\gamma)^2}\right] \end{aligned} \tag{2.24}$$
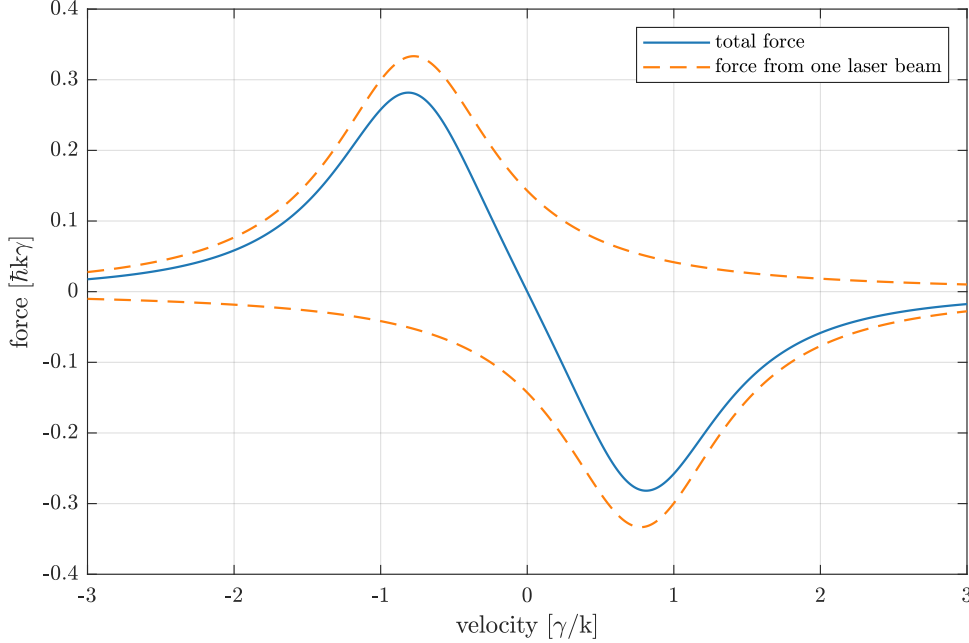
Figure 2.1: Forces on an atom in a one-dimensional optical molasses versus the atom's velocity. The detuning of the laser beams was set to $\delta = -\gamma$ and the saturation parameter $s_0 = 2$. The dashed, orange lines display the force from the two counter-propagating lasers individually. The solid line shows the total force from both laser beams, which is the sum of both dashed lines. The linear slope β of the force around $v = 0$ is well visible.

if only the Doppler shift δ_D needs to be considered and no magnetic field is present. The resulting force can for small velocities and detunings be approximated by

$$\vec{F} \approx \frac{8\hbar k^2 \delta s_0 \vec{v}}{\gamma(1 + s_0 + (2\delta/\gamma)^2)^2} \equiv -\beta\vec{v}. \tag{2.25}$$

A damping force and therefore cooling in one dimension can be realized by choosing a negative detuning $\delta < 0$ of the laser light [46]. A positive detuning would have not a cooling but a repulsive effect and is therefore not of use for the experiments discussed here. The damping force in the dimension of $\vec{k}$ is caused by a stronger interaction of atoms of non zero velocity with the laser beam which propagation direction opposes their propagation direction. This is caused by the Doppler shift which was introduced previously in equation 2.19.

This setup is called an optical molasses (OM) and the used principle Doppler

cooling. A plot of the calculated force over velocity in one dimension can be seen in figure 2.1. The figure shows the force each of the two laser beams exerts on the atom as a dashed line, the resulting total force is represented by the solid line. One can observe an approximately linear force for small velocities $|\vec{v}| < \gamma/k$ which corresponds to the slope β derived in equation 2.25.

The optical molasses extended to three dimensions enables cooling of atoms but no confinement to the center, therefore the atoms are not trapped [46].

2.3.2 Magneto-optical trap

A magneto-optical trap (MOT) uses the cooling force of an optical molasses and superposes it with a position dependent energy shift caused by an inhomogeneous external magnetic field. It harnesses the previously introduced Doppler and Zeeman frequency shifts resulting in a velocity and position selective force which enables trapping. The versatility and robustness of this concept was already praised in the preface [6].

In the following the underlying principle of the MOT will be introduced resulting in the description of forces inside it. More information on these traps and their setup can be found in [7, 8], the derivation of the experienced forces is extensively discussed in [46].

The position dependent Zeeman shift of an atom's sublevels is generated with a linearly inhomogeneous magnetic field with a constant field gradient. The higher the field, the larger the splitting between the sublevels, as can be understood with equation 2.23. Furthermore, the magnetic field is constructed to feature a zero-crossing which defines the center of the trap. All sublevels of the observed atom are degenerate at the center and separate as the atom travels away from it.

For simplicity it is helpful to reduce the trap to one dimension. The forces needed for cooling and trapping are introduced by two red-detuned ($\delta < 0$) counter-propagating lasers. These transfer the atoms to the excited state $|e\rangle$ as already shown for the optical molasses. However, now the polarization of the beams is also of interest, since the magnetic substates are split, and the polarization of a photon defines the transition which can be excited. The connection between level splitting and photon polarization is described by radiative selection rules [47].

A light wave's polarization is defined by the orientation of its electric field vector. In the case of a spatially rotating field the polarization is circular with a handedness depending on the rotation direction defined along the wave vector $\vec{k}$.

For the atom not the polarization itself but rather the helicity of the photon is crucial which can be either σ^+ or σ^-. The helicity σ^+ is defined to excite the transition $|F_g, m_{F,g}\rangle \rightarrow |F_e, m_{F,g} + 1\rangle$ with a change in angular projection $\Delta m_F = +1$. Analogously σ^- light drives a $\Delta m_F = -1$ transition in the atom. In a MOT the helicity is fixed to be σ^+ for one and σ^- for the opposing beam. Following the radiative selection rules with laser beam helicity and internal atom structure
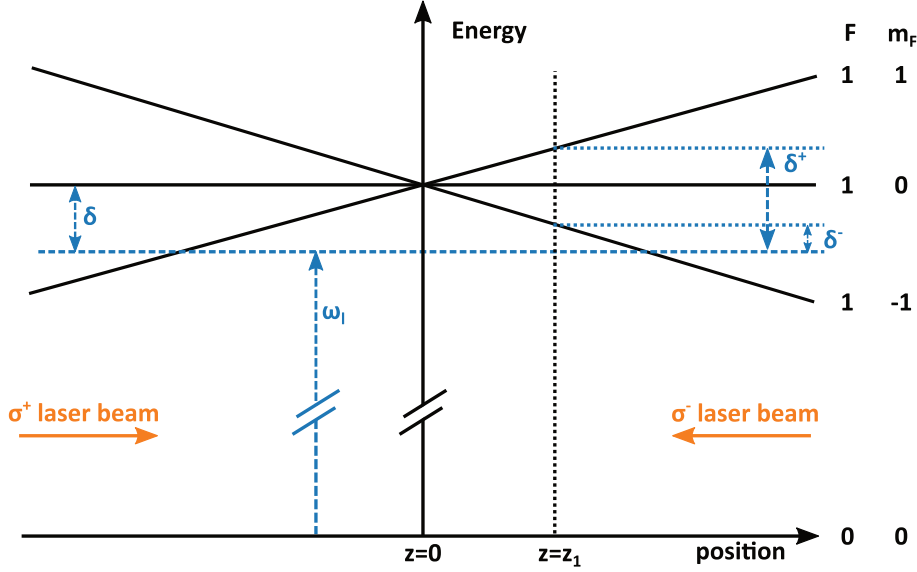
Figure 2.2: Schematic of the magneto-optical trap concept restricted to one dimension. The transition from the ground state $|g\rangle = |J = 0, m_J = 0\rangle$ to the excited state $|e\rangle = |J = 1, m_J = -1, 0, +1\rangle$ is driven by laser light detuned to the atomic resonance by δ. A linearly inhomogeneous magnetic field causes the splitting of the three excited states. The center of the trap is defined as the point of zero magnetic field which causes the upper levels to be degenerate. Moving in positive (negative) z direction of the center causes the magnetic field to increase which shifts the level $|J = 1, m_J = -1\rangle$ of an atom at this position downwards (upwards) in energy. At $z = z_1 > 0$ the state $|e\rangle = |J = 1, m_J = -1\rangle$ is then closer to resonance with the laser and more likely to scatter photons. Since the transition requires the scattering of a σ^- photon, the atom selectively scatters the light of the counter-propagating laser beam, resulting in a force towards the trap center. The figure is adapted from [46].

results in the desired trapping of atoms. In the following this will be discussed more extensively with one specific atom in one dimension.

As an example the transition $|g\rangle \rightarrow |e\rangle$ with $F_g = 0$ and $F_e = 1$ is studied. The excited level will under presence of the magnetic field split up into its angular substates defined by the projections $m_{F,e} = 0$, $m_{F,e} = 1$, and $m_{F,e} = -1$, whereas the ground state with $m_{F,g} = 0$ remains unchanged. This energy splitting is illustrated in figure 2.2.

As the atom travels outwards on the $B > 0$ side of the trap center, the $|F_e = 1, m_{F,e} = +1\rangle$ state is shifted upwards in energy, whereas $|F_e = 1, m_{F,e} = -1\rangle$ is shifted downwards. This decrease in energy causes this state to be closer to resonance with the red-detuned laser light. Since the transition from $|g\rangle = |0, 0\rangle$ to

the resonant state $|e\rangle = |1, -1\rangle$ needs to be driven with σ^- light, one chooses the σ^- laser beam to counter-propagate the atoms motion away from the center. When scattering this beam, the atom then experiences a force towards the center of the trap. Analogously atoms moving in the $B < 0$ direction are pushed back to the trap center by the opposing laser beam of σ^+ helicity.

Figure 2.2 shows a schematic of this principle in one dimension. At the position $z = z_1$, the transition from the ground state $|0, 0\rangle$ to the excited state $|1, -1\rangle$ is detuned by δ^- which is smaller than the detuning δ^+ of the transition to the excited state $|1, 1\rangle$. Due to this, the atom is more likely to scatter the σ^- light that pushes the atom towards the center at $z = 0$.

The concept of the one-dimensional MOT is readily expanded to 3D with three pairs of orthogonal, counter propagating laser beams and a quadrupole magnetic field which can be achieved with a pair of anti-Helmholtz coils.

However, in most cases the transition is not between a state of angular momentum $F_g = 0$ and $F_e = 1$. Fortunately, the trapping works for any transitions where $F_e = F_g + 1$ since the transitions between the splitted angular sub-states are then closed.[1]

Looking at the force experienced by the atom inside the trap, one can go back to equation 2.24 to find

$$\vec{F} = \vec{F_+} + \vec{F_-}, \tag{2.26}$$

$$\vec{F_\pm} = \hbar \vec{k} \gamma \frac{s_0/2}{1 + s_0 + (\frac{2\delta_\pm}{\gamma})^2}. \tag{2.27}$$

The total detuning $\delta_\pm$ is now given by the Doppler and Zeeman shift defined as δ_D and δ_Z, respectively:

$$\delta_\pm = \delta + \delta_{D\pm} + \delta_{Z\pm} = \delta \mp \vec{k} \cdot \vec{v} \pm \frac{\mu'}{\hbar} B. \tag{2.28}$$

The detuning δ is the difference between the atom's resonance at rest, without magnetic field and the photons frequency. For $\delta < 0$ the atoms experience a deceleration and can effectively be cooled and trapped.

The MOT enables trapping and detection of single atoms in the ATTA experiment and is therefore the core of the dating apparatus. Studying the forces inside it further helps to identify the optimal parameters for a combination of high capture efficiency and feasible single atom detection. These parameters were studied at the Heidelberg ArTTA facility theoretically and experimentally for ^{39}Ar in [50, 51] and [19]. This studied noble gas isotope is in many ways comparable to ^{85}Kr which causes the optimal parameter set to not differ strongly. How comparable krypton and argon really are is discussed in the next section.

---

[1] It works for any transition where the angular momentum quantum number increases by one.

2.4 Isotopes and level schemes

This section discusses the atomic spectra of the trapped noble gas isotopes. Studying these introduces the used state transitions and their frequency. A general picture for both argon and krypton will be given and then expanded to provide the atom specific background.

2.4.1 Atomic level structure

Since they are both noble gases, argon and krypton are very similar in their atomic level structure. In the ground state both feature completely occupied electronic shells which causes the electron configuration of argon to be

$$\text{Ar}: 1\text{s}^2 2\text{s}^2 2\text{p}^6 3\text{s}^2 3\text{p}^6 = [\text{Ne}]3\text{s}^2 3\text{p}^6 \tag{2.29}$$

and for krypton to be

$$\text{Kr}: [\text{Ar}]3\text{d}^{10}4\text{s}^2 4\text{p}^6. \tag{2.30}$$

Each tuple nl^e denotes an electronic state [52]. It is defined by the principal quantum number n and the orbital angular moment l which can reach values of $l = 0, 1, ..., n-1$. The superscript digit is the number of electrons in this specific level.

For the first excited state an electron of the highest state is transferred to 4s or 5s for argon and krypton, respectively. Because this electron needs to be taken out of a filled shell to be excited, the required transfer energy is very high ($\sim 10\,\text{eV}$). Laser cooling and trapping needs a transition in a more comfortable frequency range which can be easily driven with commercial laser sources. Therefore, the transition for laser cooling does not start from the absolute ground state but a meta-stable excited state from which transitions can be driven with smaller energies.

These electron configurations of these states are for argon

$$[\text{Ne}]3\text{s}^2 3\text{p}^5 4\text{s}^1 \rightarrow [\text{Ne}]3\text{s}^2 3\text{p}^5 4\text{p}^1 \tag{2.31}$$

and for krypton

$$[\text{Ar}]3\text{d}^{10}4\text{s}^2 4\text{p}^5 5\text{s}^1 \rightarrow [\text{Ar}]3\text{s}^{10}4\text{s}^2 4\text{p}^5 5\text{p}^1 \tag{2.32}$$

where the first state is the meta-stable state. Knowing the electron configuration is a first step towards the energy level structure of the transition, but the coupling of the electrons with each other needs to be considered as well. Since the outer electron occupies a state of higher n than the others and the orbital radius scales with n^2 the electron in the excited state is rather far away from inner ones.

This causes the remaining non-excited electrons that make up the so-called 'body' to couple with each other, resulting in LS-coupling of the total body spin $\vec{S} = \sum_i \vec{s}_i$ and total body orbit angular momentum $\vec{L} = \sum_i \vec{l}_i$ to the total body angular

momentum $\vec{j}_{\text{body}} = \vec{S} + \vec{L}$. The excited electron first couples with its orbital angular momentum $\vec{l}$ to $\vec{j}_{\text{body}}$ resulting in $\vec{K}$ with $K = |j_{\text{body}} - l|, |j_{\text{body}} - l| + 1, ..., |j_{\text{body}} + l|$.

Finally, the outer electron spin $\vec{s}$ couples with $\vec{K}$ to achieve the total angular momentum of all electrons $J = |K - s|, |K - s| + 1, ..., |K + s|$. The coupled quantum numbers of the body electrons do not change between the meta-stable and excited state, therefore they apply to both atoms and states $S = 1/2$ and $L = 1$. Also the total angular momentum of the body is the same for these two states with $j_{\text{body}} = 3/2$ [52, 53]. Another possibility would be $j_{\text{body}} = 1/2$.

For the excited state electron the quantum numbers are $l_e = 1$ and $s_e = 1/2$, the meta-stable ground state features $l_g = 0$ and $s_g = 1/2$. This enables various coupling possibilities for K ($K_g = 1/2, 3/2$, $K_e = 1/2, 3/2, 5/2$). The states investigated in this thesis feature $K_g = 3/2$ for the ground state and $K_e = 5/2$ in the excited state, resulting in $J_e = 3$ and $J_g = 2$.[2] With the Racah-notation

$$nl[K]_J \tag{2.33}$$

one then obtains an expression for the cooling transition in argon as

$$4\text{s}\,[3/2]_2 \rightarrow 4\text{p}\,[5/2]_3 \tag{2.34}$$

and in krypton with

$$5\text{s}\,[3/2]_2 \rightarrow 5\text{p}\,[5/2]_3\,. \tag{2.35}$$

Introducing the nuclear spin I results in discarding of J as the total angular momentum. It is replaced by the quantum number F for the hyperfine structure which is given by $F = |I - J|, |I - J| + 1, ..., |I + J|$.

There are also transitions other than the cooling transition used for ATTA. One is the quench transition which excites atoms from the meta-stable level to an excited state from which they can either decay back into the meta-stable state or to another state which can in turn decay to the absolute ground state. This open transition from the meta-stable state can selectively de-excite atoms from the cooling ground state and therefore reduce off-resonantly scattered stray light of abundant isotopes in the detection chamber.

2.4.2 Argon

Atmospheric argon contains many different isotopes, which are listed in table 2.1 with their for ATTA most relevant features.

Based on the discussion in the previous section figure 2.3 shows an excerpt of the energy spectrum for argon isotopes of even mass number, which feature no nuclear

---

[2]Also here other J are possible but only the states necessary for cooling are treated in this section. A more thorough view on the coupling can be found in [54]
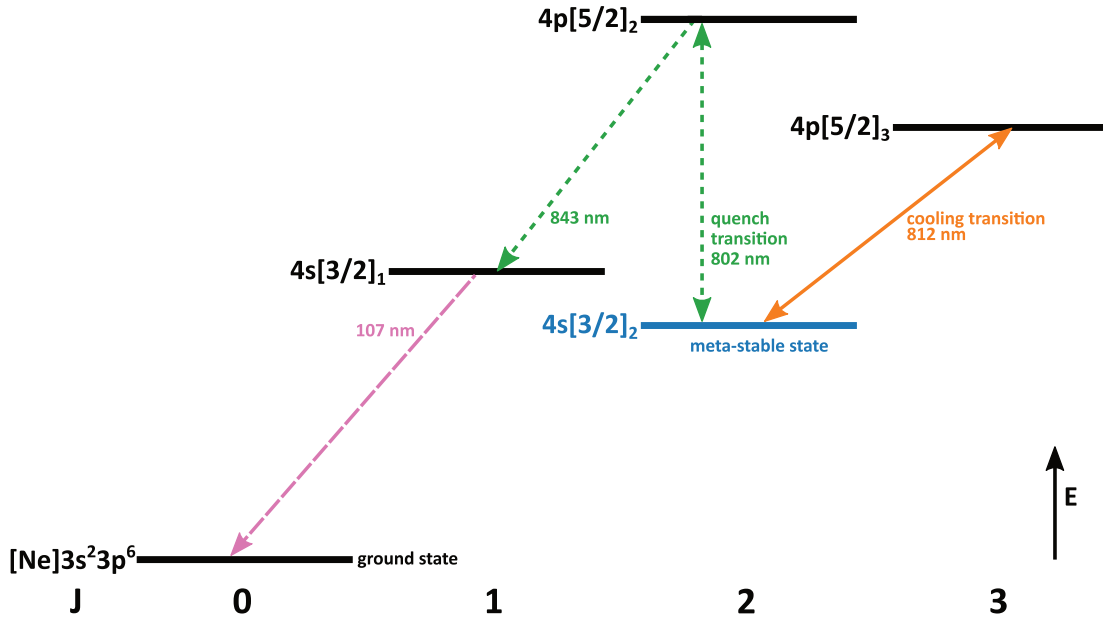
Figure 2.3: Part of the energy spectrum of argon relevant to ATTA using the $nl[K]_J$ notation. The transition from the absolute ground state $[\text{Ne}]3\text{s}^2 3\text{p}^6$ to the first excited state requires a wavelength of 107 nm and is therefore not feasible for laser cooling. Instead the meta-stable state $4\text{s}[3/2]_2$, marked here in blue, is populated with an rf-generated plasma. The cooling transition is then driven from this meta-stable state to the excited state $4\text{p}[5/2]_3$ creating a closed transition shown with a solid, orange line. The green dashed line represents another transition from the meta-stable state which is called the quench transition. It excites the atoms with 802 nm light from $4\text{s}[3/2]_2$ to $4\text{p}[5/2]_2$. From this excited state the atoms can fall back to the ground state via $4\text{s}[3/2]_1$ by emission of a 843 nm and a 107 nm photon.

spin I. To some extend the scheme also applies to ^{39}Ar with a nuclear spin of $I = 7/2$ except that the states are additionally split up due to the hyperfine structure. A more extensive transition scheme can be found in the appendix A.2.

Doppler cooling demands a closed cycling transition, since it requires a huge amount of absorption-emission cycles in order to maximize the scattering rate and thereby the force in equation 2.24. Figure 2.3 shows an energy difference between absolute ground state and first excited state which is equivalent to a wavelength of 107 nm. Currently, there is no laser or optics available for such wavelengths so an rf induced plasma discharge transfers a fraction of the atoms to the highlighted

isotope	cooler frequency shift relative to ^{40}Ar [MHz]	relative abundance [%]	I	$T_{1/2}$
^{36}Ar	450.1	0.3365(30)	0	stable
^{37}Ar	-	no natural ab.	3/2	35 d
^{38}Ar	208.1	0.0632(5)	0	stable
^{39}Ar	-492.2	$8.23 \cdot 10^{-16}$	7/2	269 a
^{40}Ar	0	99.6003(30)	0	stable

Table 2.1: List of relevant argon isotopes and their most significant features. The low relative abundance of the radioisotope ^{39}Ar is striking [19].

repumper	1st	2nd	3rd	4th
transition $F_g \rightarrow F_e$	$9/2 \rightarrow 11/2$	$7/2 \rightarrow 9/2$	$5/2 \rightarrow 9/2$	$3/2 \rightarrow 7/2$
shift relative to cooler [MHz]	-680	-1242	-1664	-1933

Table 2.2: Frequency shift of ^{39}Ar repumpers relative to the cooling transition.

meta-stable state 4s[3/2]$_2$, from which atoms can be excited by laser light of 812 nm to the state 4p[5/2]$_3$ [55].

With a lifetime of 60 s the 4s[3/2]$_2$ state[3] is suitable as the ground state of the cooling cycle. Due to the selection rule $\Delta J = 0, \pm 1$ the excited $J = 3$ state can only decay back to $J = 2$, closing the transition.

Another employed excitation from the meta-stable state is the so-called quench transition which quenches atoms out of the cooling cycle. This is achieved by driving the 4s[3/2]$_2 \rightarrow$ 4p[5/2]$_2$ transition. From the higher state the atoms can, through emission of a 843 nm photon, decay to the 4s[3/2]$_1$ state from which they can decay back to the absolute ground state with a dipole transition. Therefore the atoms will after scattering a couple of quench photons eventually be lost from the cooling cycle. This is typically used to selectively de-excite the abundant ^{40}Ar to reduce background during ^{39}Ar detection caused by off-resonant photon scattering.

The level scheme gets more complicated for ^{39}Ar due to its nuclear spin of $I = 7/2$. The quantum number J no longer fully describes the system, and the new quantum number $F = |I - J|, |I - J| + 1, ..., |I + J|$ is introduced. This splits the spectrum in substates corresponding to F, shown for the cooling transition in argon on the right side of figure 2.4.

The cooling ground state splits up into five substates with $F_g = 11/2, 9/2, ..., 3/2$,

---

[3]In other publications, often the Paschen Notation is used. In this notation the ground state is denoted by 1s$_5$($J = 2$) and the excited state by 2p$_9$($J = 3$). This notation is mostly equivalent to the here presented one.
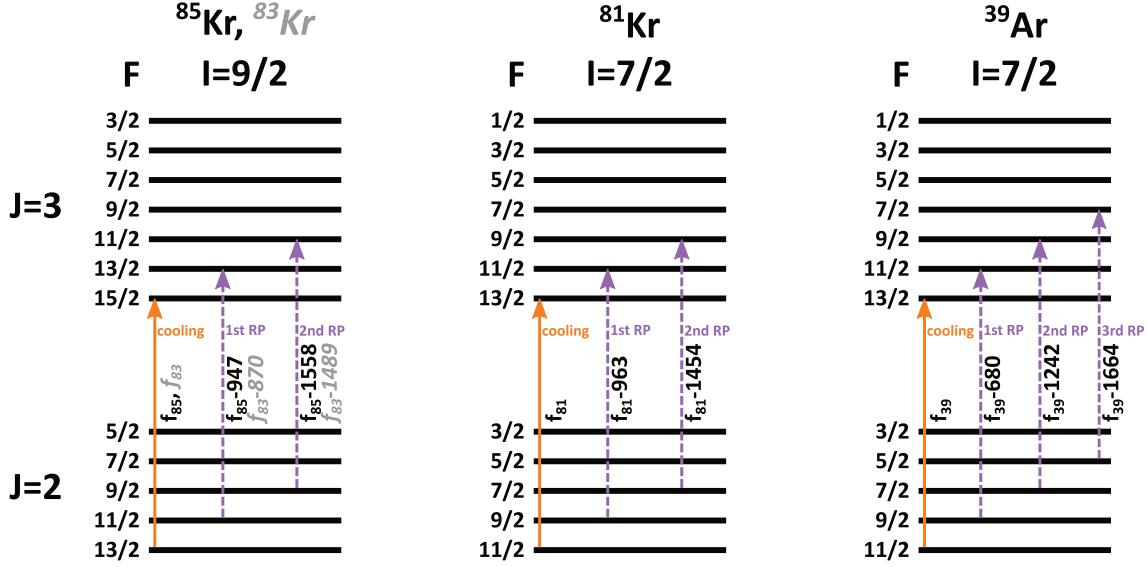
Figure 2.4: Ground and excited state hyperfine structure of krypton and argon iso-topes for ATTA. The employed electronic transitions are indicated with arrows. Solid lines represent the cooling transition which is a closed one. Dashed lines show the transitions driven by the additional repumper side-bands. The frequencies of the repumpers are given in relation to the cooling frequency. For the krypton isotopes only two repumpers were realized in this theses for argon three were used. The repumpers bring atoms back to the cooling cycle which might have been off-resonantly excited to another hyperfine state or in the beginning to populate the lowest hyperfine state [53, 51].

the excited state into seven states $F_e = 13/2, 11/2, ..., 1/2$. The

$$4s[3/2]_2(F = 11/2) \rightarrow 4p[5/2]_3(F = 13/2) \tag{2.36}$$

transition is chosen for cooling since the excited state can only decay back to the ground state due to the selection rule $\Delta F = 0, \pm 1$. However, the other levels are so close that a saturation broadened laser beam can excite other transitions as well. Because of this effect and in order to increase the ratio of atoms in the $F = 11/2$ state after the rf-discharge, new laser frequencies are introduced, the so-called repumpers [55]. With these additional laser frequencies the atoms can be transferred back to the $4s[3/2]_2(F = 11/2)$ state. Table 2.2 shows the frequencies of these repumping transitions relative to the cooling transition in ^{39}Ar.

The spontaneous decay rate of the chosen cooling transition is [46]

$$\gamma = 2\pi \times 5.87 \, \text{MHz}. \tag{2.37}$$

Other argon specific values are displayed in table 2.5 and 2.6. They will be useful when it comes to calculating the force acting on the atoms at various stages of the ArTTA experiment.

2.4.3 Krypton

The additional detection of ^{85}Kr enables the Heidelberg ATTA collaboration to check for contamination of samples in the ^{39}Ar dating range which should be ^{85}Kr depleted. For water bodies that feature a stronger mixing with water of younger ages, the examination of both tracers in the same sample results in a transit time distribution [28].

Atmospheric krypton contains many different isotopes, some of which are produced naturally in the atmosphere by cosmic rays and some of anthropogenic, fissiogenic origin [14]. Table 2.3 gives an overview of the for ATTA most relevant isotopes.

isotope	relative abundance	nuclear spin	$T_{1/2}$ [a]
^{81}Kr	$5 \cdot 10^{-13}$	7/2	2.29×10^5
^{83}Kr	0.12	9/2	stable
^{84}Kr	0.57	0	stable
^{85}Kr	$2 \cdot 10^{-11}$	9/2	10.8

Table 2.3: List of krypton isotopes important for ATTA and their most relevant features [57, 14].

The table also shows a helpful characteristic of krypton, which it unfortunately does not share with argon. The isotope ^{83}Kr is a stable and abundant isotope, which features a nuclear spin and therefore requires repumpers for cooling and capturing. Stable and abundant isotopes of argon have no nuclear spin, hindering the testing of the complete laser setup with stable isotopes before the ArTTA measurement.

Figure 2.5 shows the relevant part of energy levels in krypton for isotopes without a nuclear spin I. Other isotopes experience an additional splitting of the displayed levels based on the new quantum number F. Similarly as for argon, the transition from the atom's absolute ground state is in the deep UV regime. With 124 nm the energy is lower than for argon and optical production of a meta-stable krypton beam has already been shown in [58] by driving the 124 nm transition with an UV lamp, followed by a 819 nm laser excitation to a higher lying state. From there the krypton decayed to the desired meta-stable state with a probability of 77 %. In
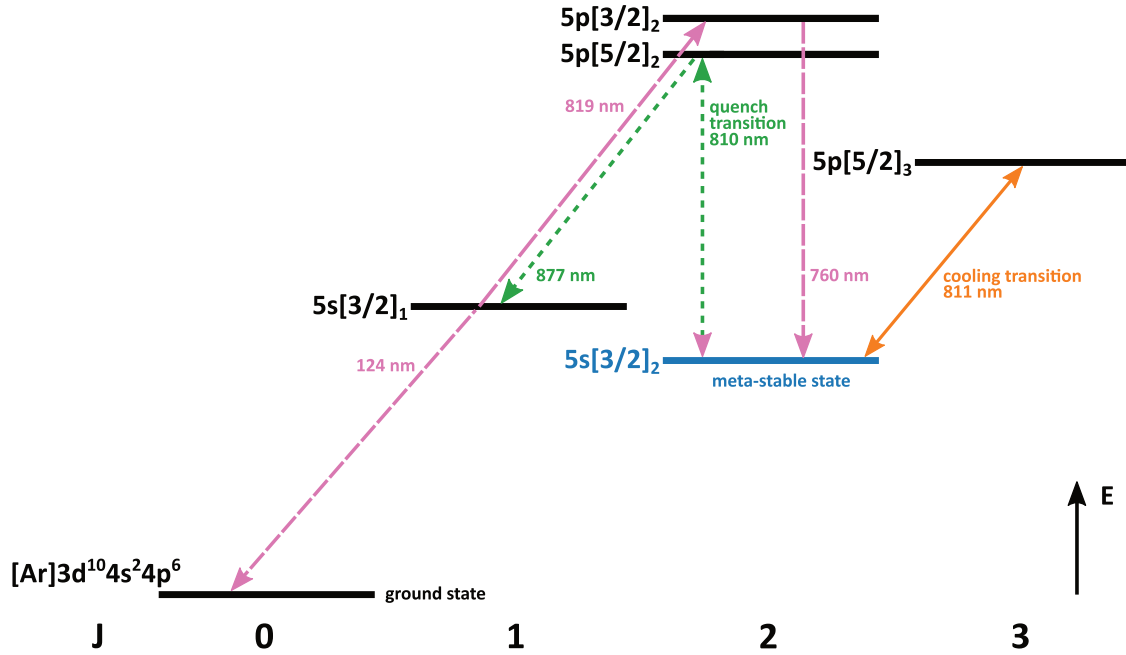
Figure 2.5: Part of the energy spectrum of krypton relevant to ATTA with the $nl[K]_J$ notation. The transition from the absolute ground state $[Ar]3d^{10}4s^24p^6$ to the first excited state can be driven with 124 nm light, which is a longer wavelength than what is required for argon. Although it can not be feasibly be produced by continuous laser light, the needed photons can be generated by a plasma outside the vacuum [56]. With an additional 819 nm photon the metastable state $5s[3/2]_2$, marked in blue, can be populated [31]. In this thesis an rf-generated plasma was used for this. The cooling transition from the metastable state to the excited state $5p[5/2]_3$ is a closed transition at 811 nm and shown by a solid, orange line. The green dashed line represents another transition from the metastable state which is called the quench transition. Similar to argon, it excites the atoms with 810 nm light from $5s[3/2]_2$ to $5p[5/2]_2$. From this excited state the atoms can fall back to the ground state by emission of a 877 nm photon. Figure adapted from [53].

the experiments discussed in this work, the meta-stable state was produced in an rf-driven plasma using the same source design as for the argon excitation which is a common approach in ATTA [53, 59].

Once the meta-stable state $5s[3/2]_2$ is reached atoms can be excited to the state $5p[5/2]_3$ by laser light of 811 nm wavelength [53]. This transition is closed due to the selection rule $\Delta J = 0, \pm 1$. A quench transition is possible in krypton and employed

at other experiments [59] but not in this thesis.

The in this thesis studied isotopes ^{83}Kr and ^{85}Kr both feature a nuclear spin of

isotope	cooler frequency shift relative to ^{84}Kr [MHz]	sideband number	sideband shift relative to cooler [MHz]
^{81}Kr	656	1st RP	963
		2nd RP	1454
^{83}Kr	783	1st RP	870
		2nd RP	1489
^{85}Kr	870	1st RP	947
		2nd RP	1558

Table 2.4: Frequency shift of krypton isotopes relative to the most abundant isotope ^{84}Kr. Also shown is the relative frequency shift of the first two repumper transitions [56].

$I = 9/2$ resulting in the splitting of the energy spectrum into substates denoted by $F = |I - J|, |I - J| + 1, ..., |I + J|$. This is shown for the cooling ground and excited state in figure 2.4. The ground state splits into five substates with $F_g = 13/2, 11/2, ..., 5/2$ the excited state into seven states $F_e = 15/2, 11/2, ..., 3/2$. For cooling the closed transition $5s[3/2]_2(F = 13/2) \rightarrow 5p[5/2]_3(F = 15/2)$ is chosen. As for argon other hyperfine levels can be populated as well due to the small energy splitting. Repumpers re-populate the ground state whereas the current setup employs two of these transitions. Their frequency shift to the cooling transition is displayed in figure 2.4 and for overview again in table 2.4 below.

Other krypton specific values are displayed in tables 2.5 and 2.6 and will be used in the following sections for theoretical studies of the processes in the KrypTTA machine.

2.5 Theoretical investigation of a Zeeman Slower for Krypton

The setup of a D-ATTA machine allows for a subsequent (or for future realizations simultaneous) counting of rare krypton and argon radioisotopes. To achieve this, the apparatus needs to be optimized for ^{39}Ar capture since these count rates are typically much smaller. Therefore the Zeeman slower (ZSL) coil for argon must also be used for krypton. Compared to other magnetic fields like the 3D or 2D MOT the ZSL optimum differs strongly between argon and krypton and therefore needs a special treatment. This can be best understood with table 2.5, which shows that the maximal deceleration a_{max} is less than half as strong for krypton than for argon. Since the Zeeman slower needs to achieve the highest velocity reduction in the whole

	argon	krypton
ground state	$4s[3/2]_2$	$5s[3/2]_2$
excited state	$4p[5/2]_3$	$5p[5/2]_3$
$\gamma/2\pi$ [MHz]	5.87	5.56
τ [ns]	27.09	28.63
λ [nm]	811.75	811.52
maximal deceleration a_{max} [10^5 m/s^2]	2.27	1.02
meta-stable state lifetime [s]	60	85
J_g	2	2
J_e	3	3
$^c g_{J,g}$	1.5012	1.5021
$^c g_{J,e}$	1.3341	1.3341
$^m g_{J,g}$	1.5009 [60]	1.502 [61]
$^m g_{J,e}$	1.3335 [60]	1.336 [61]

Table 2.5: Relevant features of argon and krypton for laser cooling and trapping. Values were taken from [46] unless stated otherwise. The superscripts c and m for the Landé-factors indicate a calculated or measured value, respectively.

	^{39}Ar	^{83}Kr	^{85}Kr
I	7/2	9/2	9/2
$m_{F,g}$	11/2	13/2	13/2
$m_{F,e}$	13/2	15/2	15/2
μ_I [μ_K]	-1.588 [62]	-0.97073 [63]	-1.0055 [64]
g_I	-0.4537	-0.2157	-0.2234
$g_{F,g}$	0.5459	0.4621	0.4621
$g_{F,e}$	0.6156	0.5343	0.5343

Table 2.6: Addition to table 2.5 for the in this thesis used radio-isotopes of odd mass number. The values are taken from [46] unless stated otherwise.

apparatus by far with $\sim 500\,\text{m/s}$ the deceleration difference is most apparent there. Although the number of windings and coil length are fixed it is still possible to change the ZSL laser detuning and the coil current. In order to find the optimal settings for krypton the theoretical description is discussed first.

 In the ZSL the atoms are cooled longitudinally from their initial velocity v_i to the final velocity v_f. In the ArTTA machine, an increasing field slower is realized. In this setup, the magnetic field of the slower increases with growing distance from its entrance and is therefore maximal at the slower exit and zero at its beginning. This results in a high detuning of the ZSL laser beam so that the beam is resonant with the fast atoms coming directly from the source.
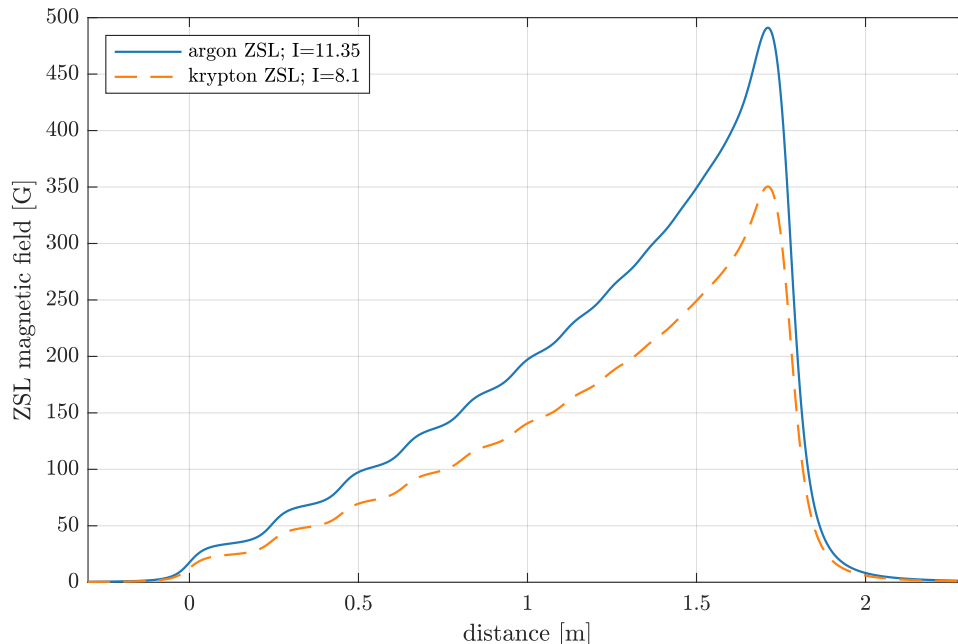
Figure 2.6: Magnetic field in the ZSL over distance for two different current settings. The magnetic field is calculated with the Biot-Savart law and the known positions and lengths of the coil windings. The distance is measured from the beginning of the ZSL coil, the MOT position is roughly at 1.8 m. Note that this is only the ZSL field, without the compensation coil or MOT magnetic field. The solid line displays the field for a current of $I = 11.35\,$A which is optimized for ^{39}Ar capture. The dashed line represents the typical ZSL current for ^{85}Kr detection which is $I = 8.1\,$A.

The biggest challenge in designing a ZSL is to take care that the atoms are not lost from the cooling cycle. Due to the spontaneous emission process with time constant γ, the amount of scattered photons per time - and therefore the deceleration - is limited. With equation 2.24 one finds the maximum deceleration a_{max} to be

$$a_{max} = \frac{\hbar k \gamma}{2m} \frac{s_0}{1 + s_0} \tag{2.38}$$

with the wave vector of the laser k, the saturation parameter s_0, and the mass of the atom m. Saturating the transition with a large s_0 simplifies this to

$$a_{max} = \frac{\hbar k \gamma}{2m}. \tag{2.39}$$

As previously discussed and displayed in equation 2.23 the frequency of an atomic transition can be tuned by the use of magnetic fields. In the case of the ZSL the magnetic field B is used to let the atom stay in resonance with the laser, canceling the Doppler shift of equation 2.19 at any point in the slower. Combining both shifts with the laser detuning δ results in the resonance condition

$$0 = \delta + kv(z) + \frac{\mu'}{\hbar}B(z) \tag{2.40}$$

which has to be fulfilled for all positions z inside the slower.

Using a constant deceleration a_B imposed by the magnetic field results in the following velocity profile[4]

$$v(z) = \sqrt{v_i^2 - 2a_Bz}, \text{ for } z \leq z_{max} = \frac{v_i^2 - v_f^2}{2a_B} \overset{v_i^2 \gg v_f^2}{\approx} \frac{\Delta v^2}{2a_B}. \tag{2.41}$$

The desired velocity difference $\Delta v = v_i - v_f$ therefore directly sets the length of the slower coil z_{max}. This velocity trajectory allows rewriting of the resonance condition 2.40 to obtain

$$B(z) = \frac{\hbar}{\mu'}\left(-\delta - k\sqrt{v_i^2 - 2a_Bz}\right). \tag{2.42}$$

An additional constraint on the setup is the maximal deceleration a_{max} of the atom due to the scattering processes, presented in equation 2.39. It may not be smaller than the deceleration required by the slope of the magnetic field which is found by taking the derivative of the magnetic field $B(z)$ in equation 2.42

$$\frac{\mathrm{d}B(z)}{\mathrm{d}z} = -\frac{\hbar k}{\mu'}\frac{\mathrm{d}v(z)}{\mathrm{d}z} = -\frac{\hbar k}{\mu'}\frac{\mathrm{d}v(z)}{\mathrm{d}t}\frac{\mathrm{d}t}{\mathrm{d}z} = -\frac{\hbar k}{\mu'}a_B\frac{1}{v(z)}. \tag{2.43}$$

With the maximal deceleration a_{max} the condition

$$\left|\frac{\mathrm{d}B(z)}{\mathrm{d}z}\right| \leq \frac{\hbar k}{\mu'}a_{max}\frac{1}{v(z)} \tag{2.44}$$

is found. This prevents the magnetic field from becoming too steep so that the atoms can not follow with the cooling.

To counteract possible imperfections in the system, such as jumps in the magnetic field due to discrete winding numbers as can be seen in figure 2.6, a 'fudge-factor' ξ is introduced which typically ranges between 0.4 and 0.7 [65, 51]. This reduces a_{max} to a feasible real deceleration $a_r = a_{max}\xi$.

The detuning δ needs to be carefully chosen to not let the required deceleration exceed the previously set a_r. To evaluate this, equations 2.40 and 2.44 are combined

---

[4]There are Zeeman slower designs which do not hold the deceleration constant [65].

[54] to find the required deceleration at each point $a_r(z)$:

$$a_r(z) = a_{max}\xi \geq \left|\frac{\mathrm{d}B(z)}{\mathrm{d}z}\right| \frac{\mu'}{\hbar k} v(z) = \left|\frac{\mathrm{d}B(z)}{\mathrm{d}z}\right| \frac{\mu'}{\hbar k^2} \left(-\frac{\mu' B(z)}{\hbar} - \delta\right). \qquad (2.45)$$

Each predefined initial velocity v_i and resulting δ now generates a maximal required deceleration which is the highest value of the profile $a_r(z)$. The magnetic field $B(z)$ is given in equation 2.42. Still, the final velocity of the atoms emerging the slower, v_f needs to be fixed.

For argon $\delta_{ZSL,Ar} = -746\,\text{MHz}$ and therefore $v_{i,Ar} = -\delta/k = 606\,\text{m/s}$. The slower current is set to $11.35\,\text{A}$ resulting in the magnetic field shown in figure 2.6 with a maximal magnetic field of $B_{max} = 491\,\text{G}$. Therefore the final velocity $v_{f,Ar}$ can be determined as $v_{f,Ar} = 49\,\text{m/s}$ with equation 2.40. These values apply to ^{39}Ar and were optimized with a sample highly enriched in this isotope [35].

However, the capture velocity of the MOT is only $v_{c,Ar} = 10\,\text{m/s}$ [66]. Typically the ZSL exit velocity v_f is chosen just below this to ensure a high fraction of the atoms being captured in the trap.

In the ArTTA apparatus v_f is deliberately chosen to be higher than $v_{c,Ar}$ to ensure that the remaining transversal velocity of the atoms emerging from the ZSL does not result in a spatial spreading of the atom beam. Instead the atoms are cooled with an additional laser beam which overlaps the ZSL beam. This booster beam acts together with the rising edge of the MOT magnetic field as a second short Zeeman slower which slows the atoms down to the MOT capture velocity. The slightly higher v_f suppresses the spread behind the slower and results in a higher capture efficiency. For krypton the booster frequency will be used as well with the unaltered argon detuning of $\delta_{booster,Ar} = \delta_{booster,Kr} = -26\,\text{MHz}$.

The final velocity $v_{f,Kr}$ of the krypton atoms emerging from the slower is calculated via $v_{f,Ar}$. Since MOT and booster will be at the same frequency and magnetic field, the gradient will be the same, just the difference in maximal deceleration between argon and krypton has to be taken into account. Equation 2.44 is also valid in the MOT and can therefore be rewritten to obtain

$$v_f = \frac{\hbar k}{\mu'} a_{max} \left|\frac{\mathrm{d}B}{\mathrm{d}z}\right|^{-1} \Rightarrow v_{f,Kr} = \frac{k_{Kr} a_{max,Kr} \mu'_{Ar}}{k_{Ar} a_{max,Ar} \mu'_{Kr}} v_{f,Ar}. \qquad (2.46)$$

With the values for μ' and a from table 2.6 the final velocity is calculated to $v_{f,Kr} = 22.2\,\text{m/s}$.

Now the maximal deceleration inside the slower can be calculated and from this the fudge-factor ξ is determined. Figure 2.7 shows this calculated ξ in a krypton ZSL for different detunings δ and resulting initial velocity $v_i = -\delta/k$. For argon ξ is set to 0.44 which is reached for krypton with $\delta \approx 660\,\text{MHz}$ and $v_i \approx 540\,\text{m/s}$. Whether this is below the typical initial longitudinal velocity can be calculated via
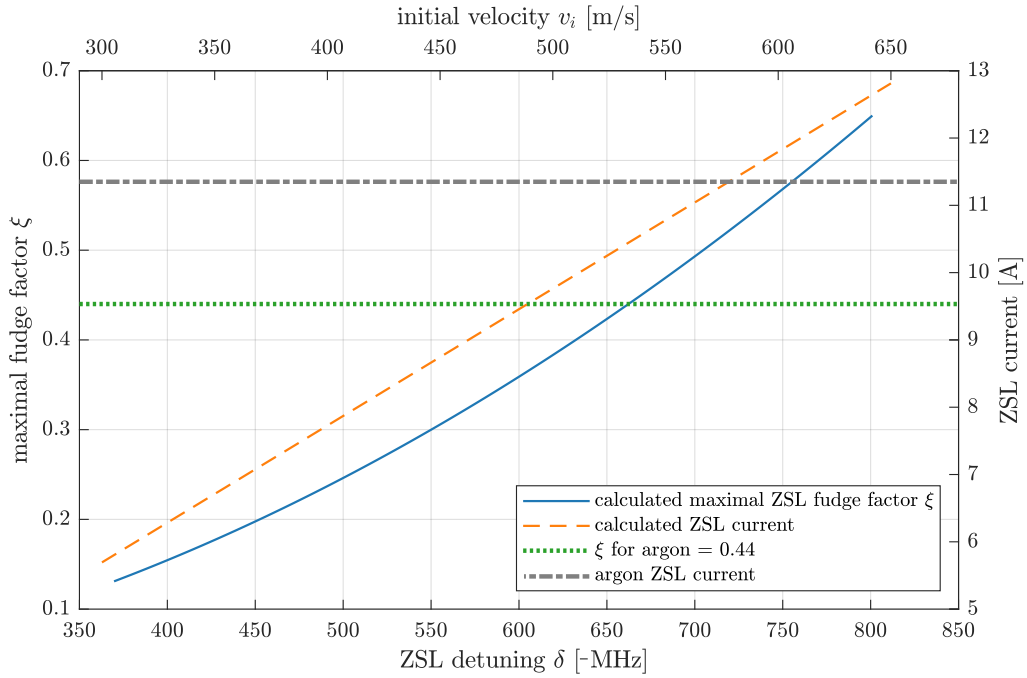
Figure 2.7: Calculated Zeeman slower parameters for krypton capture. The solid line shows the from equation 2.45 calculated maximal required fudge factor ξ for various ZSL laser detunings δ. The initial velocity v_i for each δ is calculated via $v_i = -\delta/k$. The dotted horizontal line shows ξ for argon which is $\xi_{Ar} = 0.44$. This limit is reached with krypton for a detuning of 660 MHz and initial velocity of 540 m/s. The orange, dashed line represents the required calculated magnetic coil current to achieve the deceleration of the atoms to the final velocity 22 m/s. The horizontal dotted/dashed line marks the current of $I_{Ar} = 11.35$ A employed for argon.

the plasma temperature of ~ 400 K [51] and krypton atom mass. This results in

$$v_{i,Kr}^2 = \frac{3k_B T}{m_{Kr}} \approx 340 \, \text{m/s} \tag{2.47}$$

showing that longitudinal cooling of krypton is feasible when adjusting the argon Zeeman slower in current and detuning.

Figure 2.7 also shows the calculated magnetic field current needed to slow the atoms of initial velocity v_i to the set final velocity of $v_f = 22$ m/s. At the argon current of $I = 11.35$ A the magnetic field slope is so steep that the fudge factor for krypton increases to 0.55 which may already be high enough to lose some atoms

from the cooling cycle. However, the experimental treatment of figure 2.7 will follow in section 6.1.

2.6 Sideband Generation with an EOM

The necessity for repumping sidebands was discussed previously and displayed in figure 2.4. In the ArTTA apparatus these side-bands for ^{39}Ar are produced by acousto-optical modulators (AOMs) which are a standard tool for shifting the frequency of a laser beam. The principle and implementation of these components is extensively discussed in [67, 68], and also for ArTTA in [52].

For side-band generation in the KrypTTA apparatus an electro-optical modulator (EOM) is used [53]. These devices can directly modulate the desired repumper frequencies onto a carrier laser beam and therefore compact the laser system. It generates the additional frequencies via phase variation of the input. The underlying theory will be shown here, based on [67] and [69].

Applying an electric field on an optical medium can change positions, orientations or shapes of the molecules inside it. Considering an anisotropic material where the effects of this electrical field vary depending on the orientation of the medium, one can modify the refractive index n of this material with the applied electric field strength $|\vec{E}| = E$, yielding $n(E)$. This tunability can be used for various applications, such as amplitude, phase or polarization variation of a laser beam.

This variation is typically very small, therefore $n(E)$ can be evaluated with a Taylor expansion about $E = 0$

$$n(E) \approx n(0) + \frac{\mathrm{d}n}{\mathrm{d}E}\bigg|_{E=0} E + \frac{1}{2}\frac{\mathrm{d}^2n}{\mathrm{d}E^2}\bigg|_{E=0} E^2 + ... \tag{2.48}$$

which is usually rephrased with two newly defined coefficients r and s to obtain

$$n(E) \approx n - \frac{1}{2}rn^3E - \frac{1}{2}sn^3E^2 + ... \tag{2.49}$$

with

$$n = n(0) \ , \ r = -\frac{2}{n^3}\frac{\mathrm{d}n}{\mathrm{d}E}\bigg|_{E=0} \text{ and } s = -\frac{1}{n^3}\frac{\mathrm{d}^2n}{\mathrm{d}E^2}\bigg|_{E=0}. \tag{2.50}$$

Higher orders of the expansion can safely be neglected. From this expansion one can derive two effects on a mediums refractive index:

- **Pockels effect:** The refractive index changes proportionally with the electric field strength E. Therefore equation 2.49 simplifies to

$$n(E) = n - \frac{1}{2}rn^3E. \tag{2.51}$$

- **Kerr effect:** The refractive index changes proportionally with the squared electric field strength E^2, equation 2.49 becomes

$$n(E) = n - \frac{1}{2}sn^3E^2. \tag{2.52}$$

Usually, this effect is much smaller than the Pockels effect, therefore it is only observable if $r = 0$ due to symmetry restrictions.

Typical values for r lie in the range of 10^{-10} to 10^{-12} m/V, for s between 10^{-18} to 10^{-14} m^2/V^2 [67]. EOMs are Pockels cells which are dominated by the Pockels effect. Since this section aims to investigate the processes in these EOMs the parameter s is set to zero and only equation 2.51 is considered.

Figure 2.8 shows the EOM as a Pockels cell of length L. The phase modulation
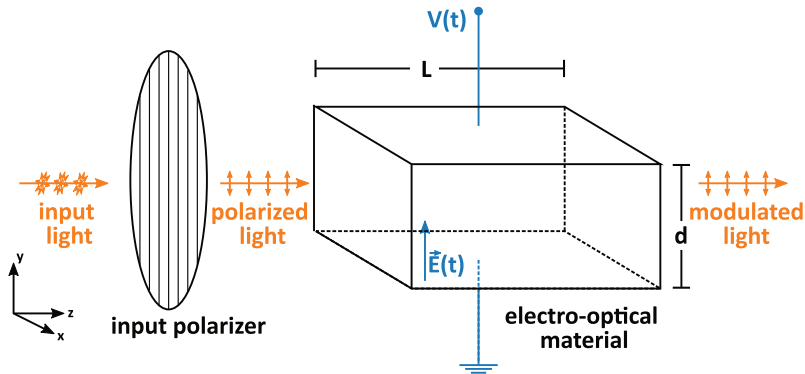
Figure 2.8: Schematic setup of an electro-optical phase modulator. The input laser travels in positive z direction. First it is parallel polarized by the input polarizer. After that the light enters the electro-optical medium on which an oscillating voltage $V(t)$ is applied. The resulting modulated electric field $\vec{E}(t)$ in the EOM causes a phase shift on the light which then generates sidebands of the modulation frequency ω_m. The strength of the modulation can vary the intensities between carrier (ω_l) and sidebands.

is achieved by modulating the voltage applied on the electro-optical crystal with the frequency ω_m. This results in $V(t) = V_0 \sin(\omega_m t)$ and in an oscillating electric field strength $E(t) = E_0 \sin(\omega_m t)$ across the cell. A linear polarizer in front restricts the input electric light field to $E_l = E_{0,l}e^{i\omega_l t}$ and a linear polarization. As light of wavelength λ and corresponding wave vector $k = 2\pi/\lambda$ travels through an EOM of

length L it accumulates a phase shift which is given by

$$\phi(t) = n(E)kL = -\frac{1}{2}rn^3 E_0 \sin(\omega_m t)kL = \pi\frac{rn^3 L}{d\lambda}V_0 \sin(\omega_m t) \quad (2.53)$$
$$\equiv \pi\frac{V_0}{V_\pi}\sin(\omega_m t) \equiv m\sin(\omega_m t)$$

with equation 2.51. The newly defined V_π is the half-wave voltage which is the amount needed to gain a phase shift of π. The parameter m is the so-called modulation depth

$$V_\pi = \frac{d\lambda}{Lrn^3} \text{ and } m = \pi\frac{V_0}{V_\pi}. \quad (2.54)$$

The time evaluation of the laser light can now be written with the time dependent phase $\phi(t)$ to read

$$E_{0,L}e^{i\omega_l t + \phi(t)} = E_{0,L}e^{i\omega_l t + m\sin(\omega_m t)}. \quad (2.55)$$

Using the Jacobi-Anger expression this can be rewritten with the Bessel functions to obtain

$$E_{0,L}e^{i\omega_l t + m\sin(\omega_m t)} = E_{0,L}e^{i\omega_l t}\left(J_0(m) + \sum_{k=1}^{\infty}J_k(m)e^{ik\omega_m t} + \sum_{k=1}^{\infty}J_k(m)e^{-ik\omega_m t}\right)$$
$$(2.56)$$

which is a carrier of frequency ω_l accompanied by sidebands of frequency $\omega_l \pm k\omega_m$ with $k \in \mathbb{N}$. The intensities of carrier and sidebands can be regulated by tuning m and therefore the amplitudes of the Bessel functions. For example can m be tuned to obtain $J_0(m) = 0$ resulting in the suppression of the carrier mode. This can be seen on the right side of figure 2.9.

 In the KrypTTA apparatus the laser beam carrier will be the cooling laser and the sidebands will be tuned to the repumper transitions. Therefore $J_0(m)$ and $J_1(m)$ of the carrier and first order sidebands should be large while higher modes are suppressed. The current realization implements two repumping side-bands for the isotopes ^{85}Kr and ^{83}Kr. Therefore two frequencies ω_{m1} and ω_{m2} are applied on the EOM voltage resulting in

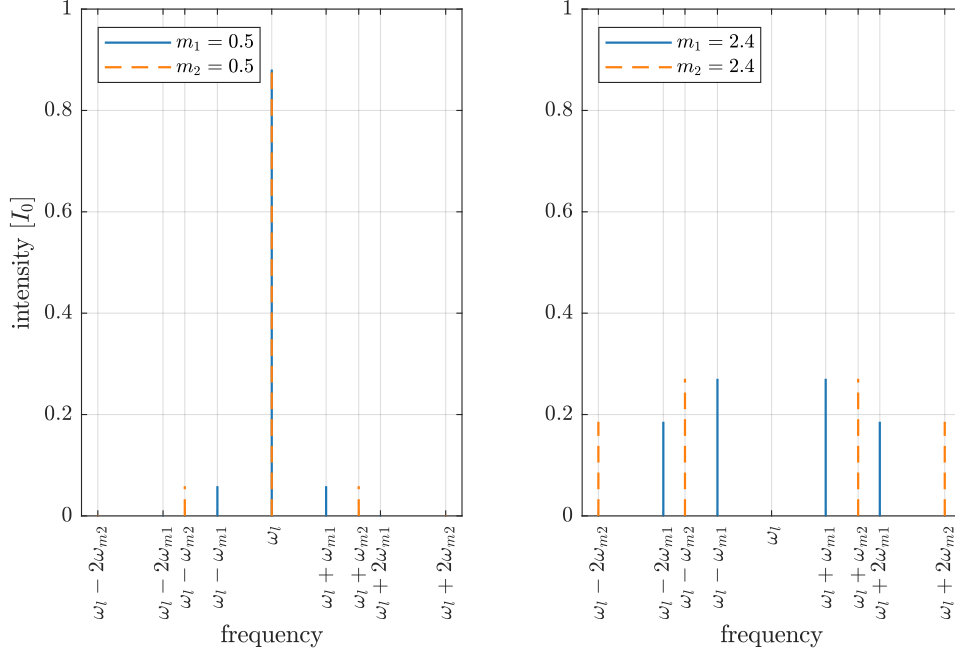$$V(t, \omega_{m1}, \omega_{m2}) = V_1\sin(\omega_{m1}t) + V_2\sin(\omega_{m2}t). \quad (2.57)$$

Figure 2.9: Laser power of the carrier and sidebands after passing an EOM which is modulated with two different frequencies ω_{m1} (solid lines) and ω_{m2} (dashed lines). These generate the repumping lasers. The left side shows the configuration for ^{85}Kr and ^{83}Kr cooling which requires the carrier and first order sideband. The right side demonstrates how the carrier can be suppressed by tuning the modulation depth m.

Analogous to equation 2.56 the electric field of the incoming light is modulated to

$$
E_{0,L}e^{i\omega_l t + m_1\sin(\omega_{m1}t) + m_2\sin(\omega_{m2}t)} = \tag{2.58}
$$

$$
E_{0,L}e^{i\omega_l t}\Bigg(J_0(m_1) + J_0(m_2) + \sum_{k=1}^{\infty}J_k(m_1)e^{ik\omega_{m1}t} + \sum_{k=1}^{\infty}J_k(m_1)e^{-ik\omega_{m1}t}
$$

$$
+ \sum_{n=1}^{\infty}J_n(m_2)e^{in\omega_{m2}t} + \sum_{n=1}^{\infty}J_n(m_2)e^{-in\omega_{m2}t}\Bigg).
$$

The light intensity I is proportional to the squared electric field and can be calculated with equation 2.58 to obtain the values displayed in figure 2.9. The experimental realization of this will be discussed in section 4.2.3.

2.7 Radioisotope dating

The detection of rare isotopes is certainly a nontrivial step towards age information on a sample. However, after the desired count rate, activity or concentration is obtained, the calculation of the sample's age follows. This is achieved by employing the exponential decay of the isotope's concentration in a sample. If the amount of the radio-active atoms at the time of sample origin t_0 is $N(t_0) = N_0$ then the atom number at the measurement time t_m is given by the exponential decay

$$N(t_m) = N_0\, e^{-(t_m-t_0)/\tau} = N_0\, e^{-t/\tau}$$
$$t \equiv t_m - t_0 \tag{2.59}$$

with the mean lifetime of the isotope τ. The sample age t is given as the time span between origin t_0 and measurement t_m. The half-life $T_{1/2}$ and τ are connected via

$$\tau = \frac{T_{1/2}}{\ln(2)}. \tag{2.60}$$

Knowing the half-life $T_{1/2}$, the initial atmospheric atom amount N_0, and the number of atoms in the sample $N(t_m)$, the age t can be directly calculated with equation 2.59.

The atmospheric concentration which typically directly determines N_0 is constant for the radioisotopes ^{39}Ar and ^{81}Kr [14]. This simplifies the dating process since any reference sample can be used to provide N_0 in equation 2.59 and no further background information is required.

2.7.1 The ^{85}Kr dating process

Although the radioisotope ^{85}Kr is produced by cosmic radiation [70], its anthropogenic input is much higher. Since the dawn of the atomic era in 1945 the atmospheric concentration of ^{85}Kr increased by six orders of magnitude [14].

This steady increase of radio-krypton budget in the atmosphere complicates ^{85}Kr dating with equation 2.59. In the case of this radio-isotope, the initial atom number N_0 is not constant which is why care in referencing and age determination needs to be taken. A profound knowledge on the ^{85}Kr concentration in air is necessary.

^{85}Kr input curve

The dominance of fissiogenic input results in a non-constant ^{85}Kr amount over time. Continuous investigation of atmospheric samples at different locations in the world is needed to create an archive of ^{85}Kr activities. These measurements provide the baseline from which dating of krypton samples can be realized. Considering equation
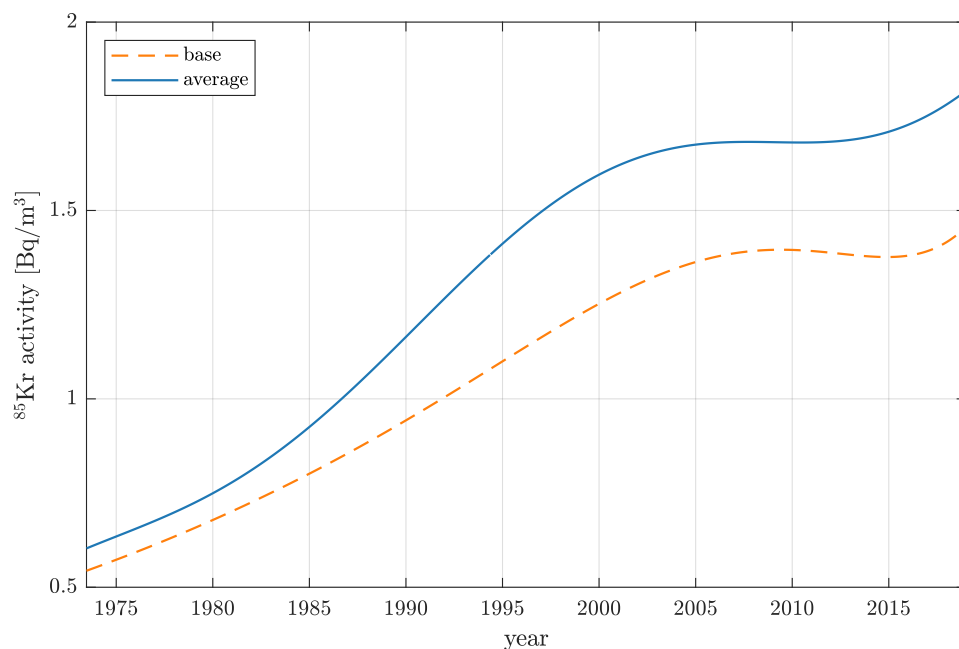
Figure 2.10: ^{85}Kr activity measured by eleven stations in Europe over the course of four decades. The increase of activity over time becomes apparent and is caused by a rise in the radioisotope's concentration. The dashed, orange curve represents the base line of activity obtained with the lowest measured activities and gives a lower bound. The solid, blue line shows the averaged ^{85}Kr activity measured in Europe. Since fluctuations caused by reprocessing cycles are strong but swift, the average is typically used for ^{85}Kr dating of samples. The data was calculated and made available in [71].

2.59 these measurements give the obligatory initial atom number N_0 which, in the case of ^{85}Kr is the time dependent number $N_0(t)$.

Figure 2.10 shows the ^{85}Kr activity in atmospheric air measured by eleven stations in Europe over four decades.[5] This activity is directly connected to the amount of radio-krypton N_0 therefore both can be used interchangeably. All the obtained activities were combined to quarterly data points and made available free for download in [71]; per quarter two data points are provided which make up the base line and the average line.

The data generating the base line is calculated by combining the lowest measured activities in a three month interval, the average represents the mean of all

---

[5]Of these eleven stations were nine in Germany, one in Poland, and one in Switzerland.

detected activities. Fluctuations in measured activity can be very high, since the input varies strongly over the course of a few weeks. Spikes in ^{85}Kr concentration of up to $6\,\mathrm{Bq/m^3}$ [71] are caused by reprocessing activities in according facilities. The distribution of the radioisotope across the hemisphere is fast enough compared to the half-life to use the input curve of figure 2.10 for all samples extracted from the northern hemisphere [72, 73]. The ^{85}Kr exchange time to the southern hemisphere was calculated in [74] to be $1.25(24)\,\mathrm{a}$, using data obtained from southern monitoring stations and comparing it to the data shown in [71].

^{85}Kr dating

The radio-krypton dating method is based on the data provided by [71] and equation 2.59. Since the initial ^{85}Kr amount $N_0(t)$ is given in figure 2.10 as the isotope's activity in atmospheric air, the calculation of sample age is also conducted with this value. Therefore equation 2.59 modifies to

$$A(t_m) = A_0(t_0)\, e^{-t/\tau} \tag{2.61}$$

with t_0 being the moment of sample enclosure from the atmosphere [72].

The activity is an inherent feature of the sample which can not be determined directly with ATTA but is obtained by comparing a measured sample count rate with a known reference count rate. The result is a relative concentration of the radio-isotope which can be transformed into its absolute activity with the data used in figure 2.10 and the known reference activity.

The extraction of sample age from a hypothetical ^{85}Kr activity is shown in figure 2.11.

The solid line of figure 2.11 again represents the average of atmospheric ^{85}Kr activity from figure 2.10. An exemplary sample activity of $A(t) = 0.40(4)\,\mathrm{Bq/m^3}$ is used to show the age determination. Employing equation 2.61 to all initial values $A_0(t_0)$ and comparing this to the 'measured' $A(t)$ yields the time t_0 at which the sample was enclosed. Figure 2.11 displays the moment t_0 as an asterisk at which the input curve and the exponential decay curve intersect. The same procedure is done for the 1σ deviation yielding an age uncertainty.

The shown example activity $A(t) = 0.40(4)\,\mathrm{Bq/m^3}$ results in a sample age of $t = 21.4(12)\,\mathrm{a}$.

^{85}Kr count rate requirements

With the equations and krypton input discussed in the previous parts ^{85}Kr dating is theoretically possible. But for feasible, viable dating with ATTA some requirements have to be met. In order to determine the conditions for krypton dating the final objectives have to be defined first. These are:
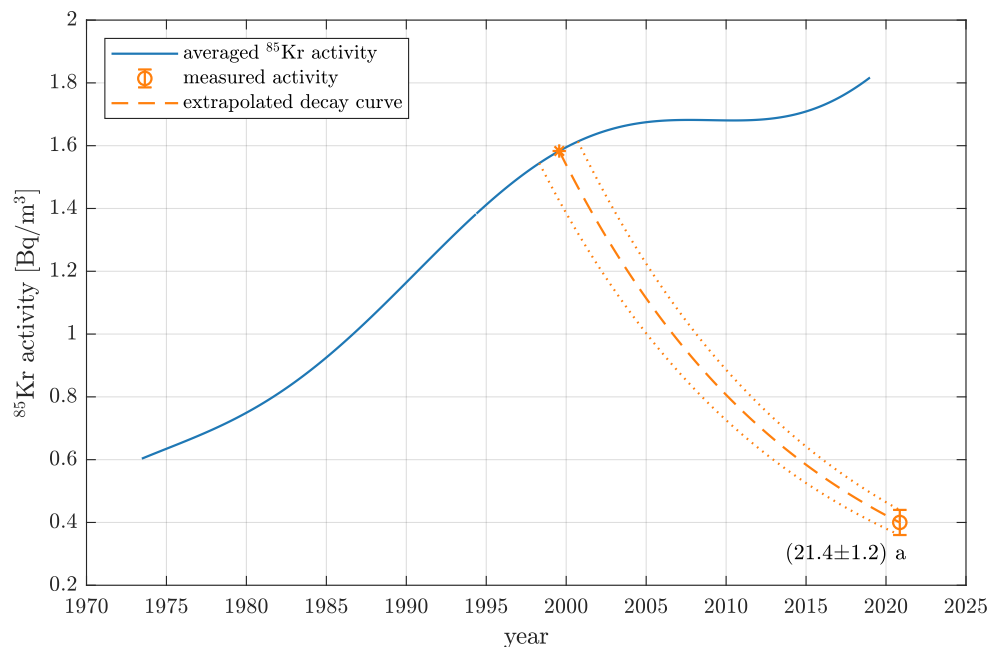
Figure 2.11: Extraction of ^{85}Kr age information from a measured sample activity. The solid, blue line represents the ^{85}Kr activity in Europe provided by [71]. The dashed, orange line shows the calculated exponential decay of the sample from its origin to the radio-krypton measurement. The intersection of the dashed line with the solid line marks this sample origin, shown here as an asterisk. The two dotted lines next to the dashed line indicate the exponential decay curves resulting from the 1σ uncertainty interval of the measured activity. The intersection of these dotted lines with the solid line compute the error of the measured sample age. The hypothetical sample has an activity of $0.40(4)\,\mathrm{Bq/m^3}$ which results together with the known ^{85}Kr input in a sample age of $21.4(12)\,\mathrm{a}$.

- ^{85}Kr dating of a sample extracted from $10\,\mathrm{L}$ of water, typically resulting in $1\,\mu\mathrm{L}$ krypton gas [75].

- A relative statistical uncertainty of $10\,\%$ for any measured sample age.

Combining these two objectives results in typical count rate requirements.

Counting a number N of single atoms is a Poisson process which is subject to a statistical error of $\sqrt{N}$, whereas a higher N results in smaller relative error. Regarding the constraints on sample size a higher count rate or detection efficiency of ^{85}Kr
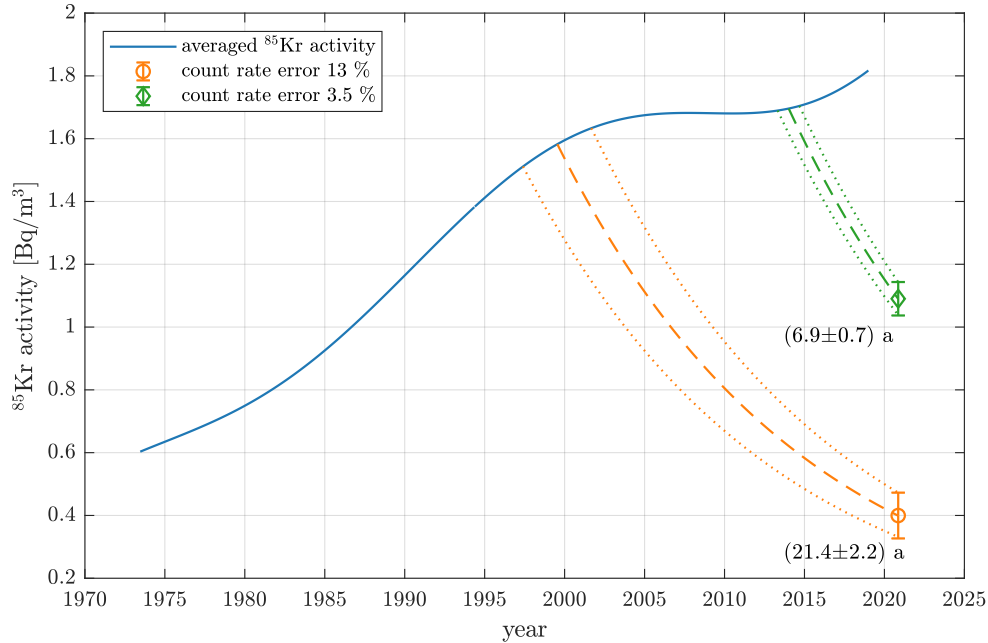
Figure 2.12: The procedure for obtaining the necessary count rate error resulting in a 10 % age error is presented. For future krypton dating applications of the KrypTTA machine a relative sample age error of 10 % is an objective. Since the ^{85}Kr dating differs from ^{39}Ar a study connecting age error and count rate error needs to be conducted first. The solid, blue krypton input curve is generated with data from [71]. Two count rate uncertainty calculations are shown here, one with a high activity of 1.1 Bq/m^3, the other one with a lower activity of 0.4 Bq/m^3. The dashed lines show the calculated exponential decay of the samples and extracts their age. As the age error should be 10 % one can now go back and infer the required error in activity and thereby count rate. The results are shown in the legend. These values are both well realizable with a count rate of ~ 100 a/h and a measurement time of < 20 h.

is also favorable since the amount of radio-krypton decreases with smaller samples. This effect can be overcome with a higher detection efficiency.

Whether the required count rate for achieving the objectives is feasible with the KrypTTA apparatus is investigated in the following. Figure 2.11 already showed the dating process for ^{85}Kr. Now a limit of 10 % relative age uncertainty is set for any determined age. The idea is to calculate back from this 10 % error to the equivalent activity error. This inaccuracy in activity is then easily transformed into a count

rate inaccuracy.

Figure 2.12 shows an example of how this inaccuracy is determined for two different activities $A_1 = 1.1 \, \text{Bq/m}^3$ and $A_2 = 0.4 \, \text{Bq/m}^3$. These are equivalent to ages of $t_1 = 6.9(7) \, \text{a}$ and $t_2 = 21.4(22) \, \text{a}$ whereas their uncertainty is already the discussed $10 \, \%$ constraint. The calculation leads to a requirement for the count rate error of $3.5 \, \%$ and $13 \, \%$ respectively.

The activity and corresponding age of $7 \, \text{a}$ was deliberately set as a lower dating limit. As the sample gets younger the $10 \, \%$ age error limit becomes even harder to achieve. The $7 \, \text{a}$ limit is well-set between a high dating resolution and feasible count rates. Its resulting $3.5 \, \%$ count rate error relates to a number of $N \approx 1000$ counted atoms. This is calculated with the Poisson statistical uncertainty $\Delta N = \sqrt{N}/N \approx 3.5 \, \%$ for $N \approx 1000$. This result denotes that 1000 atoms of the $7 \, \text{a}$ old sample need to be counted to determine its age with $10 \, \%$ statistical uncertainty.

To specify the required atmospheric count rate from this result, the activity of the sample needs to be compared to the atmospheric one. Modern air features a 1.6 times higher activity of $1.8 \, \text{Bq/m}^3$ meaning for the atmospheric reference a number of counted atoms $N_{atm} = 1.6 \cdot N_{sample} = 1.6 \cdot 1000 = 1600$ needs to be achieved. This would for example relate to an atmospheric count rate of $100 \, \text{a/h}$ and a $16 \, \text{h}$ measurement time which is well feasible.

As the sample age rises the allowed absolute age uncertainty for the $10 \, \%$ error goal increases as well. For an age of $21.4(22) \, \text{a}$, figure 2.12 shows the calculation of a relative count rate error of $13 \, \%$. This might sound easy to achieve since the error discussed before was almost 4 times smaller and still led to a feasible count rate. However, the activity of the old sample is only $0.4 \, \text{Bq/m}^3$ which is a depletion by a factor of 4.5 compared to atmosphere. This means that a count rate of $100 \, \text{a/h}$ reduces to $22 \, \text{a/h}$. Still, to achieve $13 \, \%$ counting error the Poisson statistics requires a number of counted atoms of $N \approx 100$, which could be achieved after only $4 \, \text{h}$ measurement time. While other uncertainties originate from the measured reference sample and error propagation in activity calculation the Poisson statistics of the atom counting in the sample is typically the limiting factor.[6]

In summary, counting $\sim 100 \, \text{a/h}$ for an atmospheric sample of $1 \, \mu\text{L}$ volume is a feasible objective for the KrypTTA apparatus which would meet the requirements of $10 \, \text{L}$ water sample dating with a $10 \, \%$ uncertainty.

---

[6]The results become ambiguous as soon as the ^{85}Kr activity in the atmosphere decreases.

3 Setup of ^{39}Ar detection in a new facility

The throughput of environmental samples is mainly limited by the allocation of the ArTTA machine. Currently, it takes 24 hours to measure the ^{39}Ar content of a sample including the mandatory reference. Of this time span the vast majority, 20 hours, is spent on counting radio-argon in the sample to achieve a statistical error of $\sim 10\,\%$. This measurement time can be reduced by increasing the count rate of ^{39}Ar, for which various approaches have been examined, like optical pumping from another meta-stable state to the desired one [76, 77], the expansion to higher trapping velocities in the MOT by using a second laser frequency [78], and the utilization of the bichromatic force as a first, strong cooling stage directly behind the diffusive source [79, 80].

However, the setup of a second ArTTA machine opens the possibility to directly double the sample throughput. To ensure stability whilst maintaining flexibility, the second ArTTA apparatus was built inside of a shipping container in a large hall. The container was, in a first step, set up for the cooling and trapping of ^{40}Ar and also ^{84}Kr in a MOT, which was demonstrated in the PhD thesis of Zhongyi Feng [52].

This thesis continues the previous work and extends the ArTTA machine to enable single atom detection of ^{39}Ar. This chapter begins with a review of the ArTTA apparatus and a description of the laser system finalization. In the following sections, the design and integration of monitoring devices for the meta-stable argon density and flux are discussed. These are crucial elements for a machine performance monitoring. The chapter concludes with the setup for single atom detection and its first application on ^{39}Ar.

3.1 Overview of the ArTTA machine

Figure 3.1 shows a schematic of the ArTTA apparatus realized in the laboratory container. It includes both the vacuum setup and the atomic-optical tools used for the atom cooling and trapping. Note that the schematic of the vacuum is not complete but only shows the most important parts. The fore-vacuum for sample preparation and pumping of the main chamber lacks the exact details and realization, but all turbo pumps and most important vacuum parts are visible, so that the main setup can be understood.

In the following the components of the apparatus will be individually introduced from left to right in figure 3.1.
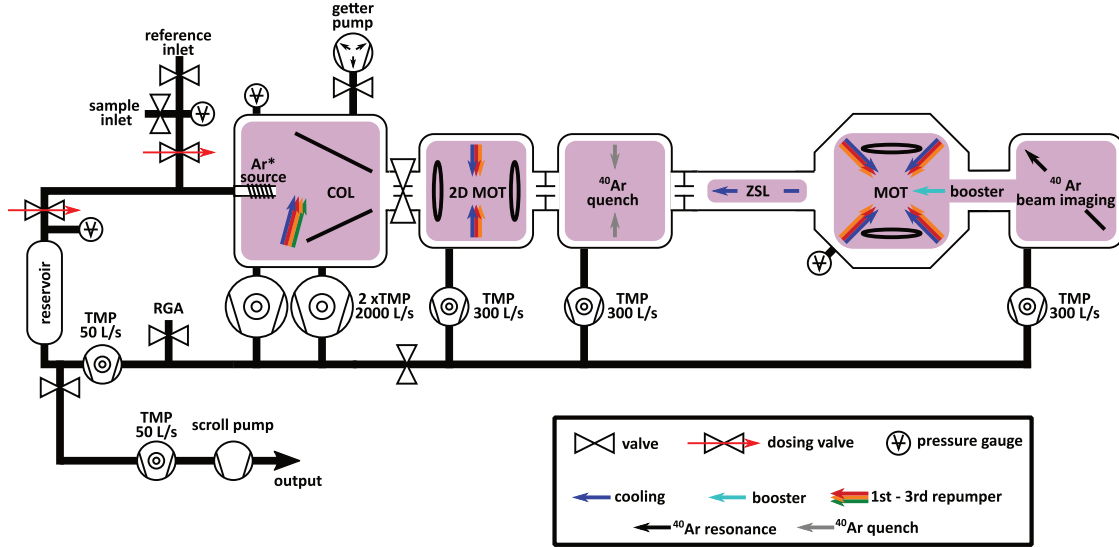
Figure 3.1: Schematic of the container ArTTA apparatus. The figure is taken from [52] and has been slightly modified to also include the modifications applied in this thesis. The argon gas is prepared at the sample inlet and is then led into the vacuum chamber which is pumped by turbo-molecular pumps (TMPs). The Ar* source produces meta-stable argon, which is transversely cooled by the collimator. After this, the 2D MOT, or magneto-optical lens (MOL), is used to focus the collimated beam onto the MOT trapping region. The next vacuum chamber features the ^{40}Ar quench, which was designed and built in during this thesis. It is used to reduce the background of meta-stable atoms in the MOT chamber and enables a continuous measurement of meta-stable ^{40}Ar flux. After this, the ZSL cools the atoms longitudinally, the booster acts as a second ZSL together with the MOT magnetic field. The atoms can either be trapped in the MOT, or, in the case of ^{40}Ar, it is also possible to examine the cross-section of the atom beam with the ^{40}Ar beam imaging instead.

Vacuum system

Since the pressure in the MOT at the end of the vacuum system should be as small as possible while maintaining a high gas amount for the ignition of a plasma, the source chamber is pumped by two very large 2000 L/s turbo pumps. To reach a pressure of $\sim 5 \times 10^{-8}$ mbar in the MOT, all vacuum chamber connections along the atom beam axis feature a differential pumping stage, which is a tube with a diameter of 18 mm that only lets atoms with a limited transversal velocity pass. Due to the collimator and magneto-optical lens (MOL) the desired meta-stable atoms are over-represented

in this directed atom beam. Additionally, each chamber is pumped with a $300\,\mathrm{L/s}$ turbo pump. After the sample gas is pumped from the main chamber, it passes a residual gas analyzer (RGA) studying its composition before it is compressed by a $50\,\mathrm{L/s}$ TMP into the reservoir. From this reservoir the sample expands back into the Ar* source and the pumping cycle starts again. This so-called recycling mode significantly reduces the needed gas amount for an ArTTA analysis.

Plasma discharge source

From the sample or reference inlet the to-be-examined gas expands into the main chamber. There it passes through the plasma discharge source which produces meta-stable argon (Ar*). To achieve a high pressure in the discharge, the gas enters the vacuum chamber trough a long isolating tube (Al_2O_3, $18\,\mathrm{cm}$) with a small cross section ($10\,\mathrm{mm}$). Across the last $5\,\mathrm{cm}$ of this tube, an rf-antenna is wound to generate the rf-field for the plasma. At the final $4\,\mathrm{mm}$ of the tube, this antenna is wound more tightly to locally enhance the rf-power. This boost causes more ions and therefore more meta-stables to form at the exit of the tube, where they directly fly into the vacuum chamber. Before the antenna, the tube is enclosed by a stainless steel can filled with liquid nitrogen. This shifts the velocity distribution of the meta-stables towards lower values and also increases the meta-stable density [51].

A picture of the source can be found in figure 3.2a) which was taken from [66]. One can see the flange on which the source is mounted, the stainless steel tubes for liquid nitrogen throughput, and the self-wound rf-coil at the exit of the tube.

Collimator

In the same vacuum chamber directly behind the source, the collimator (COL) cools the atoms transversely. The detailed setup of the COL is described in [35] and [52]. A drawing is found in figure 3.2 b), taken from [66]. It is composed of two pairs of facing mirrors, between which the cooling beam is reflected. The Doppler shift while cooling is overcome by the varying angle between atoms and laser beam. The exact angle can be tuned anytime from the outside by stepper motors on the mirror mounts (seen in red and silver in 3.2 b)). In order to pump all the meta-stable atoms into the desired ground state right at the beginning, the collimator for ^{39}Ar needs all three available repumpers.[1]

Magneto-optical lens

After the collimator, the atoms are focused into the MOT trapping region by a 2D MOT, which is often referred to as the magneto-optical lens (MOL). Its cooling laser

---

[1]Actually, a fourth repumper is also possible, but is not realized in the ArTTA system. This is because the caused flux increase is only marginal and does not justify the additional effort which results in higher laser system complexity and a decrease in reliability.

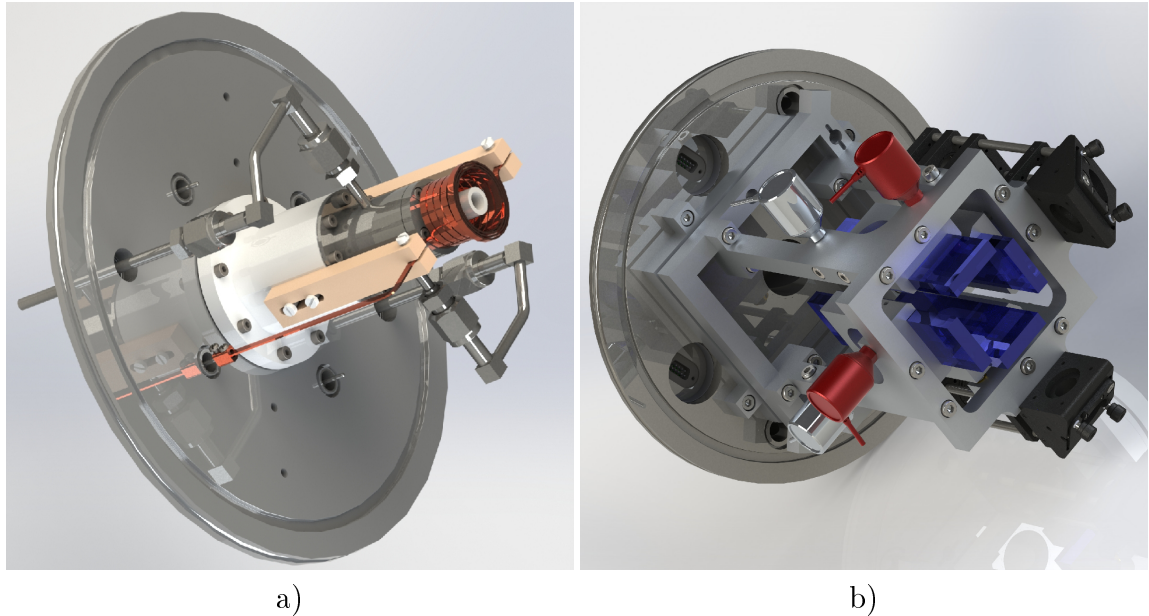a)   b)

Figure 3.2: Illustration of a) the rf-source and b) the collimator. Both pictures are taken from [66]. a) The source is mounted on an ISO 320 flange. The antenna is self-wound from $1\,\mathrm{mm} \times 4\,\mathrm{mm}$ flat copper wire (orange). It is fixed to its position by two vertical holders machined from rescor 914, a sputter resistant ceramic. Liquid nitrogen continuously flows through the stainless steel can beneath the copper wire. The two connectors to the sides are connected to the liquid nitrogen reservoir and exhaust, respectively. b) The collimator is mounted on an ISO 320 flange as well. The laser light enters through vacuum fiber connectors. The two cooling beams are shaped to rectangular cross sections by the optics built into the cage systems on each collimator axis side (black). The beam is then reflected between two opposing mirrors (blue, $\sim 16\,\mathrm{cm}$ long). The angle between the mirrors can be adjusted at any time from the outside with stepper motors (red and silver).

detuning is exactly the same as for the 3D-MOT. The first and second repumper are used here to prevent the loss of atoms into other hyper-fine states by non-resonant scattering.

^{40}Ar quench

Behind the MOL the ^{40}Ar quench is used to reduce the background of meta-stable atoms in the MOT chamber. Although the cooling laser in the MOT is resonant on ^{39}Ar, $\sim 500\,\mathrm{MHz}$ from the resonance in ^{40}Ar, the huge amount of these abundant isotopes scatters many photons off-resonantly and causes a background signal in the

detection chamber. The quench laser excites another transition (see chapter 2) in ^{40}Ar from which the atoms can de-excite into a non-meta-stable state. From this state, they can fall back to the ground state.

The quench also enables a continuous measurement of meta-stable ^{40}Ar flux. Every de-excited atom emits a photon at 843 nm. Detecting this fluorescence yields a direct and absolute measure of meta-stable ^{40}Ar density. The quench setup is also used in the original ArTTA system [35], but was re-designed and built into the container during this thesis. It will be extensively discussed in section 3.4.

Zeeman slower

In a 1.8 m long tube, the ZSL cools the atoms longitudinally, while an increasing magnetic field cancels the Doppler shift by employing the Zeeman effect introduced in section 2.2. With this the atoms velocity is decreased from $v_l = 600$ m/s to $v_l = 60$ m/s.

Booster

Overlaid with the ZSL beam, the booster acts as a second ZSL together with the MOT magnetic field. With the booster, the velocity of the atoms exiting theZSÖ can be deliberately chosen higher than the MOT capture velocity. If the exit velocity of the ZSL were equal to the MOT capture velocity, the residual transversal velocity of the atoms would cause a strong divergence of the beam. By choosing the exit velocity higher, this spread of the atoms behind the ZSL can be reduced.

Magneto-optical trap

Finally, the atoms can be trapped in the MOT. Here, the first and second repumper again reduce the effects of off-resonant scattering to other hyper-fine levels. This extends the lifetime of the atoms inside the trap. The fluorescence of atoms can be detected with a camera or, for single atoms, with an avalanche photodiode (APD).

^{40}Ar beam imaging

In the case of ^{40}Ar it is also possible to examine the transverse profile of the atom beam at the end of the vacuum system instead of capturing the atoms in a MOT. This beam imaging is used as a tool for flux optimization, since it can observe space-resolved changes in the meta-stable flux caused by the COL and MOL.
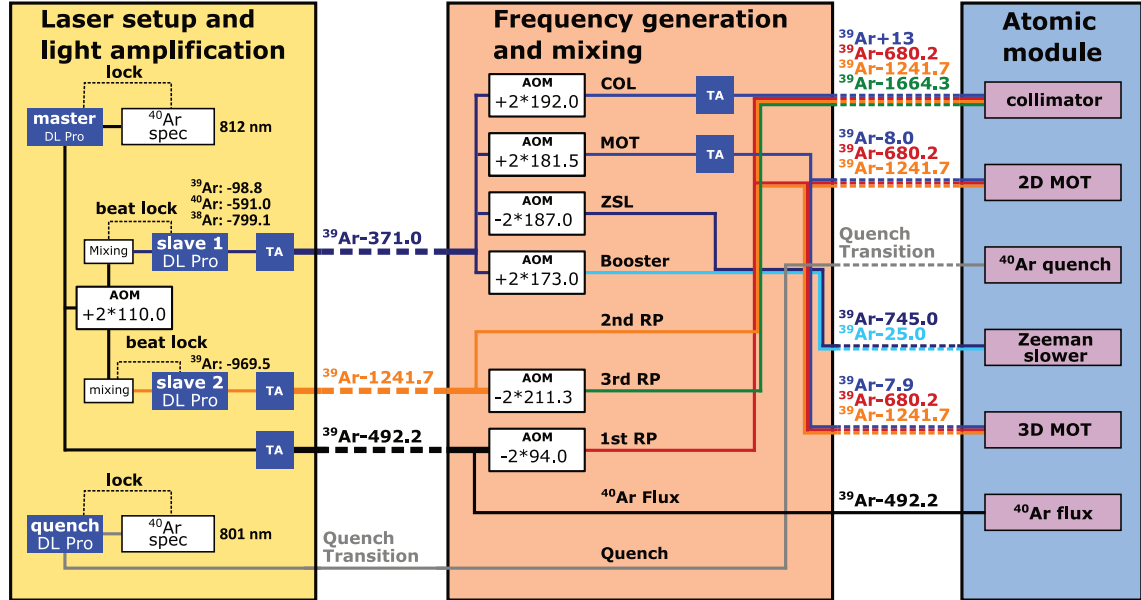
3.2 Laser setup

Figure 3.3: Overview of laser frequencies used in the laboratory container. This figure is based on [52], but has been modified according to the changes made throughout this thesis. It is divided into three parts, where the left one shows the generation of the laser power and the laser locks. For the slave 1 beat lock, the applied frequency difference for each isotope is shown, where slave 2 is only used for ^{39}Ar. In the middle, the frequency generation with acousto-optical modulators (AOMs) is shown. The right section shows which laser frequencies are used in which part of the apparatus.

The laser setup of the container is based on the design for the first ArTTA machine, since the laser frequencies and powers needed are the same. An overview of the used laser frequencies and their purpose in the experiment is shown in figure 3.3. This frequency overview is based on [52], but modifications on this system have been made, which will be discussed in the following.

The laser light of narrow line-width is generated by four external cavity diode lasers (ECDLs) [81, 82], which are *Toptica DL Pros*. These ECDLs are called the master, slave 1, slave 2, and the quench laser. The master and quench laser are both locked to a spectroscopy of meta-stable ^{40}Ar, the master to the cooling transition $4s[3/2]_2 \rightarrow 4p[5/2]_3$ at $812\,\mathrm{nm}$, the quench to the quench transition $4s[3/2]_2 \rightarrow 4p[5/2]_2$ at $801\,\mathrm{nm}$ (see subsection 2.4.2).

The slaves are both locked via an offset lock, for which functionality and setup is discussed in detail in [83] and [84]. For this offset lock, the slave lasers are overlaid with the master laser and directed onto a fast photodiode, creating a beating in power. This beating frequency depends on the frequency difference between the two lasers. One can lock the slave laser to this beating and therefore fix the frequency difference between the master and the slave. Slave 1 is used for generating cooling light in MOT, collimator and Zeeman slower and is therefore also called the cooler. Since the offset lock allows for a variable locking the cooler can also be set to provide the frequencies neceassary for trapping other argon isotopes (see figure 3.3 slave 1 beat lock). Due to the large shift between the cooling frequencies and the repumping sidebands, a second slave laser is necessary which is locked to another frequency difference from the master. This slave 2 is used to generate most of the repumping transitions, and is therefore referred to as the repumper.

This concludes the locking of the lasers, shown in the left part of figure 3.3. The power coming from the *DL Pros* at the argon wavelength of 812 nm is typically, depending on the diode, between 50 and 80 mW for anti-reflection coated diodes or between 100 and 150 mW for Fabry-Perot diodes [85]. The cooler needs to produce 65 mW of Zeeman slower power alone, without even considering the losses obtained by passing AOMs and fibers. Therefore, a laser power amplification is needed.

A widely used tool for laser light amplification is a tapered amplifier (TA) diode. These are semiconductor laser diodes with a tapered gain profile (in this experiment *Eagleyard EYP-TPA-0808-02000-4006-CMT04-0000* are used). They achieve an amplification of a 12 mW laser beam, the seed, up to 2 W of power [86]. In order to amplify incoming light, the coupling of this light into the diode has to be highly optimized and kept stable. Furthermore, the coupling of the high power into an outgoing fiber requires precision and care. These requirements are all fulfilled in the design shown in figure 3.4 a). This schematic shows the setup of a TA laser, which has been extensively discussed in [87] and was designed in this group.

In the container, five of these TA systems are in place, one for each ECDL except for the quench, one for the collimator and one for the MOT cooling light. Since the space on the optical table is very limited due to the small size of the laser room in the container, the TA units have been outsourced into a rack system. This is shown in figure 3.4 b).

Having generated the necessary powers for the ArTTA machine, the needed frequencies follow. A schematic of this is shown in the middle part of figure 3.3. The required frequencies are obtained by shifting the ECDL frequencies with acousto-optical modulators (AOMs, *Gooch & Housego, 3200-124*) [68]. The exact rf-frequencies applied onto each AOM in the experiment are displayed in figure 3.3.

The final step of the laser system is to mix these frequencies for the use at different stages of the experiment. After this, all generated laser beams are brought to their specific operation point in the experiment by optical fibers. This is achieved with seven fibers going from the laser room to the vacuum chamber. These are, sorted
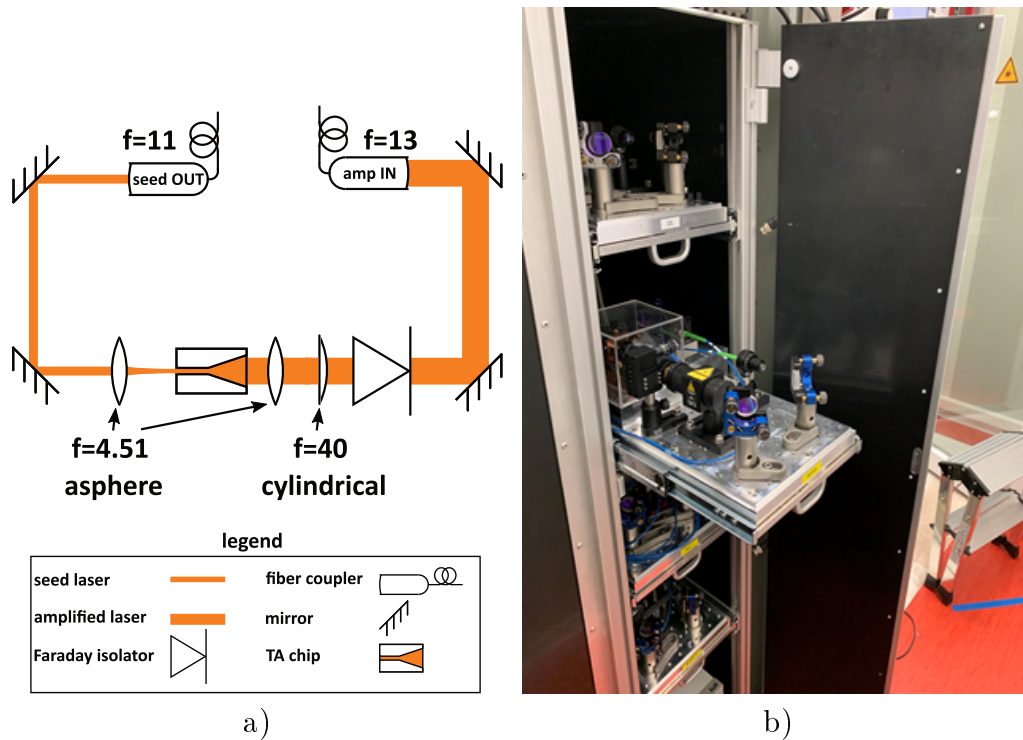
Figure 3.4: a) Sketch of the tapered amplifier (TA) block design. The seed laser is focused onto the input facet of the TA diode with a lens, where its position can be optimized by two mirrors. The amplified output beam is shaped with two lenses and coupled into the input fiber with two mirrors. To protect the diode from back-reflected light, a Faraday isolator is used. This optical path is realized on top of a massive aluminum block which is used for passive temperature stabilization. More detail of this can be found in [87]. b) Picture of the TA rack system in the container. The TA blocks on which all the optical components are fixed is mounted onto a shelf. When operating, the rack is closed off to ensure temperature stability.

by their appearance from the atoms' perspective: the two collimator axes, the two MOL axes, the quench light, the ZSL and the MOT[2]. This is shown in the right section of figure 3.3.

---

[2]The MOT light is later split up into three fibers by a fiber bench 1:3 splitter. The discarded power from polarization cleaning is directed into a Fabry-Perot interferometer which continuously monitors the frequencies and relative powers in the MOT.
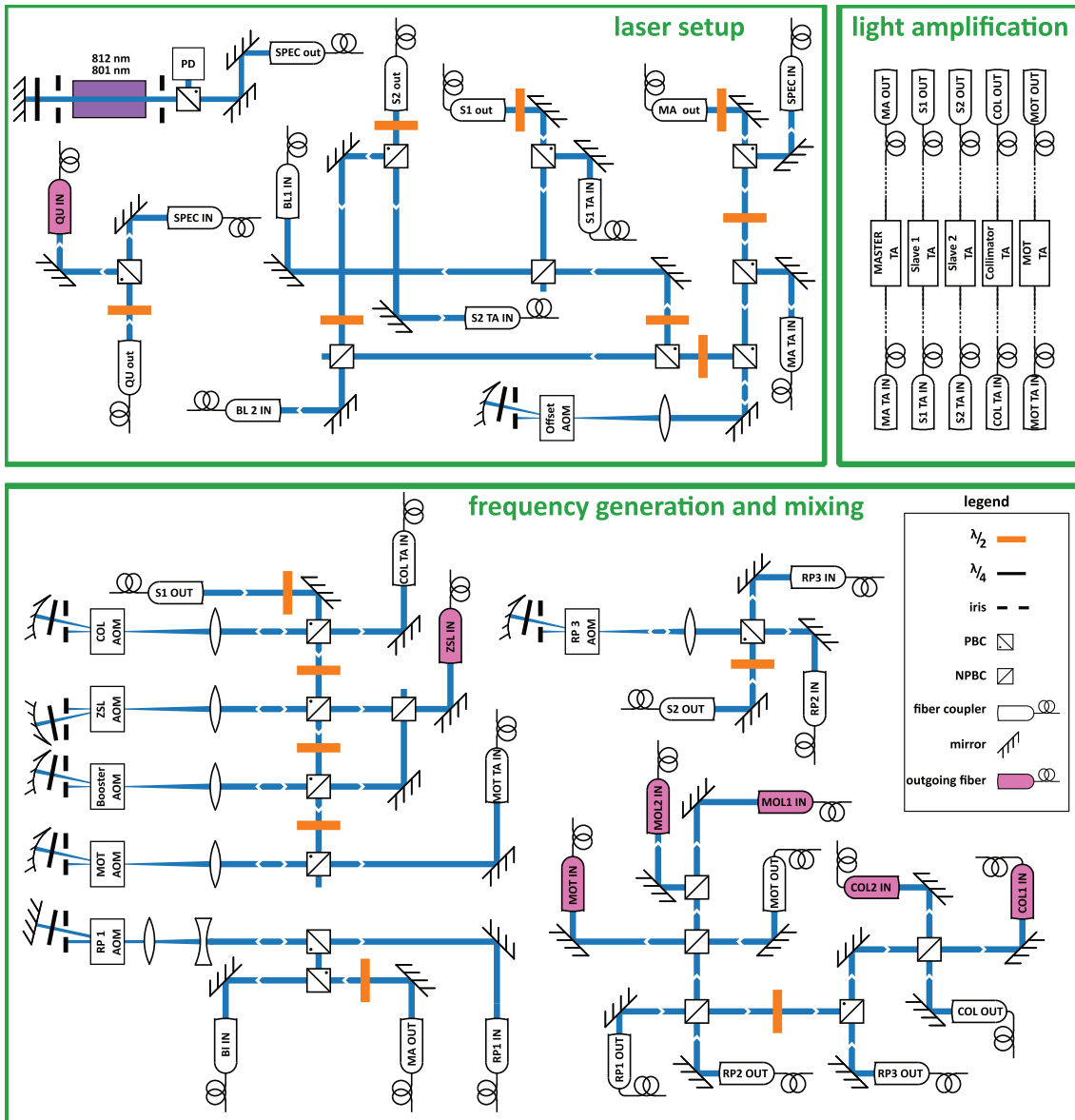
Figure 3.5: Schematic of the complete argon laser setup in the container. Not shown are the four *DL Pros* which generate the laser beams for master, slave 1, slave 2, and quench. The output fibers of these lasers are MA out, S1 out, S2 out and QU out. The lowercase 'out' is used for not yet amplified laser light. The setup is divided into three parts: The first one being the frequency stabilization, where the laser locking takes place. After amplification with self-built TAs, the slave and master lasers are used to generate the needed frequencies with AOMs. Each shifted frequency is then coupled into a fiber and directed to the mixing setup, where the fibers used in the vacuum setup are generated. These seven highlighted fibers leave the optical table and are led to their required position at the vacuum setup.

The whole laser setup with all included optics is shown as a schematic in figure 3.5. The laser system was designed as a modular setup so that occasional optimization of the beam path and replacement of components such as TA diodes will not affect the complete adjustment. The modularity enables comfortable and fast maintenance of the laser system at the cost of power losses due to the use of more optical fibers.

3.3 Performance measurements with meta-stable ^{40}Ar beam

Monitoring and optimizing the performance of the ArTTA machine before each counting of ^{39}Ar atoms is a crucial step to ensure stability and high count rates. The fluorescence measurement of a meta-stable ^{40}Ar beam at the end of the apparatus has proven to be a robust and reliable device in the first ArTTA machine. This so-called beam imaging has been designed and realized in the original ArTTA machine during the thesis of Sven Ebser [35]. Now, a few years later, this beam imaging setup is still used every day to monitor and tune the machine's performance. The design employed in the container was built up as a copy of the original with standard components from *Thorlabs*. It will be briefly reviewed in this section.

Figure 3.6 shows a schematic of the beam imaging setup in the container. The aim is to cut through a beam of meta-stable ^{40}Ar with a 'sheet of light' which is on resonance with these atoms. The fluorescence light of the atoms is guided onto a camera, obtaining a cut-through image of the atom beam.

The sheet of light is a laser beam of rectangular cross section, with very narrow side and the other one in size comparable to the meta-stable beam diameter. On the edges, the power falls off rapidly. This beam shape ensures the excitation of atoms across the whole beam cross section, but at the same time narrowing the area of addressed atoms resulting in a slicing of the beam.

To produce such a beam, an engineered diffuser is used (*Thorlabs ED1-S20-MD*). This diffuser transforms the collimated gaussian beam to a square cross section with rapid power drop at the edges. However, the light emerging from the diffuser is no longer collimated but features an opening angle of 20° for this specific device. With two cylindrical lenses behind the diffuser one can now collimate the beam and shape the rectangular cross section as desired. In the case implemented in the container setup, a beam cross section of 6 mm × 50 mm was chosen, resulting in the use of f = 20 mm and f = 150 mm cylindrical lenses. Figure 3.6a) shows the beam shaping unit. It was built in a two inch cage system and mounted on top of the beam imaging vacuum chamber. Therefore, the laser beam hits the atoms from above. This vacuum chamber is directly behind the MOT chamber, see figure 3.1.

The fluorescence light from the meta-stable ^{40}Ar first hits a mirror and is then directed into the camera (*Allied Vision Guppy F-044*) after passing a focusing lens,
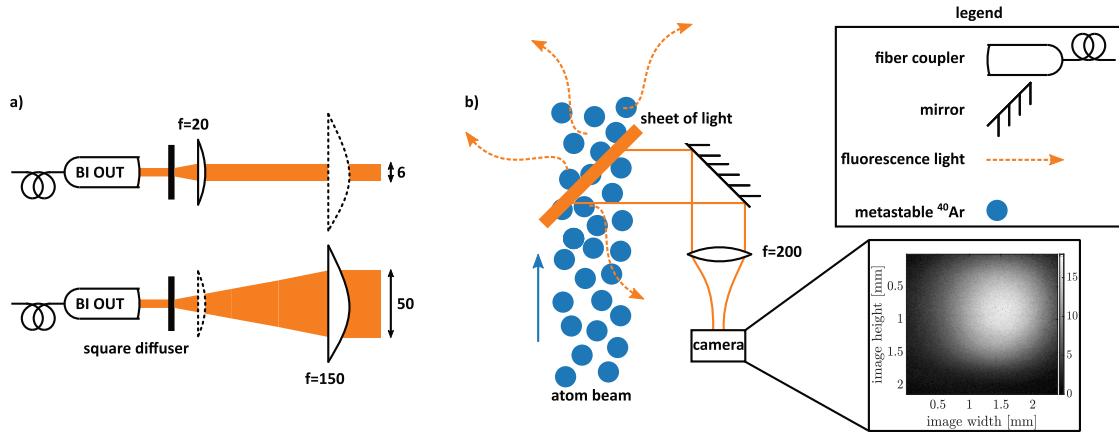
Figure 3.6: Scheme of the beam imaging setup employed in the container. All widths and focal lengths are given in mm. a) Production of the 'sheet of light' with fiber coupler, square diffuser and two cylindrical lenses. The lower beam path is rotated by 90° along the optical axis with respect to the upper one. The final laser beam is of rectangular shape with dimensions $6\,\text{mm} \times 50\,\text{mm}$. b) Position of 'sheet of light' relative to atom beam. The atoms travel from the source to the end of the machine upwards. Arrows represent the random photon scattering from spontaneous decay. Some of these fluorescence atoms reach the mirror and are then reflected and focused onto the beam imaging camera. The inset shows a typical beam imaging signal of a ^{40}Ar beam. The image was taken with a *Guppy F-044* camera and shows the atom beam without any flux enhancing tools like collimator and MOL. Adding the collimator typically increases the overall fluorescence by a factor of 100.

as is illustrated in figure 3.6b). The shown mirror is crucial to position the fluorescence on the camera. A typical image taken with the setup is displayed as an inset in figure 3.6. In order to optimize the beam shaping performance of the ArTTA machine, one takes images similar to the inset and subsequently adds the COL axes and MOL. The obtained enhancement in fluorescence for each step is noted and gives a measure for machine stability and performance.

3.4 Source performance monitoring with quench transition in ^{40}Ar

The production of meta-stable argon in the plasma source still remains one of the major concerns for the ArTTA machine. The production efficiency of the cooling ground state is only $\sim 1.5 \times 10^{-3}$ [51], meaning only one in 700 atoms ends up in the desired state $4s[3/2]_2$. Also the plasma is sensitive towards changes in source pressure, rf-frequency and power and impedance matching between antenna and rf-amplifier. To monitor the plasma efficiency at all times, even during ^{39}Ar counting, selective de-excitation of meta-stable ^{40}Ar is conducted while gathering fluorescence photons.

The transition driven for the de-excitation was introduced in subsection 2.4.2 and is referred to as the quench transition. After the atom is excited from the meta-stable state $4s[3/2]_2$ to $4p[5/2]_2$ by the quench laser it can decay to the $4s[3/2]_1$ state by emission of a 843 nm photon. From this state, the atom can decay to the absolute ground state via a strong dipole transition. Detecting the amount of 843 nm photons directly returns the number of ^{40}Ar atoms initially in the meta-stable state, which in turn is an absolute measure for the performance of the plasma source.

This de-excitation and photon collection is also implemented in the first ArTTA machine and is there used for continuous source efficiency monitoring [19]. The compactness of the container vacuum system allows for an optimization of the objective towards higher numerical aperture. Therefore its realization differs from the one designed in the first ArTTA and is discussed in the following.
Figure 3.7 shows the implemented objective design and how it is built into the vacuum chamber. The main function of the objective is to collect as much fluorescence light as possible, while staying in the spatial restrictions provided by the vacuum chamber and its flanges. The vacuum part, wherein the setup is built, is a six-way cross. The quench laser proceeds into the paper plane, the objective for photon collection is is shown on the side. In order to accumulate as much light as possible, the numerical aperture (NA) of the objective needs to be large. In general,

$$NA = n \sin(\theta) \tag{3.1}$$

with the refractive index n. In this case of a random distribution of scattering light into all spatial directions (i. e. spontaneous emission [47]) a larger solid angle θ results in more collected light. For this setup $NA = 0.66$ is realized by putting two lenses of small focal length as close to the atoms as possible. First, these two lenses collimate the fluorescence light, in order to reduce aberrations caused by passing the vacuum window. Afterwards, the same set of lenses focuses the light onto a camera, which is shielded from stray quench light with a band-pass filter (*Thorlabs FB840-10*).
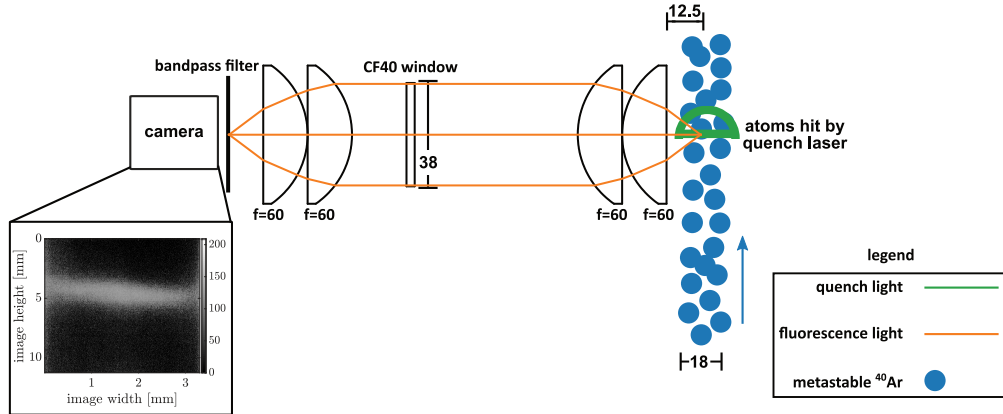
Figure 3.7: Setup of fluorescent light collector for source monitoring with the quench transition. The atoms travel from bottom to top, the quench laser beam passes perpendicular to the beam into the paper plane. The used lenses and the filter are built into a 2 inch lens tube from *Thorlabs*. The inset shows a typical image of fluorescence caused by de-excitation with quench light. The laser beam passes through the meta-stable ^{40}Ar beam. For density monitoring, the image is summed up, as a change in meta-stable atoms does not result in a variation of shape but only signal intensity.

A typical picture from the camera (in this case *Allied Vision Mako G-223B NIR* which was replaced by *Allied Vision Mako G-223B NIR* with a better quantum efficiency) is depicted in the inset of 3.7. The passing of the quench laser through the atom beam can be nicely observed since the fluorescence along the beam cross section appears as a white stripe. For monitoring purposes, this image is integrated.

A change in meta-stable density directly leads to a variation in measured fluorescence. During an ^{39}Ar atom counting the flux is continuously monitored. This can be seen for a measurement of enriched ^{39}Ar in figure 3.8. The upper part shows the detected quench flux measured with the setup in figure 3.7. If the meta-stable density stays constant over the complete measurement time, one would observe only a straight horizontal line as the quench flux. The upper graph in figure 3.8 displays this line with two distinct kinks at $\sim 0.55\,h$ and $\sim 0.66\,h$ and shows a sudden decrease of meta-stable density. At these points, the plasma source jumped into another mode.

The lower part of figure 3.8 shows the corresponding number of accumulated counted ^{39}Ar atoms in the same measurement. At the temporal positions of the mode-hops in flux, the atom number also experiences a jump. In the regime between
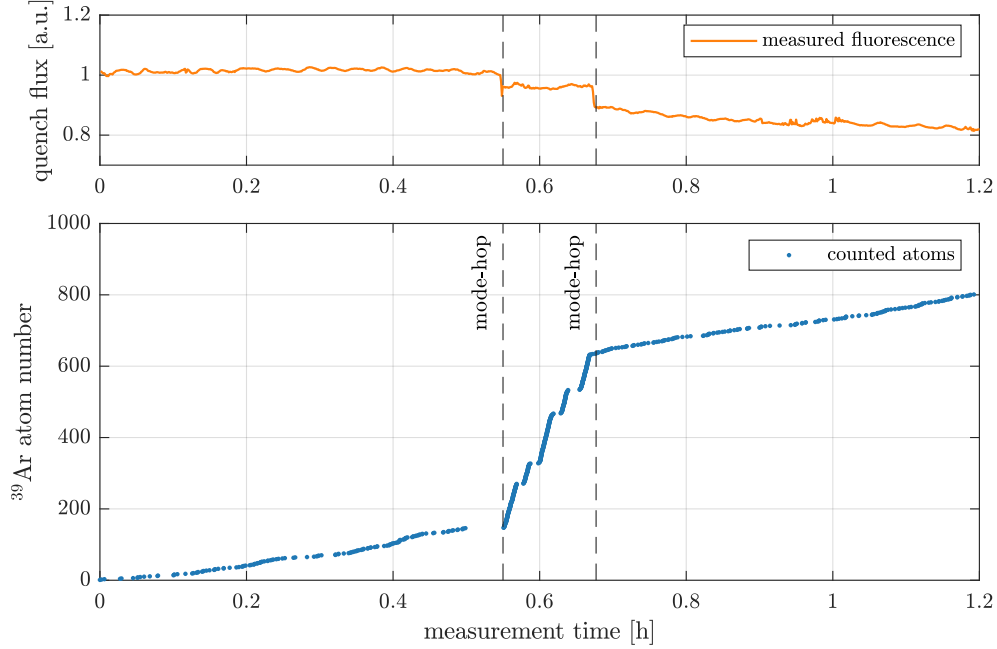
Figure 3.8: Top: Monitoring of quench flux over the course of a ^{39}Ar measurement. The fluorescence of the quenched ^{40}Ar atoms was detected with the setup shown in figure 3.7. Two kinks in flux are visible at ~ 0.55 h and ~ 0.66 h which show a sudden decrease of meta-stable density. These are caused by plasma source mode jumps. Bottom: Corresponding number of accumulated counted ^{39}Ar atoms in the same measurement. The atom number experiences jumps at the same position as the upper displayed flux. Surprisingly, the meta-stable density decreases between ~ 0.55 h and ~ 0.66 h whereas the atom number rises more strongly. This is an artifact of the measurement, obtained with a setup containing a highly ^{39}Ar contaminated vacuuum part directly behind the source. Variation of the plasma might lead to a stronger contamination which cause a higher count rate.

the two mode-hops the accumulated atom number rises much faster than for the other two source modes. Surprisingly, the meta-stable density decreases and still the atom number rises more strongly, although a low amount of meta-stable ^{40}Ar atoms should directly correspond to a smaller ^{39}Ar count rate.

This rise in count rate for the intermediate regime is an artifact of the measurement. This data was obtained with a setup containing a highly ^{39}Ar contaminated vacuuum part directly behind the source. Variation of rf-power, frequency or

impedance matching has effects on the plasma's position inside the ceramic tube. Having the plasma burn more towards the contaminated part, which was at the connection between fore-vacuum and source chamber, would release more of the highly ^{39}Ar enriched argon. Therefore it is possible to decrease the meta-stable density, by actually reducing the source efficiency, while obtaining more ^{39}Ar due to the plasma's position. Note that the contaminated part was removed from the setup as soon as it was identified to be responsible for the high amount of ^{39}Ar. However, this measurement is still shown since it very nicely shows the connection between source efficiency and flux measurement.

3.5 Single atom detection

This section shows the way towards single atom detection in the ArTTA container. It includes the design of the MOT objective and the tool for fluorescence detection. It concludes with an image of the first single ^{39}Ar atoms inside the container.

In [52] capture and detection of the abundant isotopes ^{40}Ar and ^{84}Kr inside a MOT was demonstrated. This was achieved with a camera (*Allied Vision Guppy PRO F-031*) and a basic objective suitable for observing large atom clouds. This combination was the perfect tool to demonstrate the first magneto-optical trapping in the container. However, the setup for detecting single atoms had yet to be designed. This thesis will pick up from that point, designing a more fitting objective for single atom detection and introducing a new detection device into the container.

3.5.1 Construction of the detection setup

A camera is ideal for a robust monitoring of high fluorescence signals, but single atoms require a different solution. Typically, the mean atom lifetime in the ArTTA trap is $\sim 300\,\mathrm{ms}$, which means that many atoms stay captured for a much shorter duration. In order to detect also these short-living atoms, a very fast, yet very sensitive photo-diode is used for fluorescence detection. This avalanche photodiode (APD) detects single photons in ns range. Compared to this, a camera would require a longer integration time for the small signal intensity and therefore might not detect some short-lived atoms.

The fluorescence light of the atoms in the trap needs to be directed onto the APD. Since the signal caused by a single atom is very small, as much light as possible needs to be collected. This collection is achieved with the objective. As the APD is very sensitive, placing it directly behind the objective might cause for the collection of much stray light, so the APD is placed 1 m from the MOT itself, shielded from the lasers. The objective then focuses the signal light onto a multi-mode fiber which in turn is connected to the APD. The whole setup of APD, fiber, objective and MOT needs to be matched in image cross section and numerical aperture to ensure

the highest photon yield. All these components put together result in the desired **detection setup**.

Since the MOT is optimized for atom capture, one needs to design the other parts
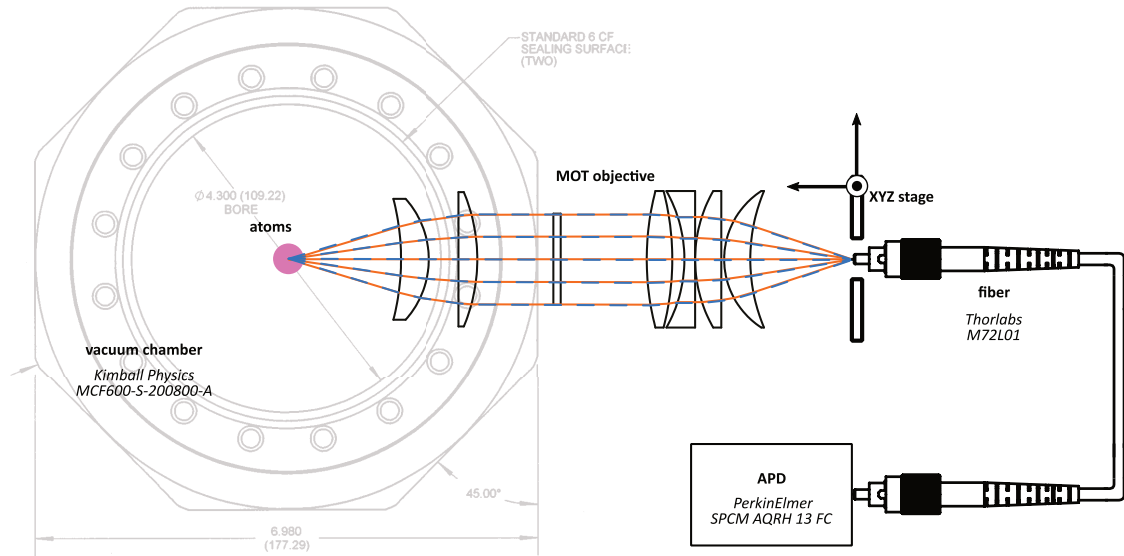

Figure 3.9: Sketch of the single atom detection setup. The atom is centered inside the shown vacuum chamber and depicted by the pink sphere. The objective will be shown more extensively in figure 3.10. The light of the atoms is focused with the objective onto the multimode fiber *Thorlabs M72L01* which is mounted on a xyz stage. The other end of the fiber is connected to the APD which is a single photon counting module *SPCM AQRH 13 FC* from *PerkinElmer*.

of the detection setup around this atom trap. The restrictions given by the MOT are the position and size of the objective inside the vacuum chamber set by the atom cloud size and laser beam cross section. The trap size is given by the force acting on the atoms in it, whereas a large force results in a small trap size. With [51] and [52] the MOT size in the container for a gradient of $20\,\mathrm{G/cm}$ and $10\,\mathrm{G/cm}$ in axial and radial direction, respectively, can be calculated to $110\,\mu\mathrm{m}$ and $77\,\mu\mathrm{m}$ in horizontal and vertical direction. These two values are due to the different magnetic field gradients caused by the anti-Helmholtz coil design. This results in a varying force for horizontal and vertical direction.

Another fixed constraint on the design is the placing of the objective. In order to maximize the photon yield, the objective needs to be placed as close to the atoms as

possible. This increases the NA and therefore the observed solid angle of the MOT. The vacuum chamber is a spherical octagon from *KIMBALL PHYSICS* with eight CF40 windows on the side and two CF63 windows on top and bottom(*MCF600-SO200800-A*). As the imaging will be done from the side, the lenses inside the vacuum chamber may not be wider than the CF40 window. This limits the diameter of the lenses to 34 mm. The MOT beams are ~ 12 cm in diameter. With the geometry of the vacuum chamber, the laser beam width and the lens diameter, the distance between MOT and the first lens needs to be $\lesssim 48$ mm. This also directly restricts the image NA to $\lesssim 0.32$.

Knowing the image size and numerical aperture one can now go on to choose a fitting fiber and APD module. The single photon counting module used is the *SPCM AQRH 13 FC* from *PerkinElmer*. It features a detector size of 175 μm in diameter and a detection efficiency of 55 %. Although the possible detection rate is ~ 100 GHz, the counts are averaged over 1 ms to reduce the data flux to the PC while still enabling detection of shortly captured atoms. The size of 175 μm is chosen to match the fiber cross section.

The fiber is chosen to match the MOT size and NA. The *M72L01* from *Thorlabs* is a good fit with a cross section of 200 μm and a numerical aperture of $NA = 0.39$. The APD fiber is put behind the objective onto a XYZ-stage to enable optimization of its position.

In order to reduce stray light reaching the fiber, 48 mm long tubes, painted black, were put into the vacuum chamber behind each horizontal MOT beam window. This reduced the APD background by a factor of 3.5.

3.5.2 Design of a new MOT objective

All that is left now is the design of the MOT objective, which is also the most complex part. As the object size and also the image size are very small, it is crucial to reduce the contributions of spherical aberrations, which might enlarge the image and cause signal loss. This is achieved by using multiple lenses and carefully placing them while minimizing aberration effects. This optimization of the lenses in terms of focal length and position was carried out with the lens designing software *OSLO*.

Fortunately, the MOT chamber in the container is exactly the same as for the other ArTTA lab, therefore the design of the objective could be based on the already employed design of [51]. For the lenses inside the vacuum still available replacement lenses of the original objective were used, which are custom made lenses from *MellesGriot* ground to a diameter of 34 mm. These are screwed into a lens tube, which in turn is fixed on the vacuum chamber wall by grub screws. This part of the objective in combination with a single lens outside the vacuum, focusing the light on the camera, was already used to demonstrate the detection of atom clouds in [52].

However, for the new outer part of the objective, an exact copy of [51] was not possible, since none of the lenses used were longer available. Therefore, the objective as a whole was redesigned. Since the inner part of the objective was already built in, only the lenses outside the vacuum were changed and replaced by lenses from the *Thorlabs* catalog. The result is presented in figure 3.10 .

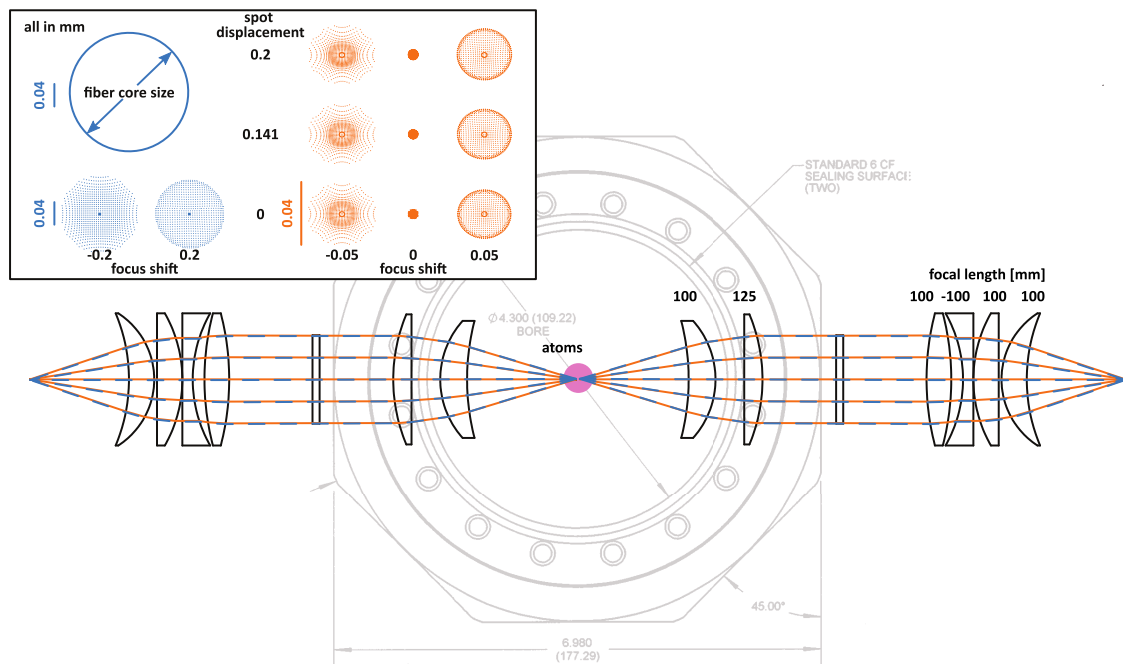All used lenses of this new objective and also the objective previously designed

Figure 3.10: Sketch of the objectives built into the MOT vacuum chamber. The atoms are centered inside the chamber. The two objectives shown from the left and right side of the atoms are identical, whereas one of them directs light onto a multimode fiber connected to the APD, the other one onto the camera. As the APD is the tool used for single atom counting, the objective was designed to optimally map the fluorescent light of the MOT onto the fiber. In order to check this, the fiber size compared to the MOT size at different positions is shown in the inset. The scale changes between the blue and orange dots, to better compare them. The exact lenses used are documented in the appendix A.

in [51] are listed in the appendix A.1. The shown objective features a numerical aperture of $NA = 0.317$ which is limited by the geometrical restrictions of the vacuum chamber. Figure 3.10 shows this objective twice, once for the camera and once for the APD. Each objective features two lenses inside the vacuum and four

outside. The rectangle between these is the vacuum chamber window, which also acts as an iris, limiting the diameter of the collimated light.

The inset of figure 3.10 shows the in *OSLO* calculated spot size of the MOT fluorescence for certain displacements of its position. The two colors respresent different length scales, whereas the orange spots are ~ 3 times smaller than the blue ones. Still, the core size of the fiber is with its $200\,\mu$m bigger than any spot size shown. These spot sizes were chosen to resemble the natural size of the MOT, which is, as discussed before $< 120\,\mu$m. The two largest spot sizes for a displacement of $200\,\mu$m are still smaller than the fiber core cross section. Therefore, the objective is suitable for imaging the fluorescence of a MOT onto the fiber.

3.5.3 Counting of single ^{39}Ar atoms

The combination of a new objective and the single photon counting module now permits the detection of single atoms in the container. The first signal was produced with the stable isotope ^{38}Ar, because its high abundance enables optimization of the APD position. After the single atom signal was maximized on the APD, the first detection of the rare radio-isotope ^{39}Ar was accomplished.

The left side of figure 3.11 shows the signal of a single ^{39}Ar atom captured in the container MOT. In both the raw and the smoothed (binomial filter 75 ms [66]) signal, the increase in fluorescence is clearly visible. The chosen ^{39}Ar atom stays captured for two seconds, however, the mean atom lifetime in the trap for this measurement was $\sim 500\,$ms. On the right side of figure 3.11 the signal of two captured atoms can be observed. Here, the second atom lives only for $\sim 300\,$ms. With the single atom detection technique available in the container, all that is missing for radio-argon dating of samples is the enhancement of atom flux into the MOT.
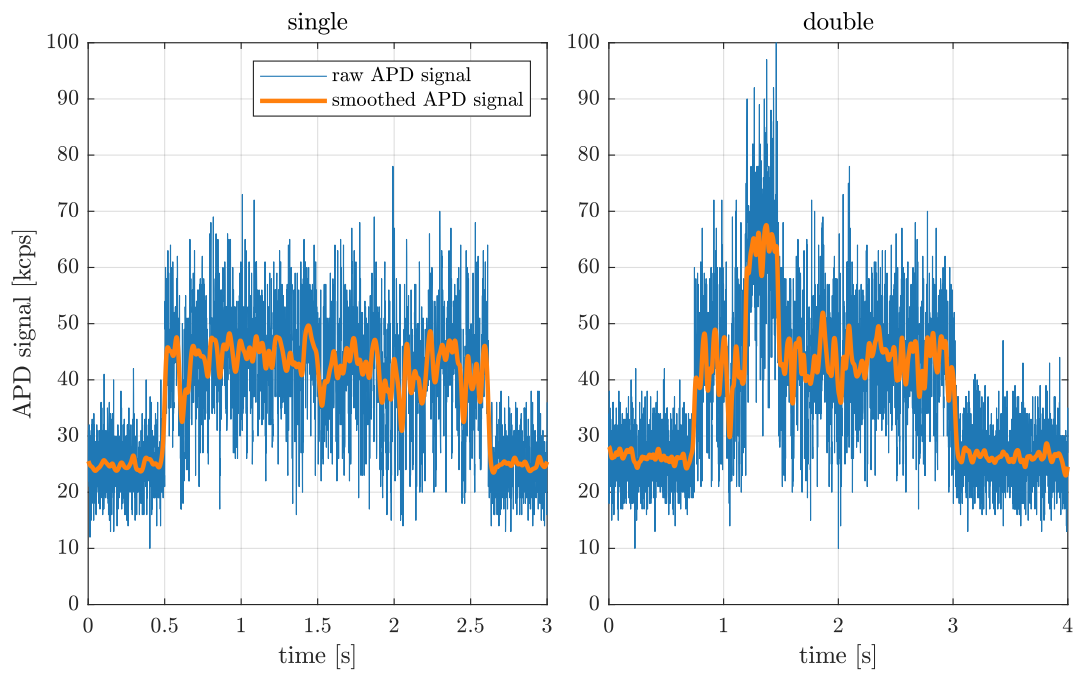
Figure 3.11: Signal of a single ^{39}Ar atom (left) and two atoms (right) inside the MOT. The blue line is the raw signal of the APD, whereas the orange line is the smoothed version.

4 Setup and demonstration of a dual ATTA system for ^{39}Ar and ^{85}Kr

This thesis demonstrates the combination of ^{39}Ar and ^{85}Kr detection in one ATTA apparatus, yielding a dual ATTA experiment (D-ATTA). This is achieved by the setup of a krypton ATTA (KrypTTA) inside the original ArTTA argon dating machine. This chapter presents the design and finalization of the krypton laser system, the integration of the generated laser frequencies into the ArTTA vacuum setup, setting up detection and monitoring of abundant krypton isotopes and modifications of the vacuum system to account for the small krypton samples. All these elements put together transformed the ArTTA system into a KrypTTA machine, where the combination of both results in the desired D-ATTA. The chapter will conclude with a first demonstration of a D-ATTA measurement.

4.1 Overview of the KrypTTA apparatus

Similar to figure 3.1 shown in the previous chapter for the ArTTA apparatus in the container, figure 4.1 shows a schematic of the KrypTTA machine realized inside the original ArTTA system. The most striking difference is the lack of a quench laser and the meta-stable beam imaging tool. Therefore, two of the vacuum chambers are left blank as they fulfill no purpose for krypton other than differential pumping. The amount of repumpers for krypton is reduced to two, but those are applied in the MOT and MOL as well as in the collimator. The improvements on the fore-vacuum, where the sample is prepared and recycled are discussed in more detail in section 4.4.

4.2 Design and setup of the laser system

The krypton laser system is the combination of the laser table generating the needed powers and frequencies and their integration into the ArTTA system.

4.2.1 Krypton laser table setup

The laser table was first designed during the bachelor thesis of Jeremias Gutekunst [54] and underwent many alterations since then, which will be presented in the fol-
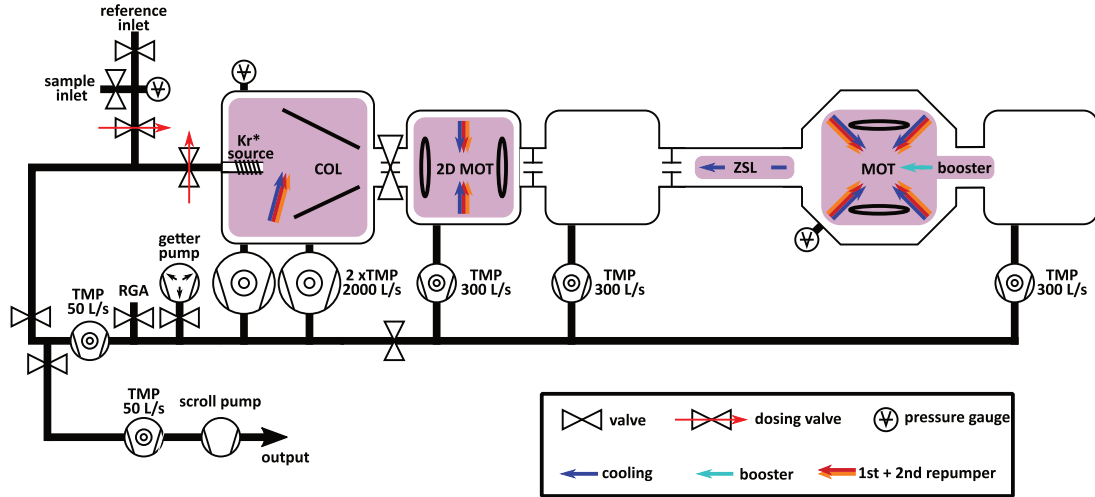
Figure 4.1: Schematic of the KrypTTA apparatus. Since this is a slightly modified version of the first ArTTA apparatus, all main vacuum parts, pumps and magnetic field coils are the same. The machine differs from the ArTTA in applied laser frequencies and slightly in fore-vacuum design, which is further discussed in section 4.4. The blank vacuum chambers are the quench and beam imaging chamber for argon, which have no use in the krypton setup yet.

lowing. Based on the transition spectrum of krypton and the requirements for single atom detection well known from ^{39}Ar, the laser powers and frequencies necessary for cooling and trapping of ^{83}Kr and ^{85}Kr were computed. As mentioned before, the objective was to first only detect these two isotopes since they are most useful together with ^{39}Ar. However, the laser system can, with only minor adjustments, also be used to cool and capture the long-lived radioisotope ^{81}Kr which will be discussed in the outlook 7.1.

The schematic for producing these laser frequencies is shown in figure 4.2 which structure is based on figure 3.3. The master (*Toptica DL Pro*) laser is locked using Doppler-free saturation spectroscopy [47] onto the cooling transition in ^{84}Kr and therefore sets the frequency reference. Its light is then split into two beams, where one is amplified with a TA diode and the other is mixed with the light of another laser, the ZSL laser, to create a beating on which the slower laser can be variably locked with an offset lock [83].
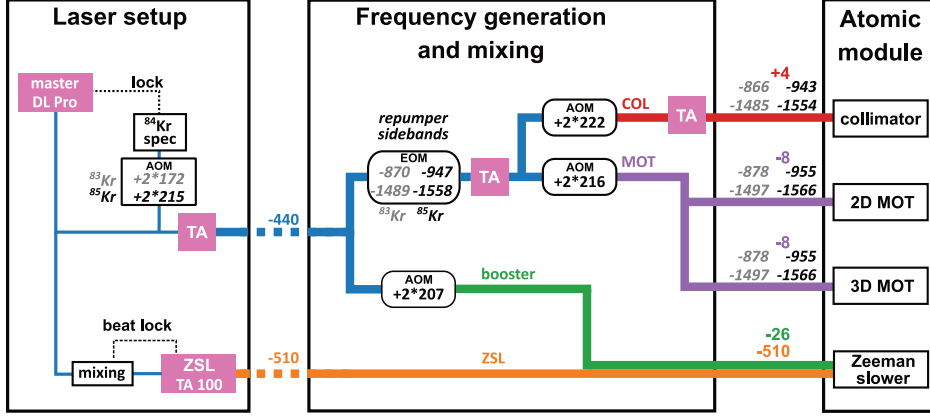
Figure 4.2: Schematic of the laser frequencies generated with the krypton laser system. Numbers in gray, italic font are specific for ^{83}Kr, black italic specific for the radio-isotope ^{85}Kr. Other numbers are not isotope specific. The left part shows the used lasers and their locking. The middle part shows the frequency shifting by AOMs and repumper sideband generation with an EOM. On the right, the use of these laser beams for the atomic module is displayed. This setup shows the realization used in this thesis with an additional laser for the Zeeman slower to ensure detuning flexibility for optimizing the ^{85}Kr flux into the trap. For the complete setup design for future KrypTTA machines, please refer to figure 7.1 in the outlook.

Note that this second laser is a non-necessary addition to the setup for detection of krypton isotopes. However, its flexibility in locking was essential for the optimization of the Zeeman slower detuning for the first measurements with krypton. All experimental data presented in this thesis was produced with this setup. Future krypton laser setups can benefit from the findings of this thesis and directly set the ZSL detuning to the optimum at -510 MHz. Then, the second laser is obsolete and can be replaced by an AOM for the master laser (see section 7.1 in the outlook).

The master laser is locked -440 MHz from the cooling transition in the isotope of interest. This initial frequency difference was chosen because it can be used to produce all required laser frequencies without the use of an additional laser or an offset lock. With the use of AOMs (*Gooch & Housego, 3200-124*) all necessary frequencies can be reached. The Zeeman slower typically needs a large red-detuning.[1] Using a single pass AOM inducing a -70 MHz shift results in a detuning of -510 MHz for the Zeeman slower light. A sketch for this setup is shown in the outlook in figure 7.1.

---

[1] In the realization implemented here, the Zeeman slower is an increasing field slower which requires far red-detuned cooling light $\sim 500 - 800$ MHz.
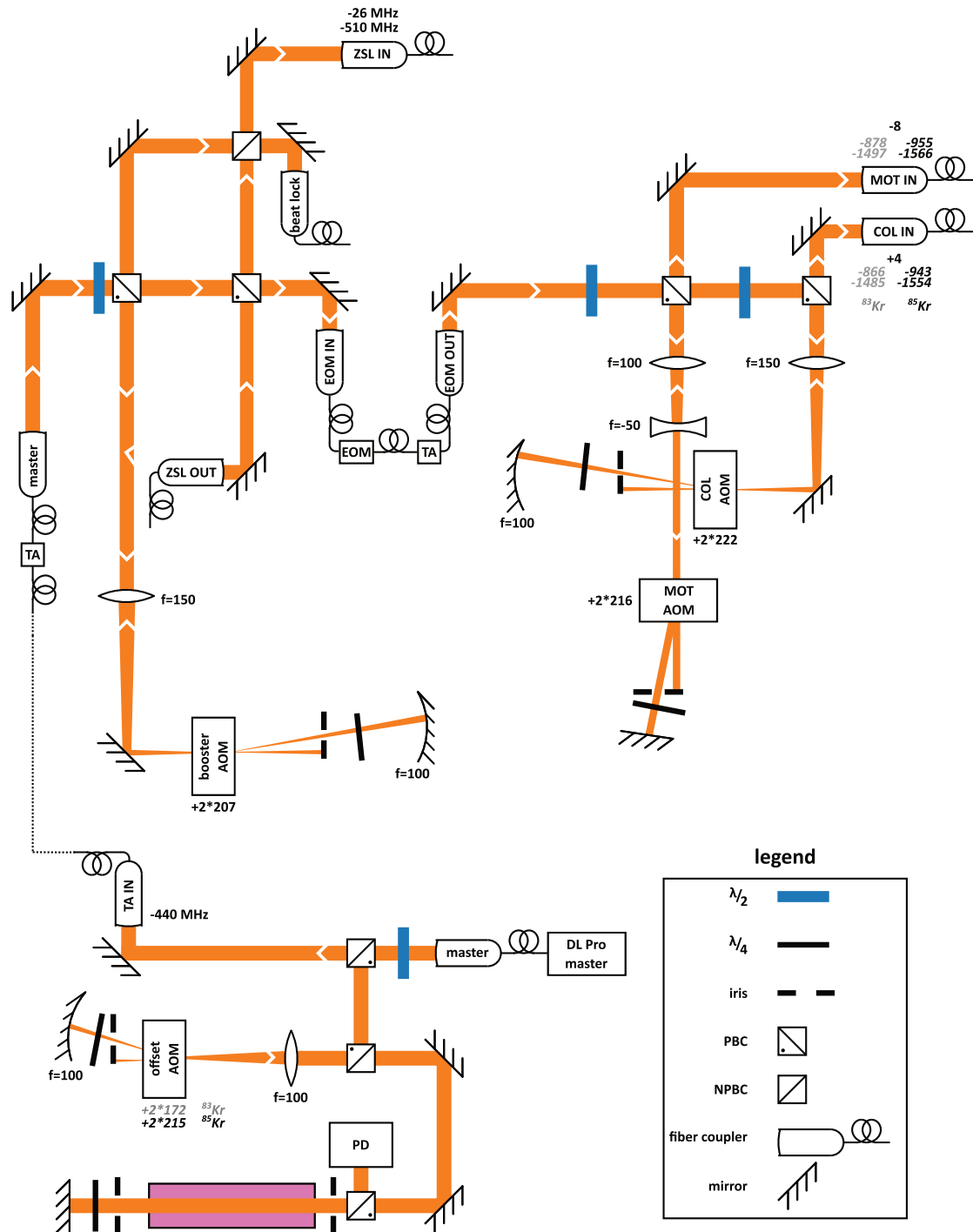
Figure 4.3: Laser setup for capturing ^{83}Kr and ^{85}Kr. This figure shows the realization of the setup designed in 4.2. Not shown is the TA laser for the COL beam. Frequencies written in gray are specific for ^{83}Kr, and in black for ^{85}Kr. Other numbers are not isotope specific.

In order to achieve the $-440\,\mathrm{MHz}$ detuning of the master laser relative to the cooling transition in the isotope of interest, ^{83}Kr or ^{85}Kr, the master's frequency is shifted in a double-pass AOM before entering the spectroscopy cell. The frequency of this AOM for capturing ^{83}Kr is $+2 \times 172\,\mathrm{MHz}$, for ^{85}Kr it is $+2 \times 215\,\mathrm{MHz}$. This offset AOM enables a completely variable frequency shift before locking the laser generating flexibility in the setup without requiring an offset lock technique and a second laser.

After being amplified, the master is split into two beams. One of them generates the booster frequency, the other one is coupled into an EOM to produce the repumping sidebands. The output of the EOM is amplified again to then be split up into two AOM paths, generating the COL and MOT frequency, respectively.

Finally, the collimator and MOT light are coupled into two separate fibers, the ZSL and Booster are overlapped into one fiber. These are then to be integrated into the vacuum system. A schematic of the complete krypton laser table is shown in figure 4.3.

4.2.2 Integration of the krypton setup into the argon system

Since the apparatus is already running for ^{39}Ar, the fibers connecting the argon laser table with the ArTTA vacuum are utilized to get the krypton lasers to the required positions. To enable a fast switching between argon and krypton for the D-ATTA apparatus, the krypton laser frequencies are coupled into the machine-connected fibers via flip mirrors. Extreme care was taken to not loose the coupling of the argon lasers but still unlock the necessary degrees of freedom to couple the krypton lasers into the fibers. The realization of this D-ATTA laser setup on the original argon laser table is shown in figure 4.4.

4.2.3 Sideband Generation with an EOM

The laser system needs to feature repumping sidebands because of the hyperfine structure of both desired krypton isotopes. These are needed in the MOT due to the high number of scattering events and possible loss channels to other hyperfine states. They are also needed in the collimator, directly behind the source, since the meta-stable atoms generated there are distributed over all possible hyperfine states. The repumper laser frequencies are especially important there to pump the atoms into the desired ground state $F = 13/2$.

For the generation of the sidebands a fiber-coupled EOM (*EO Space PM-0S5-05-PFA-PFA-811*) is used. However, the photo-refractive effect limits the laser power that can be put into the EOM [69, 88]. Heating it can typically shift this power limit to higher values, although carefully, in order to prevent melting the glue fixating the
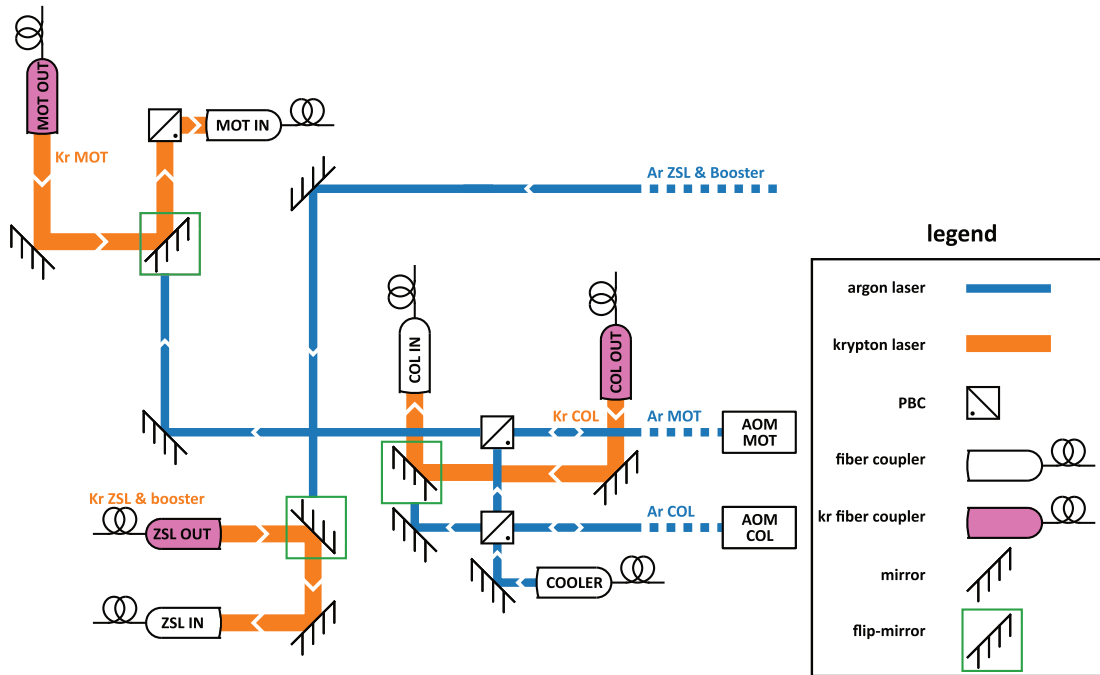
Figure 4.4: Coupling of the krypton lasers into the ArTTA atomic module fibers by use of flip mirrors. The objective was to avoid altering the argon laser coupling to enable fast switching between argon and krypton detection for a D-ATTA machine.

fiber connectors [89]. At a temperature of 48° C a power of 50 mW at the output of the EOM could be achieved, with an input of 100 mW.

Still, this power is not sufficient to create three MOT beams and two collimator beams. Therefore, the use of a further power amplification stage is inevitable.

The amplification of sidebands inside a TA diode has already been successfully shown in [90], but a thorough investigation of the amplified frequencies in this experiment is still required, since high amplification can result in the production of additional sidebands [91].

Figure 4.5 shows the TA power with increasing current. The output power was measured after coupling the laser light into a fiber. This measurement involves some problems: Even a perfectly coupled fiber might decrease its output power with increasing TA current. This is because a change in current influences the laser beam mode, an effect which is typically counteracted by optimizing the lens position in front of the coupling fiber. In the measurement shown in figure 4.5 the lens position was not changed. However, it was still decided to measure the power behind the fiber to neglect the power of the amplified spontaneous emission (ASE) which increases
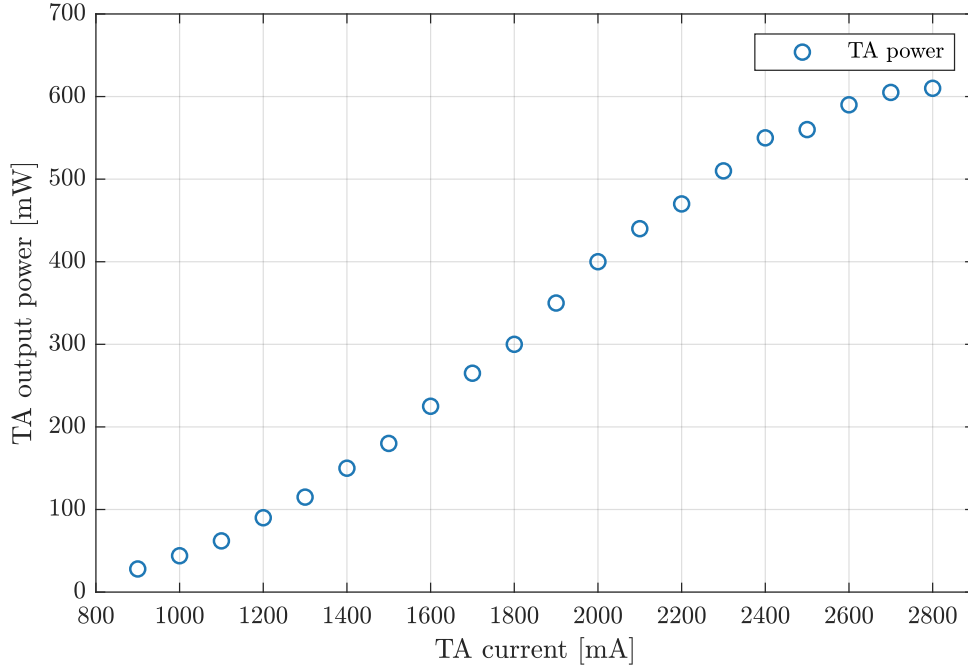
Figure 4.5: Power output of the TA laser diode into a fiber versus TA diode current. A linear amplification regime is observed between 1400 mA and 2400 mA, at higher currents the power saturates. This could be caused by the measurement of power behind the fiber, which reduces coupling efficiency with increasing diode current, or the typical amplification curve of the TA diode.

with current. The fiber acts as a mode filter, which will only let the amplified mode of the seed laser pass.

In the regime of 1400 to 2400 mA a linear increase of the laser power can be observed. At higher diode currents the amplification becomes non-linear. This can cause the appearance of additional side-bands, which in turn can disturb the atom. Still, the TA needs to produce a high output power to produce the necessary power for MOT and collimator.

In order to find the highest possible current at which the TA produces only the desired repumper sidebands without altering their realtive power relation, its output was monitored with a scanning Fabry-Perot interferometer (FPI, *Thorlabs SA 200-5B*) while increasing the TA current.

Figure 4.6 shows two typical scans of this FPI. The carrier frequency is the high peak, while on the left and right are the positive and negative sidebands, respectively. For each TA current a scan similar to 4.6 was taken and the power of each sideband
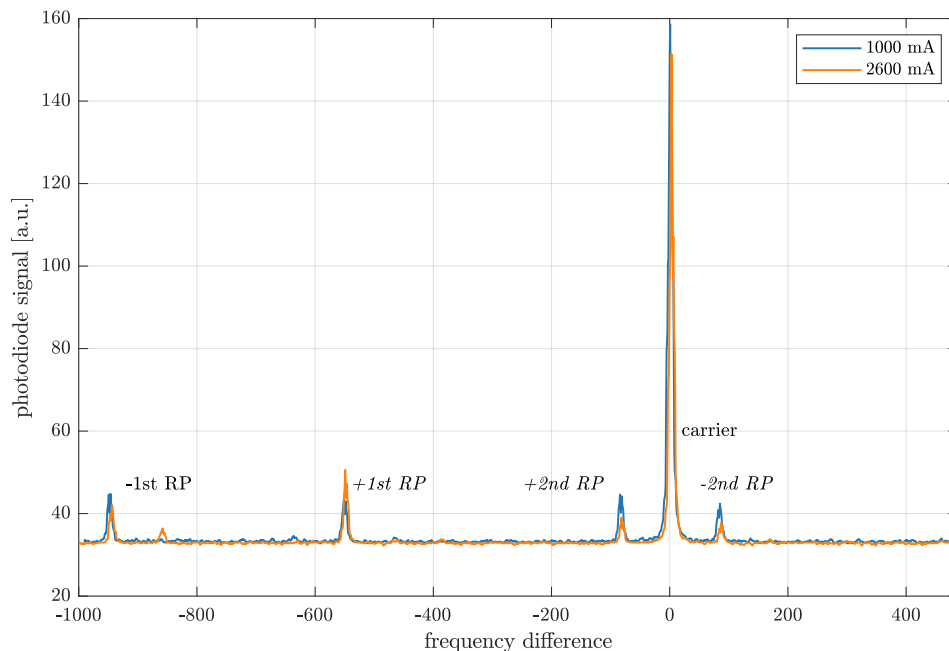
Figure 4.6: EOM side-bands for cooling and trapping of ^{85}Kr. The scans were taken with a FPI and display the complete free spectral range (FSR) of the FPI, which is 1.5 GHz wide. As the repumper spectrum itself is wider than the FSR the peaks cannot be displayed at the exact frequency position. The figure shows only the '-1st RP' peak at the correct distance from the carrier. The other peaks, marked by italic writing, belong to other positions but are displaced due to the limited FSR. However, the exact frequency difference is not of interest here, mainly the side-band peak height for the two different TA currents. The peaks do not vary strongly in height or position for the different currents.

relative to the carrier was determined. The results of this can be seen in figure 4.7. For the left side of figure 4.7 the height of the side-bands was deliberately chosen higher than necessary for cooling, to ensure good visibility of possible fluctuations. The relative power of the sidebands is not visibly affected by the increasing TA current. On the right side, the scenario for the cooling setup is shown. This verifies the stability of the amplification with a tapered amplifier up to 2600 mA, which is the current needed to provide the necessary power for MOT and collimator behind the EOM.

Figure 4.6 already shows the FPI scan at 2600 mA compared to 1000 mA and also the stability of the sidebands. It is important to note that this stable amplification
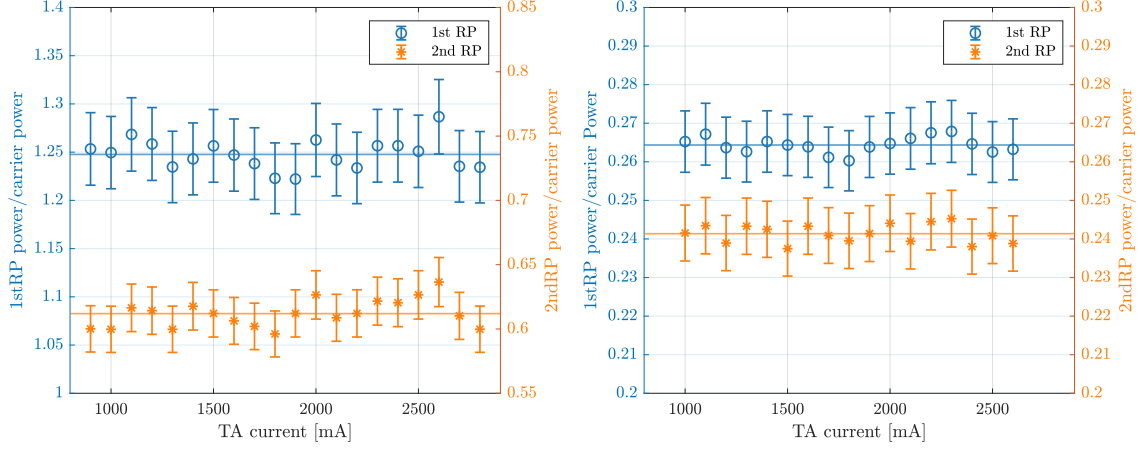
Figure 4.7: Power in the side bands relative to carrier power. On the left side, the side-bands were tuned to be higher than necessary in order to amplify possible fluctuations and to make them better visible. On the right side the side-bands are in the configuration needed for cooling and trapping of the krypton isotopes. The relative power of the repumpers remains stable for all applied currents. For cooling and trapping of krypton, the TA current is set to 2600 mA.

is not ensured for any TA chip. In a previous experiment, additional sidebands were already observed at 2000 mA. This depends strongly on the TA chip and the amplified sideband frequencies. In general, a large frequency difference between carrier and sideband enables stability in higher current regimes [91].

4.3 Performance monitoring with ^{83}Kr loading rates

The ^{83}Kr MOT loading rate is an essential tool for radio-krypton dating. It can monitor the machine's performance, determine the amount of krypton in a mixed sample and can be utilized for parameter optimization.

The loading rate is calculated as a linear fit from the loading curve of the trap. This curve is obtained by gradually increasing the loading time of the MOT by opening the cooling laser beam shutter for longer times and taking pictures of the fluorescent atoms. The laser beam switching is achieved with a fast shutter of few ms rise time. Due to the compact design of the laser setup and the premise of an unaltered argon laser system, the shutter was built in directly behind the 'MOT OUT' fiber for krypton in figure 4.4. Therefore both MOT and MOL were

shuttered which should not pose a problem in this setup, since only relative changes are studied.

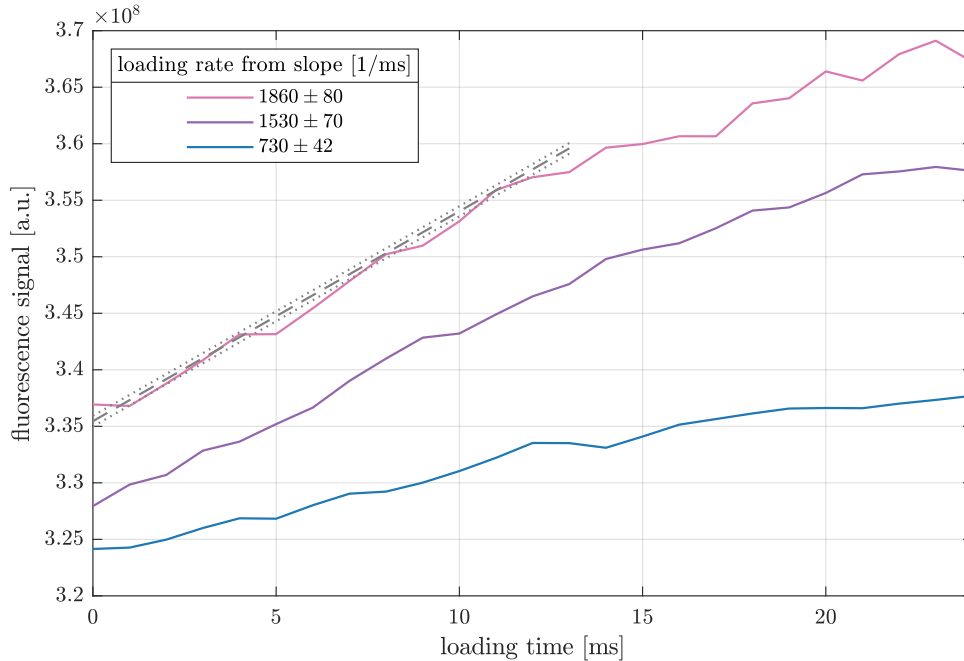Figure 4.8 shows three loading curves taken during a measurement run from section

Figure 4.8: MOT loading curve over time for a ^{83}Kr MOT. Three different realizations are shown here to represent the daily fluctuations of KrypTTA efficiency, which are small but still need to be accounted for when measuring samples. The curves' linear rise up to 13 ms was used to extract the loading rate from a linear fit which is exemplary shown for one measurement. The results for these three curves are shown in the legend.

6.3 The part of the curve which is actually used for the calculation of the loading rate ranges from 0 to 13 ms as can be seen by the solid gray line. This fitting time span of 13 ms was chosen, as the curve still increases linearly in this regime.

This shows the feasibility of ^{83}Kr loading rate measurements, which can be used in further performance monitoring and optimizing.

4.4 Vacuum setup modifications

A sample used to demonstrate ^{85}Kr dating extracted from 10 L of water may only contain $1\,\mu L$ of krypton gas [75]. Therefore, to ignite and sustain a plasma discharge, the sample needs to be mixed with argon gas. One very effective way to increase the

relative amount of krypton in the sample is to reduce the gas amount required for igniting the plasma and therefore reducing the argon admixture. However, running the plasma discharge at the ArTTA vacuum system requires a source pressure of at least 4×10^{-6} mbar.

The main ArTTA vacuum is composed of various vacuum chambers, individually pumped by turbo pumps of high pumping speed (two 2000L/s and three 300L/s). For a more detailed view on this, please refer to [66], since this thesis exclusively concentrates on the parts important for krypton samples.

When measuring a sample, the gas outlet of the main vacuum setup is connected to the source inlet again to reduce sample sizes. This process is called recycling, since the gas is reused continuously.

Due to the recycling, the gas volume needed to achieve the required source pressure is mainly limited by the vacuum design between the main vacuum and the source inlet. This is the so-called fore-vacuum. It also includes the sample preparation ports and bottled noble gases for throughput measurements (no recycling of the gas) and cleaning of the apparatus by running a plasma of other gas. The current design of this fore-vacuum is shown in figure 4.9.

The black colored part shows the ArTTA section of the fore-vacuum which was upgraded for krypton with the addition of the orange valves and tubes. The thickness of the connecting lines is a measure for the actual volume of these ducts, as some of them may be CF/KF 63, 40 or 25. Looking at the thickness and length of the connecting parts in the ArTTA fore-vacuum one can see that the volume is quite large.

The outlet of all pumps at the main chamber is connected to the recycling hose. The gas from this hose passes the getter pump, to prevent accumulation of gases other than noble gases while recycling, as well as the RGA to analyze the gas composition at all times. Then, the gas is compressed by a 50 L/s pump into the reservoir which in turn is connected to the source chamber via a dosing valve. This way, high, tunable pressures are achieved in the source chamber. Still, to obtain the required pressure for a gas discharge with this setup, at least $500 \, \mu$L of gas are needed, even after minimizing the reservoir.

For reducing the krypton sample size, the orange parts in figure 4.9 were added, creating a bypass directly from the compression pump to the source inlet. The samples were still prepared at the same sample port but were not pumped into the large reservoir. Instead they were compressed into the new KF25 flexible hose forming the bypass. Opening the orange valve next to the source would let the sample into the source chamber and also enable a coarse tuning of the pressure. Due to this modification, the required sample size could be reduced by a factor of 5 from $\sim 500 \, \mu$L to $\lesssim 100 \, \mu$L.
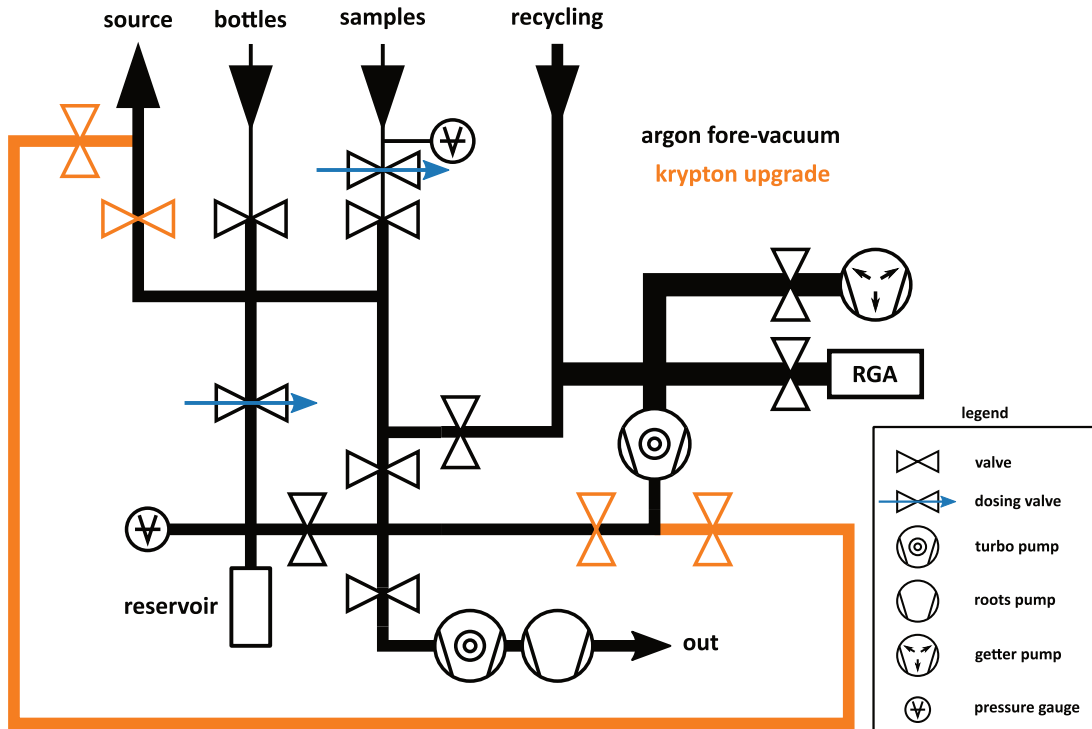
Figure 4.9: Schematic of the fore-vacuum. The existing ArTTA fore-vacuum (black parts) features the 'bottles' port, where large gas bottles for referencing or cleaning can be connected and the 'samples' port, where small environmental or artificial samples can be connected and prepared. The recycling hose collects the gas from all turbo pumps of the main chamber. Behind the recycling hose the getter pump removes accumulated gases which are not noble gases. An RGA analyzes the gas composition in the sample. The sample gas is then compressed into a sample reservoir by a 50 L/s turbo pump. Since this reservoir and the connected vacuum tubes are large in volume, a gas sample of $\sim 500\,\mu L$ is needed reach the pressure for plasma ignition in the source chamber. The addition of the orange hose and valves transforms this fore-vacuum to the D-ATTA fore-vacuum. With this, the necessary gas volume could be reduced to $\sim 100\,\mu L$.

4.5 ^{85}Kr counting setup

Single atom detection of ^{85}Kr was achieved with the same setup also used to count ^{39}Ar in the original ArTTA lab. The fluorescence light of single atoms inside the MOT is collected with a high NA objective and directed onto a multimode fiber

where an APD detects this small power increase. The employed setup in the container was discussed in the previous chapter, the exact setup used for KrypTTA is found in [51, 19] and [66].

4.6 Demonstration of a dual ATTA measurement

This section presents the combination of the previously discussed components to a dual Atom Trap Trace Analysis (D-ATTA) experiment. Due to the flexible laser setup, the apparatus can capture and detect both argon and krypton isotopes within a short time span. Table 4.1 shows the results of a first D-ATTA measurement. Within a time span of 24 h the rare radioisotopes ^{39}Ar and ^{85}Kr were detected, both with count rates applicable for dating, therefore verifying the performance of the D-ATTA apparatus and demonstrating the dating feasibility.

isotope	sample volume [μL]	admixture [Kr:Ar]	count rate [a/h]
^{39}Ar	616 ± 3	0:1	1.8 ± 0.3
^{85}Kr	627 ± 3	1:10	1420 ± 40

Table 4.1: First demonstration of a D-ATTA measurement. The two counting measurements were conducted within 24 h. Both count rates are applicable for dating, however, the sample size for krypton was even further reduced as was discussed in section 4.4.

Initially, the D-ATTA machine was set to detect the isotope ^{39}Ar. Only the argon laser frequencies were used and the ZSL magnetic field was set to the optimum for argon detection at $I_{ZSL} = 11.35$ A which is the typical ArTTA setup [66]. The measurement was conducted with a sample of ten times enriched ^{39}Ar concentration which is the current standard reference sample for radio-argon dating.

After the argon measurement, the flip-mirrors for the krypton laser beams were positioned to couple the ^{85}Kr laser beams into the D-ATTA fibers. The setup was discussed previously and is shown in figure 4.4. Then the ZSL current was reduced to the krypton optimum at ~ 8 A. This whole procedure takes only ~ 30 min, but due to the changed ZSL magnetic field, the compensation coil, which creates a steep decay of the ZSL magnetic field, needs to be tuned to optimize the magnetic field minimum, which defines the MOT position. This is achieved by capturing the isotope ^{83}Kr and observing the MOT loading rate. After this is optimized, the counting of single ^{85}Kr starts.

The ^{39}Ar count rate is approx. three times lower than previously presented count rates at the same apparatus [66]. However, the measurement presented here was the last one of only four measurements conducted over two days. Since ^{39}Ar is more complicated to detect than ^{85}Kr (it is $\sim$20000 times rarer), small changes on the

apparatus have a stronger relative effect on efficiency. Therefore the ^{39}Ar count rate is not very robust and requires frequent monitoring and adjustment. Before the argon measurement phase, the apparatus was detecting krypton for one month. As argon will be measured more frequently in the future its detection efficiency will be observed and optimized more continuously, resulting in a stable count rate in the range of 6 a/h.

The ^{85}Kr count rate is definitely suitable for radio-krypton dating but the sample size is still an issue. Igniting and sustaining the plasma discharge requires $500\,\mu$L of gas. This amount of argon can be extracted from about 1.5 kg of water or ice [66] which in turn only contains roughly $0.15\,\mu$L krypton gas. Table 4.1 already shows that this is overcome by adding argon gas to the krypton sample. Modifications on the D-ATTA vacuum setup which were discussed previously in section 4.4 reduced the required sample size to $100\,\mu$L. The to-be-broken water volume barrier of 10 L, which is set by a standard Niskin bottle [66], corresponds to only $1\,\mu$L of krypton gas. Producing a sample with 100 times more argon gas yields the required sample volume.

The gas extraction setup employed for argon sample production [92, 93] degases water or ice and removes everything except noble gases with getter pumps similar to the one used in the D-ATTA vacuum system. The final sample for radio-argon dating therefore contains all noble gases solved in the water, which is $\gtrsim 99.9\,\%$ argon and $\sim 0.02\,\%$ krypton gas. The krypton separation setup designed by Yannis Arck [75] further processes this sample to reduce the argon amount yielding up to 80 % pure krypton gas. Reducing this purity can without any further mixing directly generate the desired 1:100 krypton to argon volume sample.

However, the dilution reduces the count rate by a factor of 10 compared to table 4.1, resulting in ~ 140 a/h. Still, this is 20 times higher than the ^{39}Ar count rate and therefore allows for radio-krypton dating. First measurements of $1\,\mu$L large artificial ^{85}Kr samples demonstrate the feasibility of the dating and will be presented in the section 6.3.

The demonstration of a D-ATTA system opens the possibility of radio-argon and radio-krypton analysis in the same sample extracted from 10 kg of water or ice. Mixing the samples enables a direct measurement of both isotopes, as the 1:100 krypton to argon sample will be prepared with noble gases originating from the same water. This offers a direct atmospheric contamination check of the sample or, regarding transit-time distributions [28], analysis of mixing processes in water bodies. This offers the possibility for more thorough tracer studies within one machine and upgrades the portfolio of the Heidelberg ATTA collaboration.

5 Radio-krypton counting and analysis

5.1 Challenges in radio-krypton analysis

Although there are many similarities between the detection of rare argon and krypton isotopes, some serious differences remain. For both, demonstrating the performance of the apparatus is essential before the study of environmental samples. In both cases, this performance is tested with artificial samples of varying radio-argon or radio-krypton amount. This amount is typically given in percent modern [pm], meaning that a sample of 100 pm is of atmospheric concentration, whereas 0 pm does not contain the desired radio-isotope at all. This is usually called a 'dead' sample, since it is not radioactive any more.

These varying defined concentrations are typically 0 pm, 10 pm, 33 pm, 66 pm, and 100 pm. In the end, all the obtained count rates are plotted against defined concentration producing the desired performance graph. As the amount of radio-argon or radio-krypton atoms increases, the detected count rate should increase accordingly, ideally resulting in a perfect linear correlation between these two. The agreement between measurement data and the expected linear behavior is the benchmark for the ArTTA or KrypTTA performance.

For the ArTTA machine this graph can be extracted from the PhD thesis of Sven Ebser [66] and is displayed in figure 5.1. The measured count rates exhibit the expected linear behavior, demonstrating the feasability of ^{39}Ar analysis.

One goal of this thesis was to achieve a graph similar to figure 5.1 for ^{85}Kr as a benchmark for radio-krypton dating with KrypTTA and D-ATTA. Artificial samples of the same radio-isotope concentration were used. These were mixed by Yannis Arck from atmospheric krypton and a sample of dead krypton provided by Roland Purtschert. The measured count rates plotted against these defined concentrations are shown in figure 5.2.

The dashed line represents the perfect agreement between measured and expected count rate. There are considerable differences between the graph for ^{39}Ar (5.1) and ^{85}Kr (5.2). The measured count rates in figure 5.2 do not exhibit a linear correlation at all. Looking at the measured count rate for the 0 pm sample especially, the grave difference to the expected count rate of 0 atoms per hour to the measured count rates of ~ 40 atoms per hour is striking. This means that even with a sample that does not contain any ^{85}Kr, the measurement still yields a count rate of 40 a/h.

This discrepancy is caused by atoms that come from other sources than the sample itself. These atoms are called **contamination atoms**. The contamination can
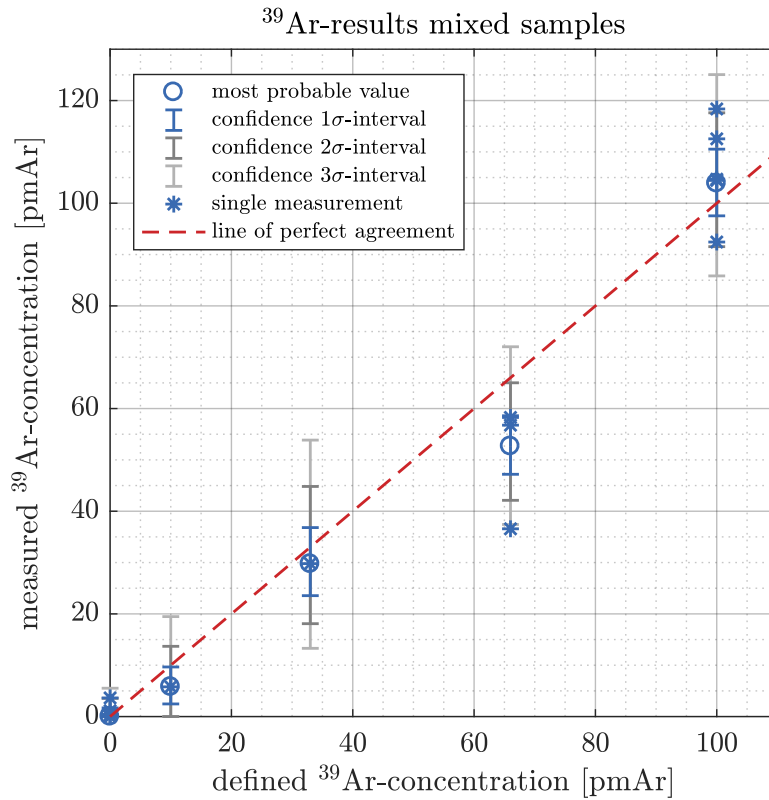
Figure 5.1: Measured ^{39}Ar concentration of artificial samples as a function of the defined concentration. The dashed line is a guide to the eye and indicates the perfect agreement between measured and defined concentration. The measurement points are all in good agreement with this expected line. Figure taken from [66].

originate from different processes and effects. This chapter aims to thoroughly study these, to subtract all contamination atoms from the sample. This will reveal the real count rate, which would, in the case of figure 5.2, lead to a graph more similar to figure 5.1. Such an agreement of the measured count rates with the expected ones will finally provide the benchmark for the performance of the KrypTTA machine, making ^{85}Kr analysis of environmental samples feasible.

5.2 Origins of contamination

The different origins of contamination atoms were already discussed for the radio-krypton ATTA-3 machine at the ANL in [53] and for the ArTTA apparatus in [66] respectively. However, the KrypTTA apparatus differs from both machines in either
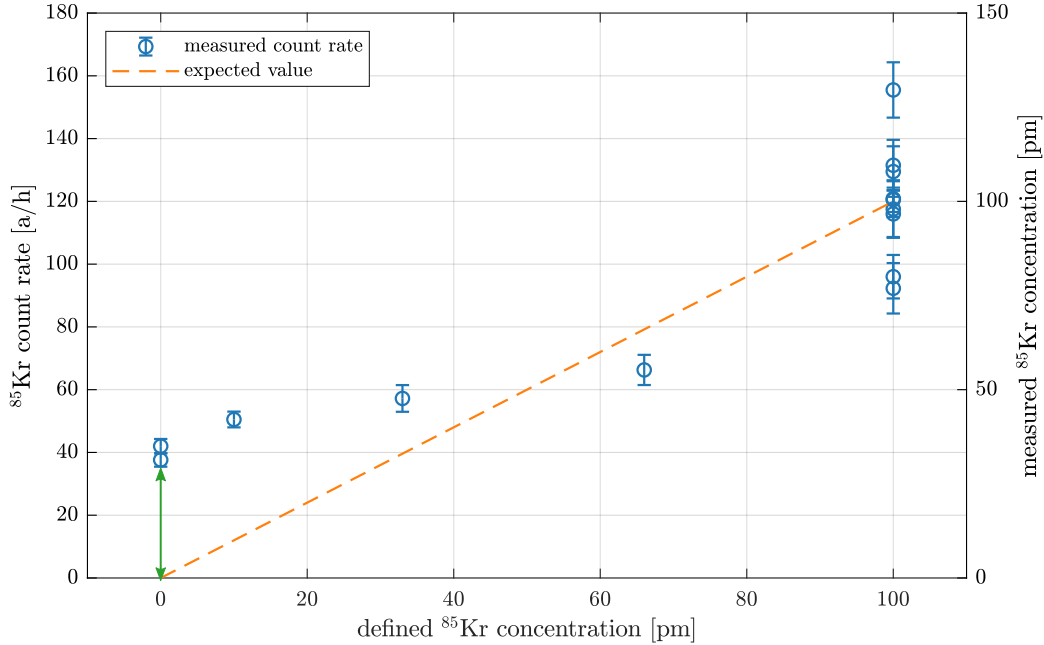
Figure 5.2: ^{85}Kr count rates calculated from counted atom number over time. The measured concentration is calculated by referencing these onto a 100 pm sample. The orange dashed line shows the expected perfect agreement between defined and measured ^{85}Kr concentration. The green vertical arrow points out the observed difference between the expected count rate of a dead krypton sample and the measured one.

vacuum system or used noble gas, requiring its own specific study of contamination origins. In order to find those and discuss their individual strength, the typical contamination effects experienced at other ATTA machines are reviewed.

First, the effect of residual gas is discussed. As the new sample is prepared at the sample port, the previous sample is pumped from the vacuum system. This can be neglected, because in all measurement runs, care was taken to always pump the previous sample until a source chamber pressure of $\sim 3 \times 10^{-8}$ mbar was achieved, which is more than two orders of magnitude lower than the pressure with a sample present ($\sim 6 \times 10^{-6}$ mbar). If there is any residual gas in the chamber, this would have also been observable in the residual gas analyzer (RGA) which is connected to the vacuum system. Residual gas would show as leftover argon and krypton in the same composition as in the previous sample.

However, a second effect is that parts of the previous sample freeze to the cold regions in the plasma source. The source is cooled with liquid nitrogen to shift the

initial velocity distribution towards lower values. For ^{39}Ar and ^{85}Kr this increases the count rate by a factor of four [51, 94]. At the ArTTA apparatus, this so-called 'cross-contamination' [66] is negligible since argon freezes at lower temperatures than krypton [95]. Also the ArTTA sample size is usually five times larger than the krypton sample volumes used in this thesis [52] and two orders of magnitude larger than samples used in ATTA-3 [12]. Naturally, for the microscopic samples of $5 - 10\ \mu$L at the ANL, freezing is an issue. In their setup, this is overcome by pumping the vacuum system whilst running a hot xenon plasma discharge for up to 18 hours [53] or totally removing the liquid nitrogen cooling and disregarding the count rate increase [94].

For the KrypTTA, a hotter plasma source without liquid nitrogen cooling can not be achieved with the current source design, since it contains indium. This metal will quickly melt at higher temperatures, which are definitely reached as soon as the plasma discharge is running for longer times ($\gtrsim$15 minutes) without cooling. Contamination contributions from the source can be identified by monitoring the pressure at the moment of plasma ignition. There they appear as a sudden gas increase as the source becomes hotter at ignition and releases frozen gas. At later times, it becomes colder again, as a thermal equilibrium is established. From this point on, the freezing of gas on the source begins.

The final contribution is from radio-isotope ions embedded in the chamber walls. The ions inside the plasma are strongly accelerated due to the high fields in the source. Some of them hit the vacuum chamber walls with high velocity and are implanted into it [66]. Other fast ions created in the source can later release them from the wall. At the ATTA-3 machine, the contamination of a sample is then caused by previously measured samples of high radio-krypton concentration. Letting the plasma source run with xenon for many hours suppresses this effect by replacing the krypton ions in the wall with xenon ions [53].

At the ArTTA apparatus some vacuum chambers were highly ^{39}Ar enriched due to past measurements with strongly enriched samples. These chambers were mostly replaced which resulted in a decrease of contamination by a factor of 6 [66]. A highly enriched sample can therefore imprint a long term memory effect on the chamber walls, resulting in the constant contribution of contamination atoms. For the ArTTA, this causes the main contamination contribution [66, 52]. These contamination atoms only appear if the plasma discharge produces fast ions and – unlike the frozen gas – their amount increases the longer the plasma source is running.

All these effects are studied with the measurement of a dead sample, where all the atoms counted in this sample are contamination atoms. After this measurement, the accumulated number of detected atoms over time is analyzed. The increase of atoms over time behaves differently for the two significant contamination effects:

- **Frozen gas:** Gas from a previous measurement is released as the source heats up in the beginning of a measurement. Since all the contamination is set free

at the same time, it behaves like an additional sample introduced into the chamber with a certain, constant count rate c_{lc}. This constant count rate results in a measured cumulated atom number N_m increasing linearly with time

$$N_m = c_{lc}t.$$

Therefore it is referred to as the **linear contamination**. It can be reduced by pumping the chamber whilst running the plasma discharge of a not-cooled source. This process is called cleaning or flushing.

- **Chamber wall contamination:** Ions are embedded in the vacuum chamber walls and are kicked out by fast ions generated in the plasma source. The number of atoms extracted increases linearly with time. This results in a quadratic increase of measured atoms over time

$$N_m = \frac{1}{2}a_{qc}t^2.$$

Therefore this is referred to as the **quadratic contamination**. The coefficient a_{qc} is the constant contamination acceleration [66].

Analysis of the linear and quadratic increase in cumulated atom number N_m measured in a dead sample directly returns the contribution strengths of these two contamination origins. These dead sample measurements or **contamination measurements** are discussed in the next section.

5.3 Study of contamination measurements

During the course of this thesis, many contamination measurements were conducted, even before the dead krypton gas was made available by Roland Purtschert. The measurements before were done with dead argon, because this also contains no ^{85}Kr [96]. A typical measurement is shown in figure 5.3.

One can observe that the cumulated atom number over time has a quadratic and a linear part. The contributions of both parts were extracted from this plot with a polynomial fit in a *MATLAB* script. The fit is shown as the orange, solid line, measured atoms are blue dots. To make the importance of the linear part for krypton more apparent, the green dashed line shows the accumulation of atoms for only the quadratic part. It should be noted that contamination measurements with dead argon in the ArTTA apparatus show mainly the quadratic behavior and no linear contribution.

To compare krypton and argon even further: The ^{39}Ar contamination acceleration is $a_{ar} = 16\,\mu\text{L}c_0/\text{h}$ [66], so for this sample in figure 5.3 this would be $a_{ar} = 0.13\,c_0/\text{h}$, with the sample volume of 120 μL and the reference count rate c_0. With a reference
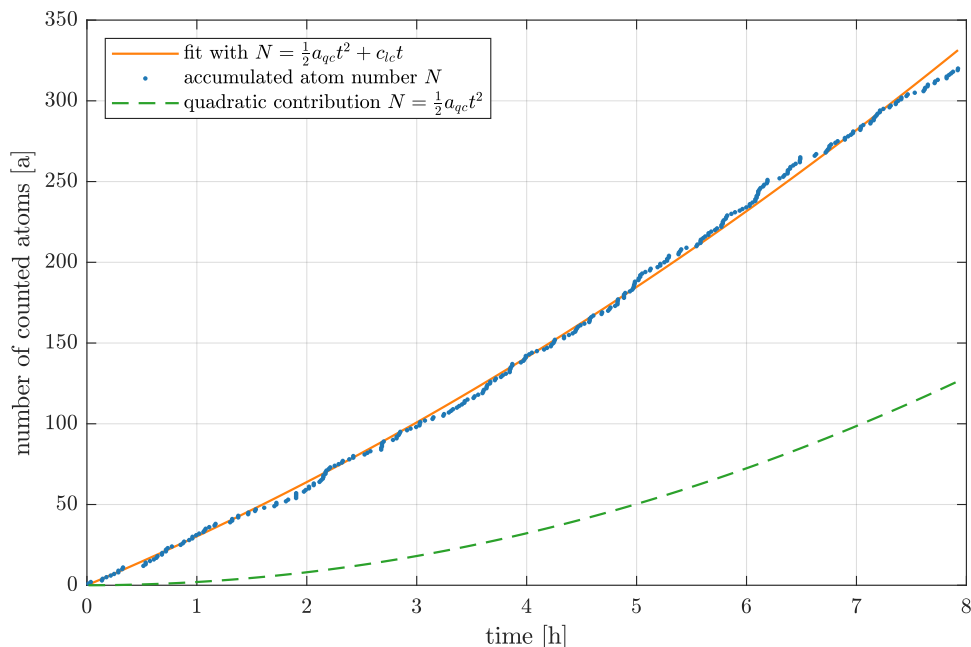
Figure 5.3: Number of counted ^{85}Kr atoms in a dead krypton sample over time (blue dots). The contribution of the quadratic and linear contamination were extracted from a polynomial fit with *MATLAB* (orange, solid line) and used for the contamination correction. In order to compare the processes of contamination between argon and krypton, the green dashed line shows only the quadratic part of the contamination, as it would look like for a dead argon sample in the ArTTA apparatus.

count rate of $\sim 120\,\text{a/h}$ and $8\,\text{h}$ measurement this would lead to $N_m = \frac{1}{2}a_{ar}t^2 \approx 500\,\text{a}$. Compared to this, the number of atoms obtained from the quadratic increase in the dead krypton fit is only ~ 130 atoms as can be seen in figure 5.3. This discrepancy is could be caused by the highly ^{39}Ar enriched contamination coming from the vacuum chamber walls. For krypton, no such highly enriched sample was ever measured resulting in a lower quadratic contribution to the contamination. Another possibility is a difference between argon and krypton considering the ability to be implemented into or extracted from the vacuum chamber walls.

With the linear contamination having such a large impact on the measurement, it needs to be studied closer. Since it is caused by past samples frozen on the source it is altered by previous ^{85}Kr concentration, warming up the source and running the plasma discharge. The study of these effects on the linear contamination is essential and can only be done by repeated dead krypton measurements. During the course

of this thesis, eleven of these dead krypton measurements were performed, varying in previous samples measured and in prior cleaning processes.

Figure 5.4 shows all measurements grouped by the sample previously present in the
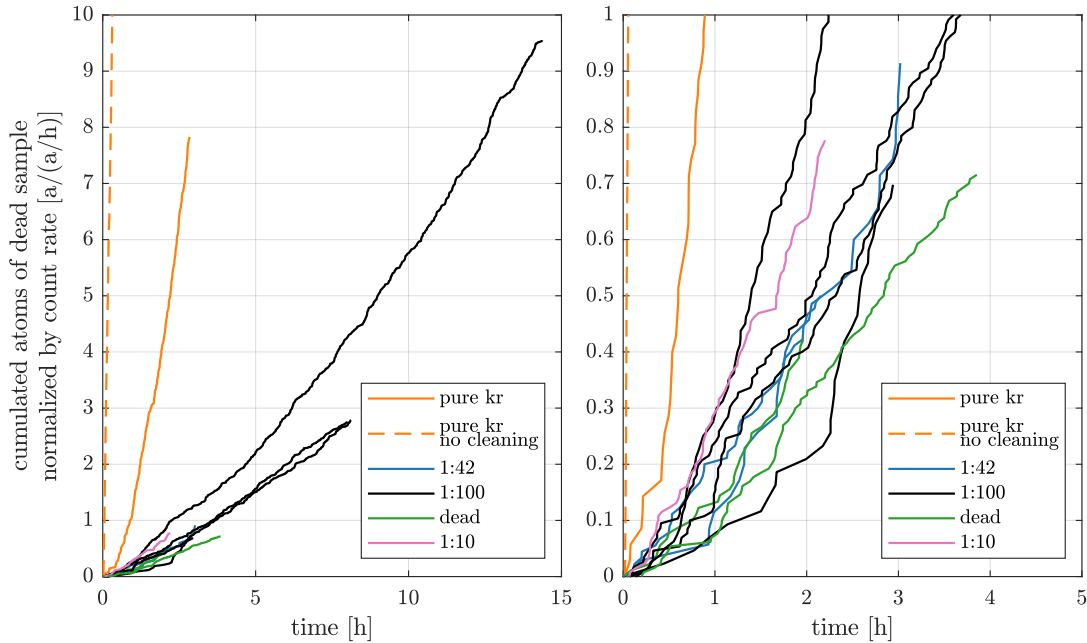

Figure 5.4: All contamination measurements with color indicating the sample measured before. The number of counted atoms is divided by the corresponding current count rate c_0, to prevent differences in the graphs caused by fluctuating count rates. On the left are all measurements in their total time, the right side shows a closer look to the short time effects. Samples of high ^{85}Kr amount strongly increase the contamination of the following dead sample. However, as the ^{85}Kr amount decreases more, the contamination seems to be unaffected by the previous sample.

source chamber. If the contamination is a short-term memory effect, meaning that it is governed by the previous sample composition, the contamination atoms will increase if the previous sample is of high ^{85}Kr concentration. As one can observe in figure 5.4, a previous sample of pure krypton increases the contamination of the following sample significantly. Towards the lower previous concentrations however, the contamination measurements show the same behavior, regardless of the previous sample composition. A difference between a preceding 1:10, 1:42 or 1:100 Kr:Ar volume mixture can not be found and even a previous dead argon sample does not change the linear contamination. These results show that even the linear contam-

ination is not purely a short-time memory effect. Not only the samples measured directly prior contribute to it, but also others examined before.

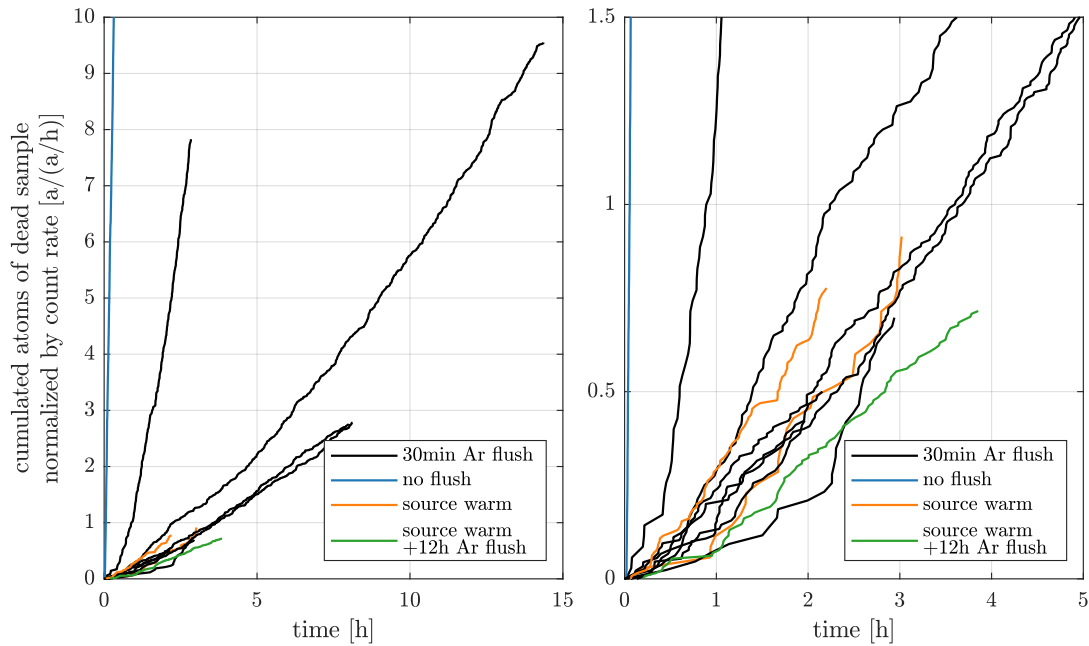One can also examine the dead krypton measurements under another aspect,

Figure 5.5: All contamination measurements with color indicating the cleaning procedure before. The number of counted atoms is divided by the corresponding current count rate c_0 to prevent differences in the graphs caused by fluctuating count rates. On the left are all measurements in their total time, the right side shows a closer look to the short time effects. The most employed cleaning procedures was a 30 minutes flush with argon gas where the source was warmed up briefly to release the frozen gas, shown in black. The blue curve represents one measurement without flushing before. For the orange and green curve the source was heated up completely without a plasma. The measurement shown in green features an additional 12 h argon flush. Comparing the curves with a situation, where no cleaning was employed, the necessity of this flushing process becomes apparent. However, a 30 minute long cleaning seems to be comparable to other applicable cleaning techniques.

namely the cleaning procedure employed before the sample measurements. Most of the times, the cleaning procedure was the same, a 30 minutes flush running an

argon plasma discharge where the source was briefly not cooled[1]. However, other procedures were tested as well. Figure 5.5 shows these measurements as before with the cumulated atom number over time. One can directly see that not cleaning the source at all results in an extreme contamination, as can be seen in the fast rising atom number. It should be kept in mind that the graph with the second highest slope had a previous measurement of pure krypton (see figure 5.4). The other graphs show again a very similar behavior. This shows that a 30 minute argon flush is necessary to clean the biggest portion of the contamination, and that longer running of the cold argon source, briefly heating the source or heating up the source without a running plasma will not significantly decrease the contamination. A thorough cleaning can be achieved by running the plasma discharge whilst warming up the source for 16 h [94]. This procedure is unfortunately not yet available due to the non-heat resistant parts of the plasma source.

To conclude this section: the linear contamination is a bigger challenge for krypton than initially expected. Efficient source cleaning is not feasible but can be achieved with redesigning the source for future KrypTTA machines (see section 7.1)).

5.4 Analysis of artificial sample measurement campaign

One possible way to reduce the impact of contamination is to employ the same measurement routine at all times, meaning same cleaning processes, comparable ^{85}Kr amount and same measurement times. This is exactly what was done in the measurement campaign of the artificial samples. As mentioned previously, the goal is to benchmark the performance of the KrypTTA dating apparatus by measuring the ^{85}Kr concentration of artificial samples and thereby producing a performance graph similar to figure 5.1. To reduce the initial contamination an argon plasma was running for two days and the source was heated up for an additional day. After this, the highest ^{85}Kr concentration was of the 100 pm sample with a mixture of 1:100 Kr:Ar, which also served as a reference. The measurement times of sample and reference were chosen to be 8 h and 2 h, respectively. The cleaning procedure was employed after each measurement in the exact same way to enable a more reliable contamination description. A schematic of the time line is shown in figure 5.6.

---

[1]This brief non-cooling is also used while argon dating. In this realization, the liquid nitrogen supply to the source is switched off while the source is running. One can observe the increase of pressure and the release of gas on the RGA. After 8-10 minutes, the cooling is switched back on. This procedure can be repeated a number of times, typically three to four times.

5.4.1 Count rate versus super ratio

Before the contamination can be corrected, it needs to be clarified what kind of parameter will be used to describe the measurement results. It needs to contain all relevant information on the system. For ArTTA, the ^{39}Ar count rate was always the standard result. Subtracting the contamination and comparison with a reference count rate would directly result in the ^{39}Ar concentration of the sample. The krypton analysis differs from this since the measurement system allows for more variabilities in ^{85}Kr count rate.

For argon, the count rate is affected by ^{39}Ar concentration and machine performance, where the latter is continuously monitored during a measurement and also determined with a reference sample. Together with the analysis of the reference the sample concentration can be extracted. The krypton count rate underlies more variations. For one, the krypton samples are all mixed with argon where small variations in the mixing ratio might occur but are $\sim 1\,\%$ for the 1:100 mixtures and $< 10\,\%$ for the smallest relative krypton amount in a 1:500 sample. Additionally, the outgassing from the source has a significant impact on the overall source pressure, which in turn has a large impact on the plasma efficiency. These effects are not as substantial for argon, since the sample volume is at least five times larger.

With krypton, checking the performance of the complete KrypTTA for each measured sample is possible by monitoring the ^{83}Kr loading rate. Due to the hyperfine structure, testing the performance of the repumper sidebands prior to each ^{85}Kr counting is possible. Since argon offers no abundant isotope with a hyperfine structure the complete laser setup for ^{39}Ar can only be tested with a known reference sample.[2] The ^{83}Kr MOT can monitor all changes in ^{85}Kr capture efficiency since it is affected by source pressure, mixing errors and plasma efficiency in the same way as the ^{85}Kr count rate is, but without activity playing a role.

Therefore the bare count rate is discarded as a dating parameter for krypton. Instead, the ratio between ^{85}Kr count rate and ^{83}Kr loading rate is used as the result of a sample measurement. As it is for argon, this result is compared to a reference measurement. For this reference, also the ratio between ^{85}Kr count rate and ^{83}Kr loading rate is given. Finally, the two ratios of sample and reference are divided. The result is called the **super-ratio** S

$$S = \frac{c_{sample}/LR_{sample}}{c_{ref}/LR_{ref}} \tag{5.1}$$

with the loading rate LR and count rate c for sample and reference, respectively.

This analysis scheme is already applied for ^{85}Kr and ^{81}Kr dating in the ANL group [53], but in a more elaborate way. The loading rate is not obtained once per measurement but multiple times during one measurement. This enables a higher

---

[2]Still the abundant isotopes without nuclear spin are used for monitoring the machine before each measurement of sample or reference.

resolution of S and the detection of different plasma modes with varying metastable efficiency also during a running atom detection. The analysis scheme of the super-ratio S will also be used in this thesis, thereby replacing the count rate.
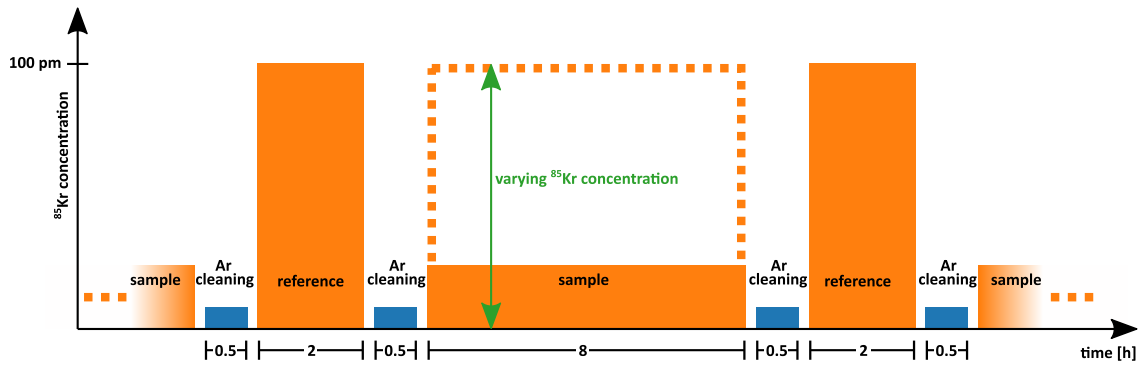
5.4.2 Final contamination correction

Figure 5.6: Schematic of the measurement procedure employed for the artificial samples. The time spans are given in hours and were chosen to result in a 12 h cycle while providing enough time to reach $\sim 10\,\%$ counting error for all samples. The references are of modern concentration with 100 pm, others feature a lower ^{85}Kr amount as indicated by the green arrow.

Now, the correction of the contamination can begin. In general, the contamination of a sample is understood by looking at the number of accumulated atoms over time for a dead krypton sample, as shown in figure 5.3. Since the dead sample itself does not contribute any ^{85}Kr, the number of measured contamination atoms N_m is

$$N_m = \frac{\zeta}{V_s}c_{lc}t + \frac{\eta}{V_s}c_{cq}t^2 \tag{5.2}$$

where V_s is the sample volume, t the measurement time[3] and c_{lc} and c_{qc} are the count rates of the linear and quadratic contamination. The contamination acceleration a was discarded to account for the dependency of the quadratic contamination on previously measured samples. Although it is suitable for the ArTTA apparatus, a constant quadratic contamination depending on a does not fully represent the

---

[3]Actually, the quadratic contamination does not scale with the squared measurement time t^2 but the time since the source is running t_0^2, because this determines the amount of released ions from the vacuum chamber walls. Since the measurement is directly started as soon as the source is running and for simplicity, t^2 is used here.

system for krypton. The volumes in equation 5.2 are necessary, since a sample is less affected by contamination as its volume increases. While the total amount of contamination atoms may not change, their relative impact does.

The linear and quadratic contamination coefficients ζ and η are given in [mL] and [mL h^{-1}], respectively. They give a measure for the amount of gas added to the sample, normalized by the count rate c_0. In order to determine these coefficients, a dead sample was measured during the course of the artificial sample campaign. The accumulated number of atoms over time is shown in figure 5.3. A polynomial fit with *MATLAB* was used to extract the slopes of the linear and quadratic term. They were found to be

$$N_m = 28.4 \text{ a/h } t + 1.75 \text{ a/h}^2 \, t^2. \tag{5.3}$$

Still, the count rates c_{lc} and c_{qc} are missing to extract ζ and η. For the case of the dead krypton measurement used for the fit, the previous sample was a $100\,$pm sample with a 1:100 krypton to argon mixture, which was used as a reference sample before and after each measurement in the artificial sample campaign (see 5.6). Since the linear contamination count rate is dominated by the count rate of the previous sample, c_p, one can write $c_{lc} = c_p$.

The magnitude of the quadratic contamination is limited to the highest count rate present in the machine during any other longer continuous running of a krypton discharge. Running the discharge with argon for longer, on the order of days, suppresses the quadratic contribution and resets the contamination [53]. During the artificial campaign, the highest count rate was the one of the reference, therefore one can substitute $c_{qc} = c_{ref}$.
Coming back to equation 5.2, one can now write

$$N_m = \frac{\zeta}{V_s} c_p t + \frac{\eta}{V_s} c_{ref} t^2 \tag{5.4}$$

where ζ and η will be extracted from the fit parameters of equation 5.3. Now, in order to take care of possible performance changes of the machine between the dead sample and its following reference, the ^{83}Kr loading rate LR of both measurements is employed to obtain

$$N_m = \frac{\zeta}{V_s} c_p \frac{LR_c}{LR_{ref}} t + \frac{\eta}{V_s} c_{ref} \frac{LR_c}{LR_{ref}} t^2. \tag{5.5}$$

With LR_c and LR_{ref} being the loading rates of the contamination and reference measurement. This results together with equation 5.3 in the final equations for the
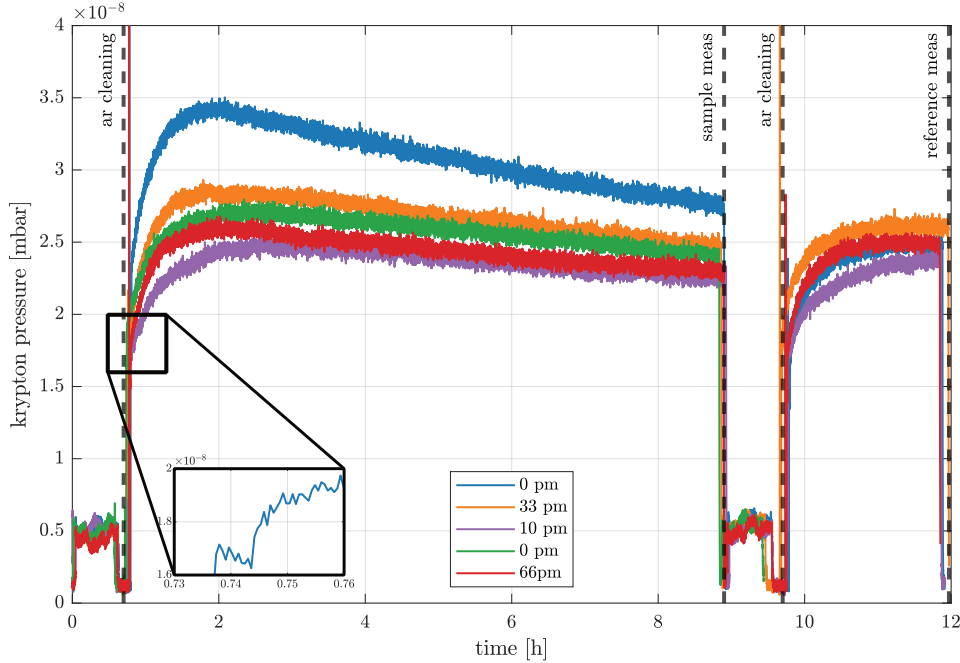
Figure 5.7: Krypton gas pressure over time for the artificial sample measurements. The data was obtained with the RGA where all sample measurements show comparable pressure curves, different colors reflect different samples. Vertical dashed lines represent the measurement stages. Each measurement starts with 30 minutes argon cleaning, where the krypton pressure rises to 0.5×10^{-8} mbar because the source releases frozen gas. Then the chamber is pumped and the sample gas is let in. The plasma source is ignited and slowly, over the course of 2 hours, krypton gas is released from the source. The inset shows a zoom in of the beginning of one krypton measurement. One can see a small plateau in the beginning, where the gas is let in, but the source is not yet running. The following jump in krypton pressure is caused by igniting the source and releasing the gas frozen to it. All of the pressure traces exhibit this behaviour in the beginning of both sample and reference measurement, but for clarity only one trace is shown here. After 2 hours the pressure begins to fall until the source is switched off after 8 hours of measurement and the sample is pumped. Another cleaning process starts and is followed by the measurement of the reference, which takes 2 hours. A rise in krypton pressure can be observed.

contamination contribution coefficients

$$\zeta = \frac{28.4\,\mathrm{a/h} \cdot V_s \cdot LR_{ref}}{c_p \cdot LR_c} = 29\,\mu\mathrm{L} \quad \mathrm{and} \quad \eta = \frac{1.75\,\mathrm{a/h^2} \cdot V_s \cdot LR_{ref}}{c_{ref} \cdot LR_c} = 1.8\,\mu\mathrm{L\,h^{-1}}.$$
(5.6)

Having calculated the contribution of both contamination origins with the measurement of a radio-krypton dead sample, one can finally go on to correct the measured samples for contamination. Since the count rate itself is no longer the best analysis result, as discussed above, the sample's super-ratio S is now of interest. The contamination will be subtracted from the measured super-ratio S_m, to obtain the real sample super-ratio S. Combining linear and quadratic contamination and the contribution of the sample results in this expression for S_m:

$$S_m = \frac{\zeta}{V_s}S_{lc} + \frac{\eta t}{V_s}S_{qc} + \left(1 - \frac{\zeta}{V_s} - \frac{\eta t}{V_s}\right)S$$
(5.7)

$$= \frac{\zeta}{V_s}S_p + \frac{\eta t}{V_s}S_{ref} + \left(1 - \frac{\zeta}{V_s} - \frac{\eta t}{V_s}\right)S.$$
(5.8)

Note that the super-ratio of the quadratic contamination is set to be the same as for the reference $S_{qc} = S_{ref}$, because S_{qc} is determined by the highest ^{85}Kr amount in temporal vicinity of the sample, which is the reference in this case. All other measured samples are of lower ^{85}Kr amount. The linear contamination is mainly governed by the previous measurement so one can substitute $S_{lc} = S_p$, with S_p being the super-ratio of the previous sample.

The last contribution in equation 5.8 is of the sample with super-ratio S. But as one can see, this contribution is reduced by the contamination coefficients ζ and η. This reduction is caused by sample freezing on the source and implantation of fast krypton ions into the walls. Note that this equation only holds true for the measurement times discussed in this thesis which are $\leq 8\,\mathrm{h}$. As time evolves further the samples' contribution to the counted atoms decreases due to the growing subtrahend $\eta t/V_s$. It can even become negative after 50 h which is physically illegitimate. Still if contamination atoms leave the vacuum chamber with the rate η then also atoms have to be implemented with the same rate. However, after 8 h the contribution of the subtrahend in equation 5.8 is only 10 % and does therefore not strongly affect the results of the sample measurements. For longer measurement times equation 5.8 should be revisited by a more extensive study of dead samples and replaced by a more elaborate rate equation.

Figure 5.7 demonstrates the impact of the source freezing described by ζ. It shows the krypton amount measured with the RGA during the measurements of artificial samples (see also the schematic in figure 5.6). Each line shows the 8 h sample measurement followed by the 2 h reference measurement of one measurement cycle. In between the liquid nitrogen is refilled and the source is cleaned for 30

minutes. During the 8 h measurement period, the krypton amount increases in the beginning (see the inset of figure 5.7), which is caused by the linear contamination, and decreases at the end due to sample freezing on the cold source. For the short reference measurements only the krypton increase is observed, most likely since the source needs to be cooled longer after igniting the plasma to achieve the low freezing temperatures.

Samples

Equation 5.8 can be simplified by looking at the super-ratios S_p and S_{ref} for the previous and the reference measurements. For a sample measurement (meaning not a reference or contamination) the preceding measurement is always a reference, since all sample mesurements are framed by two reference measurements. Therefore it is $S_p = S_{ref} = 1$ by definition of the super-ratio. This, as well as rearranging eq. 5.8, results in this expression for the sample super-ratio S

$$S = \left(S_m - \frac{\zeta}{V_s} - \frac{\eta t}{V_s} \right) \left(1 - \frac{\zeta}{V_s} - \frac{\eta t}{V_s} t \right)^{-1}. \tag{5.9}$$

However, the determination of the measured super-ratio S_m still needs to be done. As mentioned above, $S_m = \frac{c_m/LR_m}{c_{ref}/LR_{ref}}$, where the loading rates LR_m and LR_{ref} are directly measured and not prone to contamination and c_m is the measured atom number divided by measurement time. For these three values, no contamination or other further calculations are necessary. The reference count rate c_{ref}, on the other hand, needs to be contamination corrected.

References

For the reference correction, one should take a look at figure 5.7. As mentioned before, the reference measurements are very short with only 2 h. Prior to the measurement, the source is flushed with argon and briefly warmed up. Figure 5.7 shows that the krypton pressure increases in the beginning, when the source is ignited, but no decrease for longer times as it is seen for the samples. This suggests that the source is still warm enough to not let significant amounts of the krypton sample freeze to it.

Figures 5.3, 5.4, and 5.5 show that in the first 2 h the atom number increase is dominated by processes linear in time. This allows the restriction of the model for reference measurements to linear increases in atom number, neglecting the quadratic part. Therefore the measured atom number N_m is

$$N_m = \frac{\zeta}{V_{ref}} c_p t + c_{ref} t. \tag{5.10}$$

The sought reference count rate is c_{ref} and c_p the count rate of the previous sample. One can now solve for c_{ref} to obtain

$$c_{ref} = \left(N_m - \frac{\zeta}{V_{ref}} c_p t \right) t^{-1}.$$ (5.11)

The previous count rates c_p need to be calculated for each reference measurement individually. They are the bare count rates of the directly preceding measurement.

With all required measured and corrected values one can go back to equation 5.9 and plug in the numbers, finally obtaining the desired sample super-ratio. These super-ratios are then used for a KrypTTA performance graph similar the one for argon in figure 5.1. This gives the benchmark for measuring environmental samples with the KrypTTA apparatus. The determination of this curve is shown in the next chapter.

6 Reducing the ^{85}Kr dating sample size

This thesis features the first application of the KrypTTA apparatus on the measurement of artificial samples with various ^{85}Kr activity. The goal is to demonstrate the feasibility of radio-krypton dating in environmental samples extracted from 10 L of water, which is the equivalent of 1 μL krypton gas.

This chapter shows how this performance was reached. In general, the way towards this can be divided into two major steps: The enhancement of ^{85}Kr count rate, and, as the sample is a mixture of krypton and argon, the identification of the ideal sample composition. The results of various experiments with the isotopes ^{83}Kr and ^{85}Kr are discussed and interpreted to boost the KrypTTA performance.

The chapter concludes with the analysis of five samples of various ^{85}Kr activity, setting the benchmark for future measurements of environmental krypton samples extracted from 10 L of water. This sample volume also enables ^{39}Ar dating making D-ATTA measurements feasible.

6.1 Improvement of ^{85}Kr count rate

A high ^{85}Kr count rate reduces the measurement times, makes higher argon admixtures and therefore smaller krypton sample sizes possible, and enhances the measurement precision. As capturing ^{85}Kr was new to this ArTTA dating machine, an extensive study to increase its flux into the magneto-optical trap is essential before the detection.

6.1.1 Enhancement factors on ^{85}Kr count rate

First, the effects of the atomic optical tools like the COL and MOL on the ^{83}Kr loading rate and ^{85}Kr count rate are studied and compared to the well-known effects in argon.

An essential routine for monitoring the machine's dating performance is taking a so-called 'vector', which is an array of enhancement factors. These factors are measured by reading out the flux of meta-stable ^{40}Ar recorded by the beam imaging, and referencing them to a base-line. More background on the beam imaging tool is found in section 3.3 and in [35]. For the ArTTA experiment this base line is the 'bare' flux of meta-stables behind the MOT without the flux enhancing COL and MOL.

In this KrypTTA realization of the vector, not the ^{40}Ar beam imaging but rather the ^{83}Kr MOT loading rate is employed, since the current setup does not allow for krypton beam imaging. The base-line is the loading rate with only MOT, ZSL and booster.

For both types of vector, the next steps are the individual addition of both collimator axes[1] (first 'COL H' – horizontal, then the other 'COL V' – vertical) and then the inclusion of both ('COL'). Finally, both MOL axes are added, and the enhancement between both COL axes and the COL together with the MOL is noted.

For a sample with large krypton amount and therefore high ^{85}Kr count rates the vector was even extracted from single atom detection. To achieve good comparison, the same sample was also used to measure a ^{83}Kr loading rate vector. Table 6.1 shows the results of these two measurements and compares them to typical enhancement factors from the ArTTA machine.

	flux	COL H	COL V	COL	COL+MOL
^{85}Kr count rate [a/h]	52 ± 5	700 ± 46	1030 ± 55	4460 ± 160	7300 ± 150
factor	1	14 ± 2	20 ± 2	86 ± 9	1.6 ± 0.1
^{83}Kr loading rate [a.u]	18 ± 1	54 ± 10	77 ± 12	290 ± 60	330 ± 60
factor	1	3.0 ± 0.6	4.3 ± 0.7	16 ± 3	1.1 ± 0.3
typical ArTTA factor	1	10	10	100	1.5

Table 6.1: Measured ^{85}Kr count rates and ^{83}Kr loading rates for a krypton to argon 1:1 mixture. Enhancement factors of atom optical tools were calculated by referencing to the 'flux' value, which is the bare signal without any enhancement. The final factor 'COL+MOL' is referenced to 'COL'. For the ^{83}Kr loading rates the repumpers were switched off.

In order to achieve a high count rate, a 1:1 krypton to argon mixture was used. Unfortunately, the amount of ^{83}Kr became so high that the loading rate could not be directly measured, since the MOT would saturate too fast. Therefore the repumpers needed to be left out for the loading rates shown here. The discrepancy in enhancement for absolute numbers between the factors for loading and count rate is caused by this lack of repumpers in the collimator. Due to the hyperfine structure of both ^{85}Kr and ^{83}Kr, the repumpers directly behind the source are especially important to pump the atoms from other hyperfine states into the desired ground state $F = 13/2$. Due to its number of substates (see the left side of figure 2.4) 28 %

---

[1]The collimator axes are the two spatial directions from which the atoms are cooled by the collimator laser beams. One of them is referred to as the vertical axes, COL V. The other one is perpendicular to COL V and therefore termed COL H.

of the atoms are in $F = 13/2$ in the beginning even without repumpers. The two repumper sidebands also include $F = 11/2$ and $F = 9/2$ into the cooling and therefore increase this fraction to 72 %. These two numbers indicate an increase of atoms in the cooling ground state by a factor of 2.6 with the repumping sidebands. The differences between the measured enhancement factors for loading rate and count rate are ∼5 which results from the lack of repumpers in not only the COL but also the MOT. The absence of repumping sidebands in the MOT reduces the fluorescence and therefore the ^{83}Kr loading rate.

The measured increase from 'COL V' to 'COL' is in both measurements ∼ 4, also the 'COL+MOL' factor is comparable. This suggests that the two methods might not be comparable in absolute numbers but in relative ones. Both are reliable methods to measure the performance of the KrypTTA machine. Also typical vectors for the argon ArTTA are comparable to which was measured with the ^{85}Kr count rate as can be seen in the last row of table 6.1. This shows that the atom optical tools are well adjusted also for krypton and can be further used to enhance the count rate of ^{85}Kr.

6.1.2 Zeeman slower optimization

To optimize the Zeeman slower detuning and magnetic field, the influence of both on the flux of the abundant ^{83}Kr is examined. Since the krypton atoms are cooled and trapped inside the ArTTA apparatus, the setup itself may not be altered and the magnetic field coils may only be changed in current.

This was done only for the ZSL coil, because the MOT magnetic field of 18 G/cm [19] is also suitable for trapping and detecting ^{83}Kr and ^{85}Kr. This is convenient considering the feasibility of D-ATTA measurements of radio-argon and radio-krypton. However, changing the ZSL coil alone is unfortunately not sufficient. The ArTTA setup features an additional coil between ZSL and MOT, which is the so-called compensation coil. It is used to produce a steep decay of the ZSL magnetic field to reduce residual fields in the MOT. As the ZSL coil current is varied the compensation coil current needs to be adjusted as well to hold the point of zero magnetic field, which defines the MOT center, at the same position.

As previously discussed in section 2.5, the Zeeman slower current needs to be shifted to lower values because of the higher mass of krypton compared to argon. Otherwise krypton might be lost from the cooling cycle inside the slower, since it can not follow the constant deceleration caused by the high magnetic field gradient.

The ^{83}Kr MOT loading rate was determined by continuously detecting the fluorescence of the atoms. Prior to the measurement, a complete loading curve was obtained to find the regime of linear fluorescence increase. This linearity allows to use the detected fluorescence as a measure for the MOT loading rate.

The measurement was conducted with a sample of a krypton to argon mixture of 1:10. First the ZSL detuning was fixed to a value with the offset lock (see laser
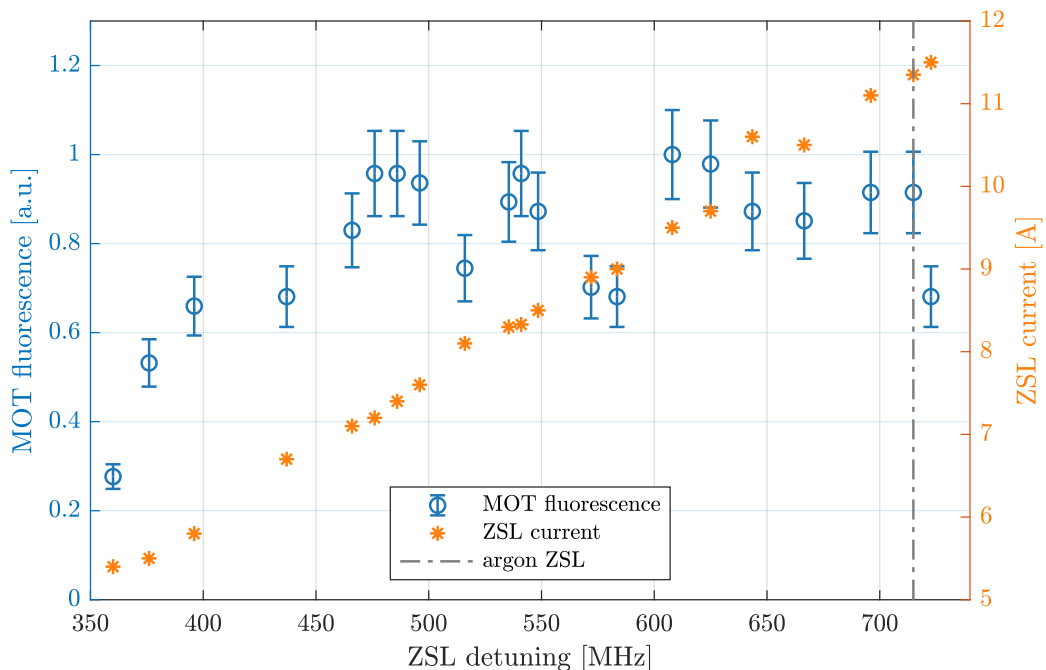
Figure 6.1: Measured MOT loading rate versus ZSL detuning (blue circles). The fluorescence of ^{83}Kr atoms in a 1:10 krypton to argon mixture was measured after 2 ms loading time. The magnetic field of the slower and the compensation coil were tuned to achieve a maximal fluorescence. Orange asterisks show the set ZSL current. The fluorescence error is ten percent due to signal fluctuations. The typical argon ZSL detuning is shown as dashed, gray line.

setup in figure 4.2), then the ZSL and compensation coil magnetic field were tuned until the loading rate reached an optimum. This maximum loading rate, as well as the detuning and ZSL magnetic field were noted and are displayed in figure 6.1.

The figure shows the measured fluorescence versus ZSL detuning as circles with an uncertainty of 10 %. This error is caused by fluctuations of the fluorescence measured by the camera (*Hamamatsu C8484-03G02*). The fluctuations of detuning due to the lock were on the order of 0.1 MHz and therefore negligible. The orange asterisks represent the optimal Zeeman slower coil current for the corresponding detuning.

The fluorescence signals show a broad maximum around 450 to 700 MHz, which is supported by a calculated fudge factor ξ of 0.25 to 0.55 in this region. For higher detuning, the fudge factor increases and the loading rate decreases. At this point, some atoms are lost from the cooling cycle and can not be captured in the MOT

due to their high remaining longitudinal velocity. Lower detunings result in a lower loading rate as these detunings are not sufficient to address the fastest krypton atoms in the beginning of the slower. These are then not cooled at all and can therefore not be trapped.

The optimized ZSL current versus detuning can be compared to the calculations of figure 2.7. The calculated ZSL current shown in this figure is slightly higher than the measured one in figure 6.1. This could be a result of an underestimated MOT capture velocity and therefore underestimated final velocity of the slower. For the calculations leading to figure 2.7, the final velocity for krypton was set to $v_{f,Kr} = 22\,\mathrm{m/s}$. That value is based on the final velocity for argon $v_{f,Ar} = 49\,\mathrm{m/s}$ calculated from the slower magnetic field at the end and laser detuning. In order to obtain $v_{f,Kr} = 22\,\mathrm{m/s}$ the lower maximal deceleration due to the higher mass was taken into account and plugged into equation 2.46. However, the magnetic field to detuning relation shown in figure 6.1 suggests a final velocity of $v_{f,Kr} = 35\,\mathrm{m/s}$. Adapting the calculated relation of figure 2.7 to this velocity matches it to the observed relation in figure 6.1. The capture velocity of the MOT in combination with the booster matches the final slower velocity, $v_f = v_c$. In the case of $v_{f,Kr} = 35\,\mathrm{m/s}$ this means that $v_{c,Ar} = 80\,\mathrm{m/s}$, which is also in the range of simulated capture velocities found in [50] and [51] but slightly higher than the value expected from the ZSL magnetic field and detuning.

The gray dashed line shows the detuning used for slowing argon. Future applications might aim to capture argon and krypton in the same machine simultaneously, which is a further development of the D-ATTA experiment which was already demonstrated as a consecutive measurement of the two tracers in section 4.6. For simultaneous D-ATTA the ZSL detuning and corresponding coil current will be set to the optimum for ^{39}Ar detection. This is due to the fact that the count rate is significantly lower for ^{39}Ar than for ^{85}Kr and the machine needs to run on the ^{39}Ar optimum at all times. In order to show the feasibility of this measurement, the ^{85}Kr count rate was determined for both the optimum argon and krypton ZSL parameters. The results of this are shown in table 6.2[2].

	^{85}Kr ZSL	^{39}Ar ZSL
count rate [a/h]	888 ± 33	333 ± 17

Table 6.2: Measured ^{85}Kr count rates for different ZSL settings. The measurement on the left was conducted at the optimal ZSL current for ^{85}Kr detection, whereas it was set to the ^{39}Ar optimum for the measurement on the right.

---

[2]These are the measured count rates. No Melonenschnaps was involved during any measurement.

The measurements were conducted with a krypton to argon mixture of 1:10. If the ZSL current is set to the argon optimum, the ^{85}Kr count rate decreases by a factor of 2.7 which puts a simultaneous D-ATTA measurement within reach since radio-krypton dating would be feasible even at these lowered count rates. For the measurements conducted in this thesis however, the ZSL detuning and current were set to the krypton optimum at -510 MHz and 8.3 A, respectively.

6.2 Krypton sample requirements

One challenge in dating with ^{85}Kr is the small krypton amount in environmental samples. The goal is to successfully date a krypton sample extracted from 10 L of water, which contains only $\sim 1\,\mu$L of krypton [75]. In order to achieve the necessary source pressure for sustaining a plasma discharge, this microscopic krypton amount needs to be mixed with another gas to reach a sample volume of $\geq 100\,\mu$L with the new vacuum setup discussed in section 4.4. In order to enable D-ATTA dating of ^{85}Kr and ^{39}Ar, the krypton sample is mixed with argon gas. This section shows measured count rates for different source pressures and argon admixtures, so that the ideal amount of sample volume and argon admixture can be extracted from the interpretation of these results.

6.2.1 Dependency of ^{85}Kr count rate on plasma source pressure

First, the exact gas amount for an optimal detection of ^{85}Kr needs to be determined before the admixture for future environmental samples is fixed. The volume should be as small as possible whilst still ensuring a stable and high count rate. That way, the mixed amount of argon can be minimized.

Figure 6.2 shows two experimental runs for which the pressure of the source was varied while counting ^{85}Kr atoms. One can see that below 4.5×10^{-6} mbar the count rate decreases, whereas above this pressure up to 8×10^{-6} mbar it reveals a broad maximum. A pressure of $p_s = 4.6 \times 10^{-6}$ mbar corresponds to a sample volume of $V = 103(2)\,\mu$L. In order to shift the source pressure to a more stable regime for the measurement of artificial samples, their gas volume was set slightly higher to $V \approx 110\,\mu$L, resulting in $p_s \approx 5.3 \times 10^{-6}$ mbar. Strictly speaking, this volume would require a mixture of krypton to argon of 1:110 to limit the amount of krypton per measurement to exactly $1\,\mu$L. However, for the measurements in this thesis, especially the samples of varying ^{85}Kr activity, the admixture was fixed to 1:100, neglecting the 10% difference. The impact of various mixing ratios on the count rate will be shown in the next section.
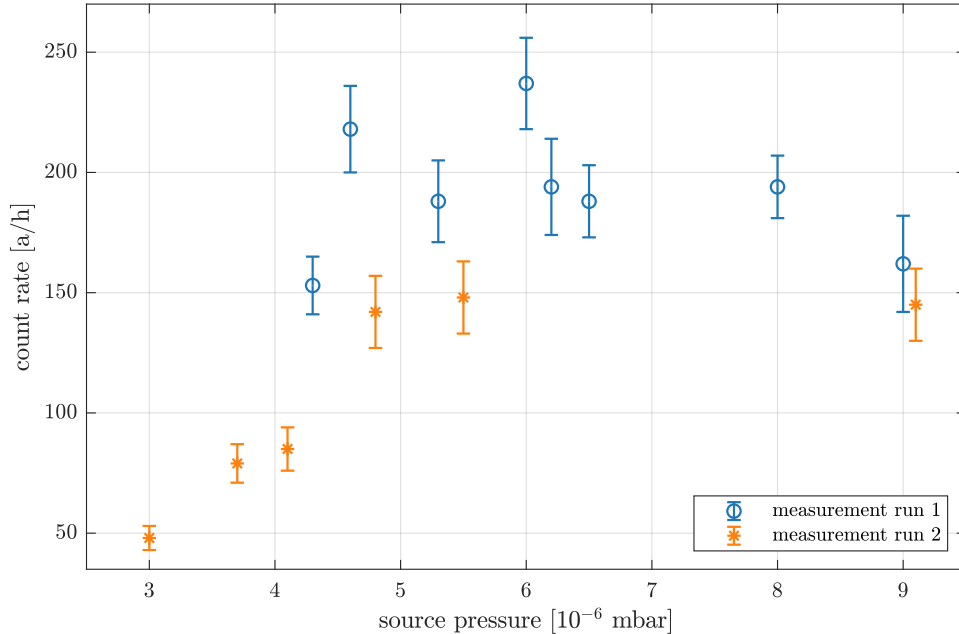
Figure 6.2: Measured ^{85}Kr count rate versus source pressure. Both data sets of measurement run 1 (blue circles) and run 2 (orange asterisks) were taken three days apart, with the only difference between them being the cooling of the sample container with liquid nitrogen. This cooling can cause fractionation effects and lead to a lower krypton content. For run 1, no cooling was employed, resulting in slightly higher count rates. The measurements were taken with a 1:42 krypton to argon admixture and are not corrected for contamination. The lowest volume for this measurement was $77\,\mu$L, the largest $240\,\mu$L.

6.2.2 ^{85}Kr count rate of various krypton to argon mixtures

In order to study the effect of argon admixture to a krypton sample, the dependency of the ^{85}Kr count rate on the argon amount was studied. The admixture is a necessary tool for preparing an environmental sample with $1\,\mu$L krypton to be measured with the KrypTTA machine. In the previous chapter, the connection between count rate and pressure was studied, which set the required sample volume to $V \geq 100\,\mu$L.

One might think, if the relative krypton amount in a sample decreases, the ^{85}Kr count rate decreases accordingly, which was also observed in [97]. However, there are experiments that show an increase of meta-stable density caused by carrier gas due to enhancement of the electron density in the plasma [98]. Measuring the ^{85}Kr count rate for rising argon admixtures will reveal either its decrease or increase and

lead to the optimal mixed argon amount.

Figure 6.3 shows the measured count rates for various mixtures corrected for
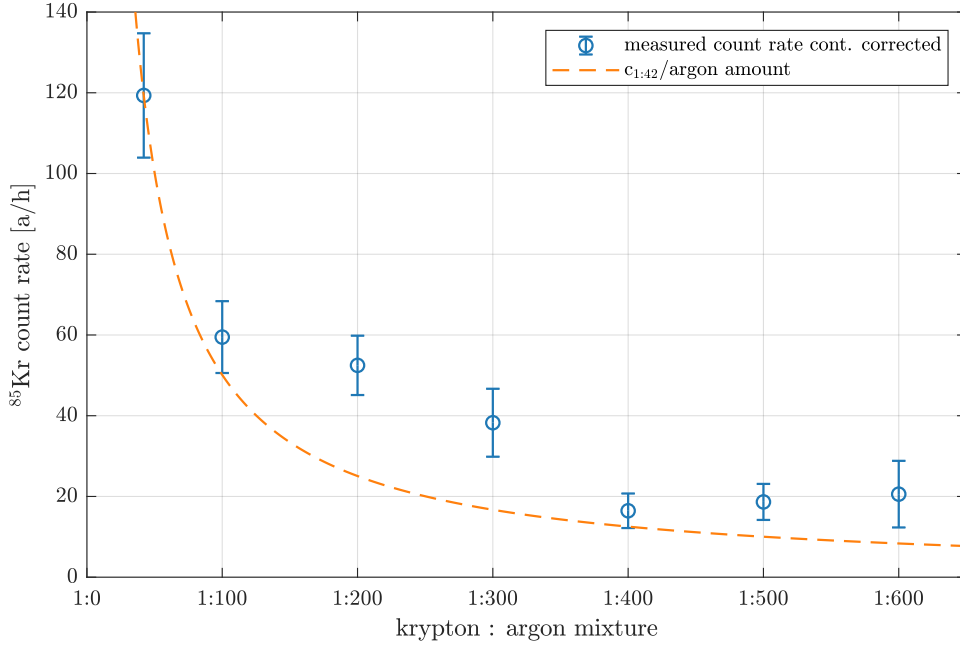
Figure 6.3: Contamination corrected ^{85}Kr count rate for different krypton to argon mixtures (blue circles). The reduction of count rate for higher argon admixture is clearly visible. The orange dashed line shows the count rate estimated from the krypton amount in the sample using the count rate of the 1:42 sample as a reference.

contamination. This correction is essential, since the contamination atoms otherwise disturb the measurement, as already extensively discussed in the previous chapter. In this specific measurement, the count rate is the used result instead of the super-ratio S. The loading rate is also affected by the argon mixture because the ^{83}Kr amount varies and can therefore not be used as a reference in the super-ratio S.

The contamination contributes to the number of measured atoms N_m with two different processes, which were extensively discussed in the previous chapter. Extending equation 5.4 to include the sample count rate c_s then yields

$$N_m = \frac{\zeta}{V_s}c_p t + \frac{\eta}{V_s}c_{qc}t^2 + c_s t. \tag{6.1}$$

Since this experiment was conducted under similar conditions as the measurements of different artificial ^{85}Kr activities, which will be discussed in the following chapter,

the contamination coefficients ζ and η extracted from that run will serve for the subtraction of the contamination in this section. This assumption is valid, because the vacuum setup was not changed and no highly enriched samples were used between these two experiments, so that the contamination coefficients should be the same. Also, they are normalized by the count rate so that changes in the reference count rate are not an issue.

Looking at figure 6.3 one can observe that the count rate decreases for a smaller relative krypton amount, but also that it is still higher than what is expected by considering a decrease only due to krypton amount. The highest count rate c_{ref} comes from a 1:42 krypton to argon mixture. The dashed line in figure 6.3 is calculated via

$$c_{s,theo} = c_{ref} \frac{\text{ar amount ref}}{\text{ar amount sample}} = c_{ref} \frac{42}{\text{ar amount sample}} \tag{6.2}$$

with the argon amount of the sample 100, 200, ... and 600. The model of decreasing count rate with smaller relative krypton amount seems to hold true here, although the sample count rates are all slightly shifted to higher values. This could be an indicator for remaining krypton contamination. This is most likely caused by the 1:42 sample for this measurement run which is of higher activity than the 1:100 mixture of the artificial samples. However, figure 6.3 provides the desired restriction on argon admixture: the less argon, the better. Therefore in the following, all measured samples are prepared as a 1:100 mixture with $\sim 100\,\mu\text{L}$ sample size corresponding to the desired $10\,\text{L}$ water volume.

6.3 Measurement of artificial samples

The final step is the measurement of the artificial samples. These were produced as a 1:100 krypton to argon mixture using $\sim 100\,\mu\text{L}$ gas to resemble a sample extracted from $10\,\text{L}$ of water. The goal is to demonstrate ^{85}Kr dating with a graph similar to figure 5.1 for ^{39}Ar.

The krypton part of the samples was prepared by Yannis Arck as a mixture of dead and atmospheric krypton with an activity of $0\,\text{pm}$, $10\,\text{pm}$, $33\,\text{pm}$, $66\,\text{pm}$, and $100\,\text{pm}$. The $100\,\text{pm}$ sample (purely atmospheric krypton) was also used as a reference. A reference of higher krypton admixture would have shortened the measurement time, but also increased the contamination. In this setup, the reference was measured for $2\,\text{h}$, whereas the samples were each measured for $8\,\text{h}$, leaving $1\,\text{h}$ of cleaning time between each measurements to reach a measurement cycle of $12\,\text{h}$. The measurement procedure is schematically shown in figure 5.6.

Reference measurements

The analysis of the measurement run for the artificial samples does not begin with the samples itself but with the reference data. Going back to the last chapter, equation 5.11 gives the corrected reference count rate c_{ref} and is also shown again here

$$c_{ref} = \left(N_m - \frac{\zeta}{V_{ref}} c_p t \right) t^{-1}. \qquad \text{(5.11 revisited)}$$

As ζ is already determined in equation 5.6 and N_m and V_{ref} are measured for each reference data set, the missing piece is the previous count rate c_p. These were calculated for each measurement individually as the not contamination corrected bare measured atom number over time. With this, equation 5.11 can be evaluated.

All contamination corrected reference count rates are shown on the left side of figure 6.4. The right side shows these count rates divided by the ^{83}Kr loading rate. The used bare data is displayed in the appendix A.

The error was calculated using error propagation, the largest contribution being
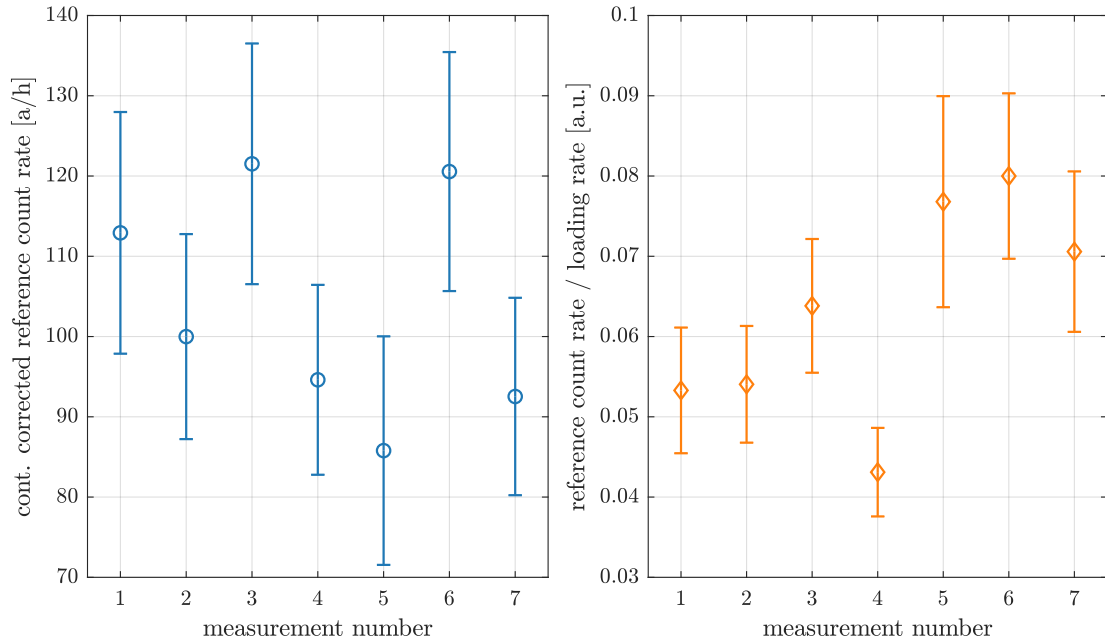
Figure 6.4: Left side: ^{85}Kr count rate of the reference measurements with contamination subtracted according to equation 5.11. Right side: ^{85}Kr count rate divided by ^{83}Kr loading rate of the same reference measurement. The measurement number is given chronologically.

the Poisson counting error of N_m. The count rates are not varying strongly. The

right side of figure 6.4 shows the reference count rates divided by the detected ^{83}Kr loading rate.

Artificial measurements with varying ^{85}Kr activity

Finally, the measured samples can be corrected for contamination to reveal whether a performance graph similar to 5.1 for ArTTA can also be achieved with KrypTTA. The previous chapter extensively discussed the analysis of contamination and gave with equation 5.9 the mathematical tool for determining the real super-ratio S of each sample. This equation is shown again here

$$S = \left(S_m - \frac{\zeta}{V_s} - \frac{\eta t}{V_s} \right) \left(1 - \frac{\zeta}{V_s} - \frac{\eta t}{V_s} t \right)^{-1}. \qquad \text{(5.9 revisited)}$$

The previously calculated reference count rates are necessary here, whereas c_{ref} was computed as the mean of the two reference samples measured before and after the sample. The results of the calculated super-ratios S are presented in figure 6.5.

The contamination corrected results show the desired linearity between expected super-ratio from the defined ^{85}Kr concentration and the measured one. The uncertainties are mainly dominated by the Poisson statistical error of reference and sample, however, also the errors for ζ, η, and V_s are included. The results feature a linear increase with higher ^{85}Kr amount but appear to be lower in super-ratio than expected. This discrepancy can be caused by over-estimating the contamination coefficients extracted from fitting the measured atom number in a dead sample. The ^{85}Kr counting efficiency might have been slightly higher for this contamination measurement, resulting in larger values for ζ and η. Measuring more dead krypton samples and using those for computing the coefficients reduces possible drifting effects.

Figure 6.5 is the first demonstration of radio-krypton analysis with $1\,\mu$L krypton gas. This gas amount corresponds to a $10\,$L water sample which also contains $\sim 4\,$mL of argon. The D-ATTA setup is therefore capable of ^{39}Ar dating and also ^{85}Kr detection to the required limit in the same sample. To transform D-ATTA into a routine dating machine, the setup needs to undergo some adjustments which will be briefly introduced in the final chapter.
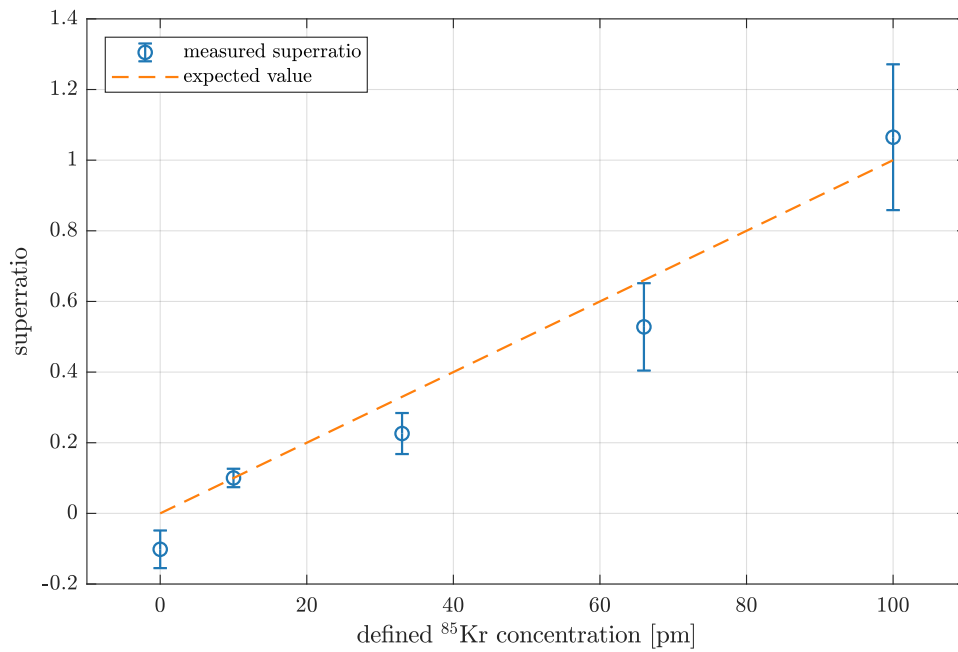
Figure 6.5: Measured and contamination corrected sample super-ratios S versus super-ratio expected from the defined ^{85}Kr concentration. The dashed line is a guide to the eye and represents the perfect agreement of both. The graph is comparable to the performance graph for the ArTTA machine shown in figure 5.1.

7 Conclusion and outlook

The work presented in this thesis can be separated into two main parts that both contribute to the further development of the ATTA activity in Heidelberg. The first aspect is the development of the second ArTTA facility inside a laboratory container. Chapter 3 presented the design, realization, and employment of a setup for single atom counting resulting in the first ^{39}Ar signal in the container. Additionally, devices measuring the machine performance were designed and built in to enable efficient optimization and monitoring. These developments lay the foundation for routine ^{39}Ar dating in the container.

The other goal of this thesis was the realization of a ^{85}Kr dating setup and its integration into the existing original ArTTA machine. Enabling the detection of two tracers in this D-ATTA experiment elevates the existing ArTTA machine into a more versatile and powerful dating apparatus. The ability to investigate both the ^{85}Kr and ^{39}Ar concentration within a single sample and a short time interval allows for a more thorough tracer study of the environmental sample. In chapter 4, the first successful D-ATTA measurement was shown, yielding count rates that are sufficient for dating of both isotopes. After modifying the vacuum system to handle smaller sample sizes, radio-krypton analysis from $1\,\mu$L krypton gas was demonstrated. The measured sample was a mixture of krypton and argon gas with a ratio 1:100 showing the feasibility of ^{85}Kr dating from $1\,\mu$L krypton gas and an ^{39}Ar dating measurement in the same sample. The volume restrictions are set to match a water sample size of $10\,$L which corresponds to the sampling volume of a standard Niskin bottle.

Finally, the ^{85}Kr concentration in artificially produced samples of varying activity was measured. As is presented in chapter 6, $1\,\mu$L krypton gas samples were used to show the feasibility of radio-krypton dating from $10\,$L of water. Subtracting the contamination from the measured data yielded the expected linear behavior between known sample concentration and obtained super-ratio S, as shown in figure 6.5. An atmospheric ^{85}Kr count rate of $100\,$a/h was achieved. The krypton measurements presented in this thesis are a benchmark for future ^{85}Kr dating activity in Heidelberg.

This final chapter concludes by revisiting the experimental setup and proposing performance-increasing modifications. It presents future improvements on the D-ATTA setup and the dating machine in the container.

7.1 D-ATTA setup improvements

D-ATTA laser system improvements

The laser setup for the first detection of ^{85}Kr was designed to offer flexible ZSL laser beam detuning. Due to this, a second laser was introduced into the system which could be variably locked relative to the master with an offset lock [83]. This technique allowed to scan the laser frequency to find the optimum ZSL detuning of $-510\,$MHz and corresponding ZSL coil current of $8\,$A.
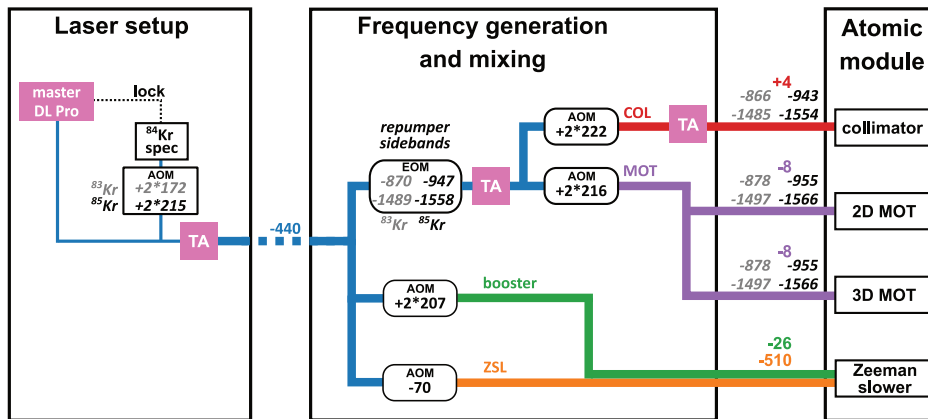

Figure 7.1: Schematic of the frequency generation in the krypton laser setup. Though the flexibility of the Zeeman slower frequency is lost (see figure 4.2), only one master laser is required. The Zeeman slower detuning is instead generated by a single pass AOM. The other laser frequencies are obtained in the same way as previously demonstrated and verified.

Figure 7.1 shows the generation of this ZSL frequency with an additional AOM path for the master laser. This setup fixes the detuning to the optimum value of $-510\,$MHz and renders the second laser obsolete. The result is a more compact and reliable laser system for detection of ^{83}Kr and ^{85}Kr, easily achieved by small modifications on the existing one.

Radio-krypton dating with ^{81}Kr

This thesis demonstrated the detection of ^{83}Kr and ^{85}Kr. However, the extremely long-lived radio-isotope ^{81}Kr is also of high interest in environmental physics, where it serves as a tracer for very old groundwater [43] or ice [44]. Figure 7.2 shows the krypton isotopes and their frequency offset from the most abundant isotope ^{84}Kr. In order to detect ^{81}Kr, the laser lock needs to be modified.
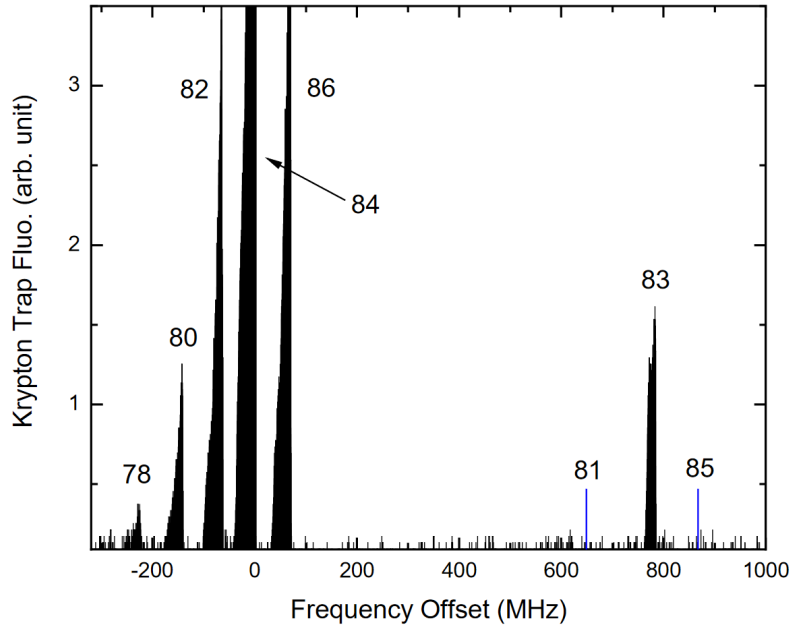
Figure 7.2: Krypton isotopes and their frequency offset from the most abundant isotope ^{84}Kr. The figure is a fluorescence measurement obtained by scanning the frequency of the cooling transition. Each peak corresponds to a krypton isotope where the height of the fluorescence gives the relative abundance of this isotope. Due to their low natural abundance, the radio-isotopes ^{81}Kr and ^{85}Kr cause no fluorescence peak. Their frequency offset is still shown. Figure taken from [53].

In this thesis frequency-variable locking is produced with an AOM (*Gooch & Housego, 3200-124*), which is used to shift the laser frequency before entering the spectroscopy cell (see figure 7.1 and 4.2). This is only applicable because the frequency difference of 87 MHz between ^{83}Kr and ^{85}Kr is not larger than the bandwidth of the AOM.

isotope	cooling transition frequency relative to ^{84}Kr [MHz]	half-life $T_{1/2}$ [a]
^{81}Kr	656	2.12×10^5
^{83}Kr	783	stable
^{85}Kr	870	10.8

Table 7.1: Overview of the frequency shifts of the to-be-detected isotopes relative to the most abundant isotope ^{84}Kr.

However, the ^{81}Kr cooling transition is 214 MHz detuned from the transition in ^{85}Kr, which exceeds the bandwidth of a double-pass AOM. Therefore, the detection

of ^{81}Kr is not easily integrated into the laser setup shown in figure 7.1, but can instead be realized with an additional laser and an offset lock. This technique is also used at the ArTTA apparatus for locking onto the argon isotopes ^{36}Ar, ^{38}Ar, ^{40}Ar, and ^{39}Ar.

The master laser currently in use would remain locked to the cooling transition in ^{84}Kr at all times and is overlapped with a second laser, the slave. The offset lock [83] is used to fix the frequency difference between these two lasers. With this setup, the slave laser frequency can be variably locked within a span of $\sim 1\,\mathrm{GHz}$ which allows to tune it to the cooling transition in ^{83}Kr, ^{85}Kr, and ^{81}Kr. In the setup as shown in figure 7.1, the slave laser would then produce the beam with a detuning of $-440\,\mathrm{MHz}$, which would later be used to generate all other necessary laser frequencies.

Though all repumping frequencies also need to be adjusted to ^{81}Kr, this can easily be achieved by changing the frequencies on the EOM. The required detunings (see table 2.4) can be produced by the already in-use voltage-controlled oscillators that apply the radio-frequencies onto the EOM.

Increase in radio-krypton count rate

Due to the extremely high count rate of ^{85}Kr the KrypTTA setup was never fully optimized to achieve the highest possible count rate. If the isotope ^{81}Kr is added to the portfolio, this isotope's count rate will most likely be 40 times lower than for ^{85}Kr, considering its lower relative abundance. This would result in a count rate of $\sim 3\,\mathrm{a/h}$ for $1\,\mu\mathrm{L}$ krypton samples, which is comparable to ^{39}Ar. For these small count rates, measuring at the optimum achievable efficiency is crucial.

The collimator detuning for krypton was equal to the one used for ^{39}Ar dating and not optimized for ^{85}Kr in this thesis. Additionally, the alignment of the collimator mirrors inside the vacuum chamber was not adjusted after switching from argon to krypton detection. The collimator still caused a satisfying enhancement in ^{83}Kr loading rate and ^{85}Kr count rate (shown in table 6.1) and was therefore not further investigated. The detuning is defined by the transverse velocity of the atoms and angle of incidence of the collimator laser beam, which together cancel the Doppler shift. The transverse velocity is expected to be lower for krypton since the temperature of the plasma is the same but krypton is more than twice as heavy as argon. The optimum can be found by scanning the AOM frequency while monitoring the ^{83}Kr loading rate.

Source monitoring via quench transition

Similarly as in argon, the quench transition in krypton can be utilized to monitor the source efficiency during a measurement. This requires an additional laser, locked on this transition. Furthermore, the quench laser light needs to be led to the vacuum

chamber, preferably in the fiber used for the same purpose in argon so that the same optics are used. This can be achieved by flip-mirrors, similar to the setup shown in figure 4.4. However, the ^{84}Kr atoms emit a 877 nm photon when de-exciting to the ground state (see figure 2.5), which is blocked by the band-pass filter before the detection diode. For comparison, ^{40}Ar emits a 843 nm photon.

As the krypton samples are mixed with a high amount of argon, the quench transition in ^{40}Ar can be utilized for source monitoring. Typically, the mixture is 1:100 Kr:Ar to achieve a krypton volume of $1\,\mu$L gas. This small krypton amount will not result in a detectable signal of de-excitation photons. Therefore, detecting the quench transition in ^{40}Ar is the only option for continuous source monitoring. The generation of meta-stable argon underlies the same changes as krypton making the monitoring via ^{40}Ar-quench feasible to detect mode-jumps or performance degradation of the plasma source.

Source and fore-vacuum modifications

The fastest and most efficient way to enhance the count rate of krypton isotopes is to reduce the required sample size, lowering the required argon dilution. The fore-vacuum of the D-ATTA machine, displayed in figure 4.9, contains many hoses and crosses of large cross-section and length which can be replaced by more compact elements to reduce the volume.

However, as the sample size decreases, the contamination has a relatively larger effect. In particular, the freezing of sample gas on the cold parts of the source was an issue in this thesis and needs to be prevented in the next measurements of krypton. The ability to employ a more efficient flushing system similar to the existing krypton ATTA machine at the ANL [53] can be achieved by discarding the liquid nitrogen cooling completely, in which case the indium wire around the source tube also needs to be removed. This would result in a lower count rate by a factor of approx. four but reduce the contamination [94].

Another option is the design of a new source, which offers the possibility of liquid nitrogen cooling without the creation of cold areas in the vacuum chamber on which krypton can freeze. A new design was realized and is currently built in the container ArTTA machine. The source performance and other information on the design will soon be published in the dissertation of Julian Robertz.

7.2 Second ArTTA facility

This thesis showed the first detection of the rare ^{39}Ar in the laboratory container. The modular and fiber-coupled design proved to be very flexible and robust, but when it comes to laser power, the fiber coupling is an issue. The TA diodes currently used in the container to generate the necessary powers typically operate at a high

($\geq 2\,$A) current, which reduces their lifetime to two years. Mounting the TA chips on separate blocks that can quickly be replaced has simplified the chip replacement procedure.

Using EOMs in the laser setup to produce the repumping sidebands for ^{39}Ar would make the AOM paths for the repumper frequencies obsolete and therefore also reduce the number of TA diodes from five to four. Additionally, the slave 2 laser and corresponding offset lock could be removed from the laser setup.

The container machine continues to grow: the fore-vacuum is already built up and is used to measure the typical ten-times ^{39}Ar enriched reference sample. The count rate has increased steadily and will soon reach a rate feasible for radio-argon dating.

A Appendix

MOT objective design

The design of the MOT objective was extensively discussed in the thesis' subsection 3.5.2. Here, all part numbers for the lenses and an exact setup of the objective are presented.

The upper part of table A.1 displays the built-in lenses of the objective in the original ATTA lab, which was designed and realized in [51]. Since most of these were no longer available for another setup in the container lab, a new setup was designed and realized using standard lenses from *Thorlabs* which are shown in the lower part of table A.1. The first two lenses needed to be ground down to 34 mm diameter to fit the space restrictions in the vacuum. These were custom made in a higher quantity by *Melles Griot* for the original objective, so the spare ones were used in the container.

original ATTA			
position	focal length [mm]	used lens	Company
1	100	MENP-50.0-10.3-100.0-C-670-1064	*Melles Griot*
2	125	LPX-50.0-64.8-C-670-1064	"
3	100	LDX-50.0-102.3-C-670-1064	"
4	-100	LPK-50.0-51.9-C-670-1064	"
5	100	LPX-50.0-51.9-C-670-1064	"
6	100	MENP-50.0-10.3-100.0-C-670-1064	"
Container			
position	focal length [mm]	used lens	Company
1	100	MENP-50.0-10.3-100.0-C-670-1064	*Melles Griot*
2	125	LPX-50.0-64.8-C-670-1064	*Melles Griot*
3	100	LB1630-B	*Thorlabs*
4	-100	LC1093-B	"
5	99.7	LA1050-B	"
6	100	LE1076-B	"

Table A.1: Lenses used in the MOT objectives in the original ATTA lab (upper table) and the container lab (lower table).

Figure A.1 shows the position of the lenses in the objective and their relative
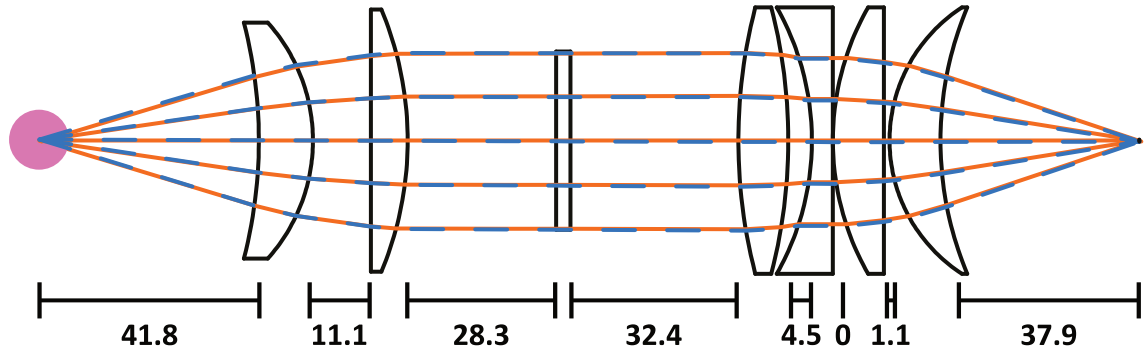
Figure A.1: Schematic of the MOT objective realized in the container. The distances between the lenses are given in mm and are measured from the lens' center. The pink sphere represents the atoms.

distances between each other. They are mounted on the vacuum side in a black-painted stainless-steel tube, on the other side of the vacuum window inside a 2 inch lens tube from *Thorlabs*.

Argon energy spectrum

In section 2.4.2 a part of the atomic level spectrum of argon was shown using the Racah notation. Figure A.2 displays are more extensive level scheme of this atom to offer a deeper understanding of the system. The figure uses the Paschen notation in which the state is denoted by $n'l_e$ where n' is the difference in principal quantum number between the highest body and the outer electron. The angular momentum l is the one of the outer electron and the number e sorts the states of equal $n'l$ by energy [99].

Measured krypton data

The results of the artificial measurement campaign for ^{85}Kr dating were presented in section 6.3, where the evaluation steps between the measured count rate and the resulting super-ratio S are also shown. Table A.2 shows the bare, non-contamination-corrected measured atom numbers and measurement times. It also contains the sample volumes and already evaluated ^{83}Kr loading rates.
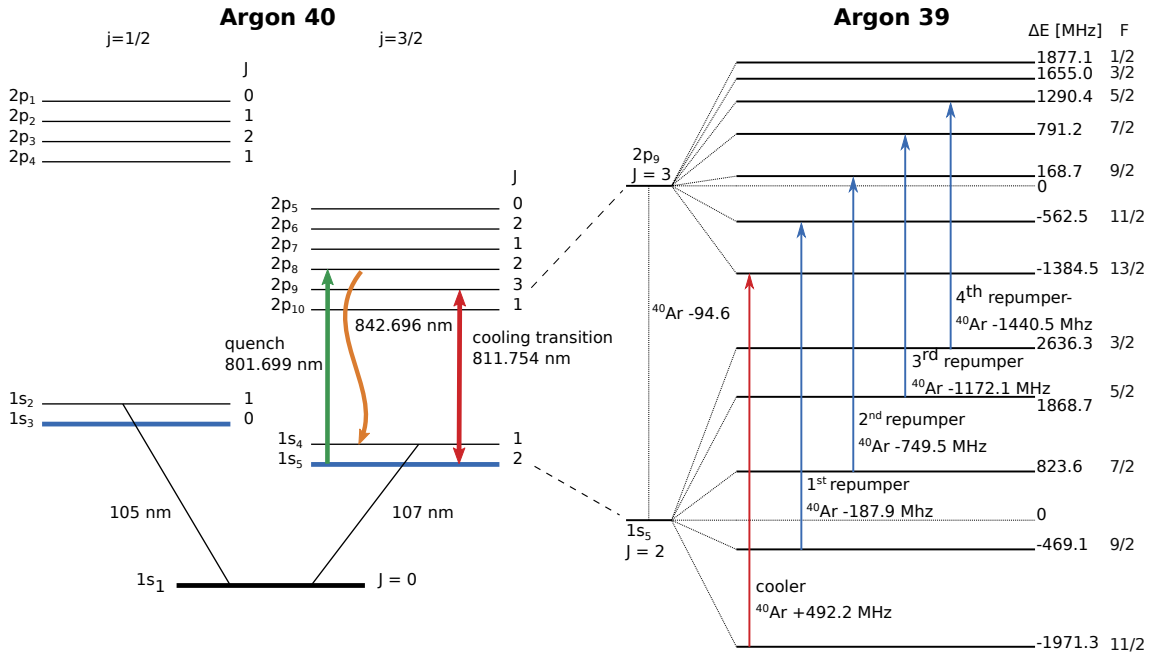
Figure A.2: Atomic energy level spectrum of even argon isotopes (left) and ^{39}Ar (right). The states are written in Paschen Notation. The highlighted, blue state is the meta-stable ground state for cooling which is 1s$_5$ in this notation. The excited state is denoted by 2p$_9$.

Hyperfine transition strengths

In the course of this thesis the transition strengths for the different sublevels involved in the transition from ground state to excited state were calculated. The strength of a transition $|g\rangle \rightarrow |e\rangle$ is given by the squared absolute of its dipole moment $|\mu_{eg}|^2$ which is normalized by its maximal value α [46]. Its value is obtained via

$$\frac{|\mu_{eg}|^2}{\alpha} = (2J_e + 1)(2F_g + 1)(2F_e + 1) \begin{Bmatrix} J_e & F_e & I \\ F_g & J_g & 1 \end{Bmatrix}^2 \begin{pmatrix} F_g & 1 & F_e \\ m_{Fg} & \Delta m & -m_{Fe} \end{pmatrix}^2 \quad \text{(A.1)}$$

with the braces being the Wigner 6j and Wigner 3j symbol [46]. The cooling transitions are $F_g = 11/2 \rightarrow F_e = 13/2$ in ^{39}Ar and $F_g = 13/2 \rightarrow F_e = 15/2$ in ^{83}Kr and ^{85}Kr. All states feature magnetic substates denoted by $m_F = -F, -F+1, ..., F$. The details regarding the isotopes and transitions are given in the subsections 2.4.3 and 2.4.2.

Tables A.3 and A.4 present the calculated transition strengths. Due to the symmetry of equation A.1 and limited page size only a part of the values are presented here. The figures A.3 and A.4 show all values in a schematic realization.

concentration ^{85}Kr [pm]	Measurement time [h]	Volume ± 3 [μL]	^{83}Kr loading rate [a.u.]	counted ^{85}Kr atoms
100	3.5	105	1530 ± 73	423
100	2.0	114	2119 ± 131	311
66	8.0	117	1856 ± 78	190
100	2.0	120	1850 ± 78	232
0	8.0	117	1826 ± 62	301
100	2.0	114	1904 ± 81	263
33	8.0	114	2352 ± 82	181
100	2.0	114	2195 ± 60	192
10	8.0	114	2098 ± 207	404
100	2.0	120	1117 ± 47	132
0	8.0	120	1800 ± 72	336
100	2.0	114	1507 ± 55	259
100	8.0	117	1531 ± 51	964
100	2.0	120	1311 ± 64	175

Table A.2: Measurement results from the artificial ^{85}Kr campaign.

$m_{F,g}$ \ $m_{F,e}$	-1/2	1/2	3/2	5/2	7/2	9/2	11/2	13/2
1/2	7/26	7/13	14/39	0	0	0	0	0
3/2	0	5/26	20/39	6/13	0	0	0	0
5/2	0	0	5/39	6/13	15/26	0	0	0
7/2	0	0	0	1/13	5/13	55/78	0	0
9/2	0	0	0	0	1/26	11/39	11/13	0
11/2	0	0	0	0	0	1/76	2/13	1

Table A.3: Transition strengths of the cooling transition $F_g = 11/2 \rightarrow F_e = 13/2$ in ^{39}Ar.

F$_e$=13/2

-13/2 -11/2 -9/2 -7/2 -5/2 -3/2 -1/2 1/2 3/2 5/2 7/2 9/2 11/2 13/2 **m$_F$**

1 11/13 55/78 15/26 6/13 14/39 7/26 5/26 5/39 1/13 1/26 1/76

2/13 11/39 5/13 6/13 20/39 7/13 7/13 20/39 6/13 5/13 11/39 2/13

1/78 1/26 1/13 5/39 5/26 7/26 14/39 6/13 15/26 55/78 11/13 1

-11/2 -9/2 -7/2 -5/2 -3/2 -1/2 1/2 3/2 5/2 7/2 9/2 11/2 **m$_F$**
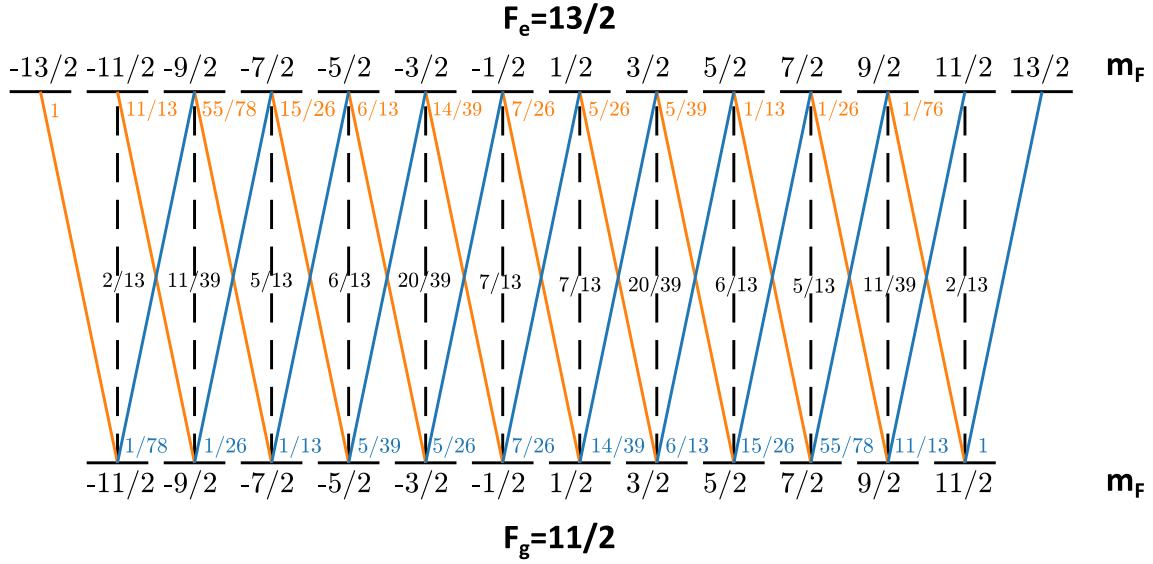
F$_g$=11/2

Figure A.3: Schematic showing transition strengths of the cooling transition $F_g = 11/2 \rightarrow F_e = 13/2$ in ^{39}Ar.

$m_{F,e}$ \\ $m_{F,g}$	-1/2	1/2	3/2	5/2	7/2	9/2	11/2	13/2	15/2
1/2	4/15	8/15	12/35	0	0	0	0	0	0
3/2	0	1/5	18/35	3/7	0	0	0	0	0
5/2	0	0	1/7	10/21	11/21	0	0	0	0
7/2	0	0	0	2/21	44/105	22/35	0	0	0
9/2	0	0	0	0	2/35	12/35	26/35	0	0
11/2	0	0	0	0	0	1/35	26/105	13/15	0
13/2	0	0	0	0	0	0	1/105	2/15	1

Table A.4: Transition strengths of the cooling transition $F_g = 13/2 \rightarrow F_e = 15/2$ in ^{83}Kr and ^{85}Kr.
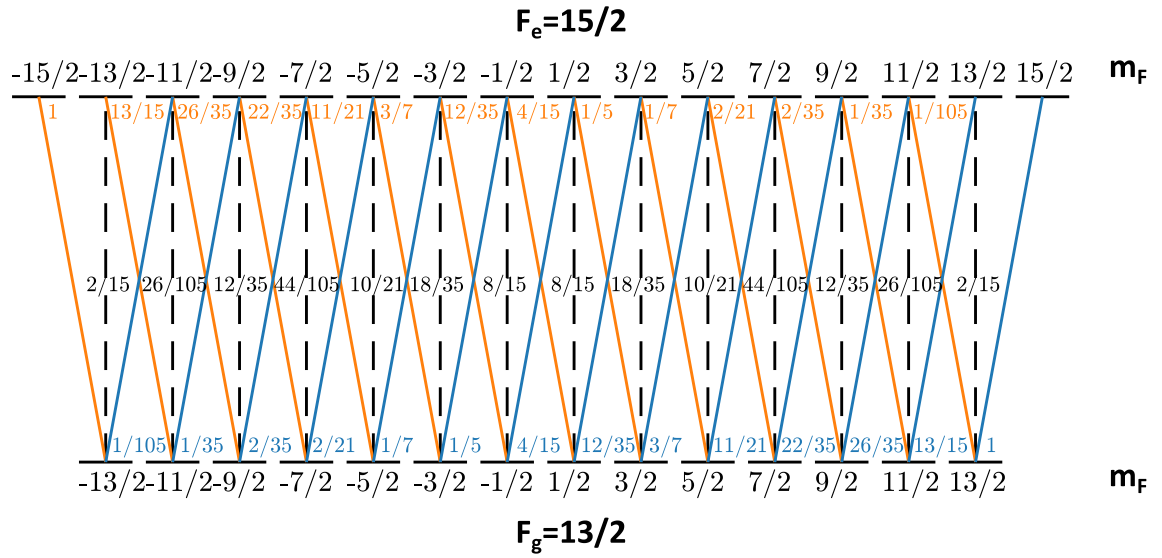
Figure A.4: Schematic showing transition strengths of the cooling transition $F_g = 13/2 \rightarrow F_e = 15/2$ in ^{83}Kr and ^{85}Kr.

List of own publications

[27]   Z. Feng, P. Bohleber, S. Ebser, L. Ringena, M. Schmidt, A. Kersting, P. Hopkins, H. Hoffmann, A. Fischer, W. Aeschbach, and M. K. Oberthaler. "Dating glacier ice of the last millennium by quantum technology". In: *Proceedings of the National Academy of Sciences* 116.18 (2019), pp. 8781–8786. ISSN: 0027-8424. DOI: 10.1073/pnas.1816468116. eprint: https://www.pnas.org/content/116/18/8781.full.pdf. URL: https://www.pnas.org/content/116/18/8781.

[28]   S. Ebser, A. Kersting, T. Stöven, Z. Feng, L. Ringena, Maximilian Schmidt, T. Tanhua, W. Aeschbach, and M.K. Oberthaler. "^{39}Ar dating with small samples provides new key constraints on ocean ventilation". In: *Nature Communications* 9.5046 (2018).

[80]   Z. Feng, S. Ebser, L. Ringena, F. Ritterbusch, and M. K. Oberthaler. "Bichromatic force on metastable argon for atom-trap trace analysis". In: *Phys. Rev. A* 96 (1 July 2017), p. 013424. DOI: 10.1103/PhysRevA.96.013424. URL: https://link.aps.org/doi/10.1103/PhysRevA.96.013424.

Bibliography

[1] H. Hertz. "Ueber einen Einfluss des ultravioletten Lichtes auf die electrische Entladung". In: *Annalen der Physik* 267.8 (1887), pp. 983–1000. DOI: `https://doi.org/10.1002/andp.18872670827`. eprint: `https://onlinelibrary.wiley.com/doi/pdf/10.1002/andp.18872670827`. URL: `https://onlinelibrary.wiley.com/doi/abs/10.1002/andp.18872670827`.

[2] A. Einstein. "Über einen die Erzeugung und Verwandlung des Lichtes betreffenden heuristischen Gesichtspunkt." In: *Annalen der Physik* 4.17 (1905), pp. 132–148.

[3] T.W. Hänsch and A.L. Schawlow. "Cooling of gases by laser radiation". In: *Optics Communications* 13.1 (1975), pp. 68–69. ISSN: 0030-4018. DOI: `https://doi.org/10.1016/0030-4018(75)90159-5`. URL: `https://www.sciencedirect.com/science/article/pii/0030401875901595`.

[4] William D. Phillips and Harold Metcalf. "Laser Deceleration of an Atomic Beam". In: *Phys. Rev. Lett.* 48 (9 Mar. 1982), pp. 596–599. DOI: `10.1103/PhysRevLett.48.596`. URL: `https://link.aps.org/doi/10.1103/PhysRevLett.48.596`.

[5] Steven Chu, L. Hollberg, J. E. Bjorkholm, Alex Cable, and A. Ashkin. "Three-dimensional viscous confinement and cooling of atoms by resonance radiation pressure". In: *Phys. Rev. Lett.* 55 (1 July 1985), pp. 48–51. DOI: `10.1103/PhysRevLett.55.48`. URL: `https://link.aps.org/doi/10.1103/PhysRevLett.55.48`.

[6] E. L. Raab, M. Prentiss, Alex Cable, Steven Chu, and D. E. Pritchard. "Trapping of Neutral Sodium Atoms with Radiation Pressure". In: *Phys. Rev. Lett.* 59 (23 Dec. 1987), pp. 2631–2634. DOI: `10.1103/PhysRevLett.59.2631`. URL: `https://link.aps.org/doi/10.1103/PhysRevLett.59.2631`.

[7] Steven Chu. *The manipulation of neutral particles*. Nobel lecture. 1998.

[8] William D. Phillips. *Laser cooling and trapping of neutral atoms*. Nobel lecture. 1998.

[9] K. Sengstock and W. Ertmer. "Laser manipulation of atoms". In: *Advances in Atomic, Molecular, and Optical Physics* 35 (1995), pp. 1–44.

[10] M. H. Anderson, J. R. Ensher, M. R. Matthews, C. E. Wieman, and E. A. Cornell. "Observation of Bose-Einstein Condensation in a Dilute Atomic Vapor". In: *Science* 269.5221 (1995), pp. 198–201. ISSN: 0036-8075. DOI: `10.1126/science.269.5221.198`. eprint: `https://science.sciencemag.org/content/269/5221/198.full.pdf`. URL: `https://science.sciencemag.org/content/269/5221/198`.

[11] C. Y. Chen, Y. M. Li, K. Bailey, T. P. O'Connor, L. Young, and Z.-T. Lu. "Ultrasensitive Isotope Trace Analyses with a Magneto-Optical Trap". In: *Science* 286.5442 (1999), pp. 1139–1141. ISSN: 0036-8075. DOI: `10.1126/science.286.5442.1139`. eprint: `https://science.sciencemag.org/content/286/5442/1139.full.pdf`. URL: `https://science.sciencemag.org/content/286/5442/1139`.

[12] W. Jiang, K. Bailey, Z.-T. Lu, P. Mueller, T.P. O'Connor, C.F. Cheng, S.M. Hu, R. Purtschert, N.C. Sturchio, Y.R. Sun, et al. "An atom counter for measuring ^{81}Kr and ^{85}Kr in environmental samples". In: *Geochimica et Cosmochimica Acta* 91 (2012), pp. 1–6.

[13] F. Ritterbusch, S. Ebser, J. Welte, T. Reichel, A. Kersting, R. Purtschert, W. Aeschbach-Hertig, and M.K. Oberthaler. "Groundwater dating with Atom Trap Trace Analysis of ^{39}Ar". In: *Geophysical Research Letters* 41.19 (2014), pp. 6758–6764.

[14] Philippe Collon, Walter Kutschera, and Zheng-Tian Lu. "Tracing Noble Gas Radionuclides in the Environment". In: *Annual Review of Nuclear and Particle Science* 54.1 (2004), pp. 39–67. DOI: `10.1146/annurev.nucl.53.041002.110622`.

[15] J.A. Corcho Alvarado, R. Purtschert, F. Barbecot, C. Chabault, J. Rueedi, V. Schneider, W. Aeschbach-Hertig, R. Kipfer, and H.H. Loosli. "Constraining the age distribution of highly mixed groundwater using 39Ar: A multiple environmental tracer (^{3}H/^{3}He, ^{85}Kr, ^{39}Ar, and ^{14}C) study in the semiconfined Fontainebleau Sands Aquifer (France)". In: *Water Resources Research* 43.3 (2007).

[16] Gholam A. Kazemi, Jay H. Lehr, and Pierre Perrochet. *Groundwater age.* John Wiley & Sons, 2006.

[17] H. H. Loosli, H. Oeschger, and W. Wiest. "Argon 37, argon 39, and krypton 81 in the atmosphere and tracer studies based on these isotopes". In: *Journal of Geophysical Research (1896-1977)* 75.15 (1970), pp. 2895–2900. DOI: `https://doi.org/10.1029/JC075i015p02895`. eprint: `https://agupubs.onlinelibrary.wiley.com/doi/pdf/10.1029/JC075i015p02895`. URL: `https://agupubs.onlinelibrary.wiley.com/doi/abs/10.1029/JC075i015p02895`.

[18] *Isotope Methods for Dating Old Groundwater.* Non-serial Publications. Vienna: INTERNATIONAL ATOMIC ENERGY AGENCY, 2013. ISBN: 978-92-0-137210-9. URL: `https://www.iaea.org/publications/8880/isotope-methods-for-dating-old-groundwater`.

[19] Florian Ritterbusch. "Dating of groundwater with Atom Trap Trace Analysis of ^{39}Ar". PhD Thesis. Universität Heidelberg, 2013.

[20] R. Purtschert, R. Yokochi, W. Jiang, Z.-T. Lu, P. Mueller, J. Zappala, E. Van Heerden, E. Cason, M. Lau, T.L. Kieft, C. Gerber, M.S. Brennwald, and T.C. Onstott. "Underground production of 81Kr detected in subsurface fluids". In: *Geochimica et Cosmochimica Acta* 295 (2021), pp. 65–79. ISSN: 0016-7037. DOI: `https://doi.org/10.1016/j.gca.2020.11.024`. URL: `https://www.sciencedirect.com/science/article/pii/S0016703720306992`.

[21] Donald Porcelli. *Noble gases in geochemistry and cosmochemistry.* 1. Auflage. 2002.

[22] P. Collon, M. Bichler, J. Caggiano, L. Cecil, Y. El Masri, R. Golser, C.L. Jiang, A. Heinz, D. Henderson, W. Kutschera, et al. "Development of an AMS method to study oceanic circulation characteristics using cosmogenic ^{39}Ar". In: *Nuclear Instruments and Methods in Physics Research Section B: Beam Interactions with Materials and Atoms* 223 (2004), pp. 428–434.

[23] J. R. Tuniz, Claudio Tuniz, John R. Bird, Gregory F. Herzog, D. Fink, Tuniz Tuniz, W. Kutschera, and D. Fink Bird. *Accelerator Mass Spectrometry - Ultrasensitive Analysis for Global Science.* Boca Raton, Fla: CRC Press, 1998. ISBN: 978-0-849-34538-8.

[24] H.H. Loosli, M. Möll, H. Oeschger, and U. Schotterer. "Ten years low-level counting in the underground laboratoryin in Bern, Switzerland". In: *Nuclear Instruments and Methods in Physics Research Section B: Beam Interactions with Materials and Atoms* 17.5-6 (1986), pp. 402–405.

[25] W.M. Smethie, H.G. Ostlund, and H.H. Loosli. "Ventilation of the deep Greenland and Norwegian seas: evidence from krypton-85, tritium, carbon-14 and argon-39". In: *Deep Sea Research Part A. Oceanographic Research Papers* 33.5 (1986), pp. 675–703. ISSN: 0198-0149. DOI: `https://doi.org/10.1016/0198-0149(86)90060-9`. URL: `https://www.sciencedirect.com/science/article/pii/0198014986900609`.

[26] P. Collon, W. Kutschera, H.H. Loosli, B.E. Lehmann, R. Purtschert, A. Love, L. Sampson, D. Anthony, D. Cole, B. Davids, et al. "^{81}Kr in the Great Artesian Basin, Australia: a new method for dating very old groundwater". In: *Earth and Planetary Science Letters* 182.1 (2000), pp. 103–113.

[27]   Z. Feng, P. Bohleber, S. Ebser, L. Ringena, M. Schmidt, A. Kersting, P. Hop-kins, H. Hoffmann, A. Fischer, W. Aeschbach, and M. K. Oberthaler. "Dating glacier ice of the last millennium by quantum technology". In: *Proceedings of the National Academy of Sciences* 116.18 (2019), pp. 8781–8786. ISSN: 0027-8424. DOI: `10.1073/pnas.1816468116`. eprint: `https://www.pnas.org/content/116/18/8781.full.pdf`. URL: `https://www.pnas.org/content/116/18/8781`.

[28]   S. Ebser, A. Kersting, T. Stöven, Z. Feng, L. Ringena, Maximilian Schmidt, T. Tanhua, W. Aeschbach, and M.K. Oberthaler. "^{39}Ar dating with small samples provides new key constraints on ocean ventilation". In: *Nature Communications* 9.5046 (2018).

[29]   Pablo Woelk, Markus Kohler, and Klaus Sengstock. *Detection of nuclear re-processing activities using Kr-85*. Talk. online `https://inis.iaea.org/search/search.aspx?orig_q=RN:50010342`; 30.03.2021.

[30]   Jie Li, Zhonghe Pang, Guo-Min Yang, Jiao Tian, Amin L. Tong, Xiang-Yang Zhang, and Shui-Ming Hu. "Million-year-old groundwater revealed by krypton-81 dating in Guanzhong Basin, China". In: *Science Bulletin* 62.17 (2017), pp. 1181–1184. ISSN: 2095-9273. DOI: `https://doi.org/10.1016/j.scib.2017.08.009`. URL: `https://www.sciencedirect.com/science/article/pii/S2095927317304073`.

[31]   P. S. Light, R. D. Glover, M. A. Dakka, G. Tsiminis, A. J. Palmer, D. Chetty, I. Litvinyuk, R. T. Sang, and A. N. Luiten. "Towards an Australian Atom-Trap Trace Analysis (ATTA) facility". In: *AOS Australian Conference on Optical Fibre Technology (ACOFT) and Australian Conference on Optics, Lasers, and Spectroscopy (ACOLS) 2019*. Ed. by Arnan Mitchell and Halina Rubinsztein-Dunlop. Vol. 11200. International Society for Optics and Photonics. SPIE, 2019, pp. 15–16. DOI: `10.1117/12.2541232`. URL: `https://doi.org/10.1117/12.2541232`.

[32]   I. D. Moore, K. Bailey, J. Greene, Z.-T. Lu, P. Müller, T. P. O'Connor, Ch. Geppert, K. D. A. Wendt, and L. Young. "Counting Individual ^{41}Ca Atoms with a Magneto-Optical Trap". In: *Phys. Rev. Lett.* 92 (15 Apr. 2004), p. 153002. DOI: `10.1103/PhysRevLett.92.153002`. URL: `https://link.aps.org/doi/10.1103/PhysRevLett.92.153002`.

[33]   David R. Lide. *Handbook of Chemistry and Physics*. CRC Press, 2004. ISBN: 0-8493-0485-7.

[34]   H.H. Loosli. "A dating method with ^{39}Ar". In: *Earth and Planetary Science Letters* 63.1 (1983), pp. 51–62.

[35] Sven Ebser. "Optimierung und Stabilisierung von ^{39}Ar-ATTA bis hin zur erstmaligen Anwendung auf die Datierung natürlicher Wasserproben". Diploma Thesis. Universität Heidelberg, 2012.

[36] *Krypton-85 for the detection of plutonium production.* Website. online `https://www.znf.uni-hamburg.de/en/forschung/nuklearwaffenkontrolle/krypton-85.html`; 22.03.2021.

[37] Frank von Hippel, David H. Albright, and Barbara G. Levi. "Stopping the Production of Fissile Materials for Weapons". In: *Scientific American* 253.3 (1985), pp. 40–47. ISSN: 00368733, 19467087. URL: `http://www.jstor.org/stable/24967786`.

[38] *Krypton clue to North Korean nuclear progress.* online article. online `https://www.newscientist.com/article/dn3960-krypton-clue-to-north-korean-nuclear-progress/`; 21.07.2003.

[39] Martin B. Kalinowski, Hartmut Sartorius, Stefan Uhl, and Wolfgang Weiss. "Conclusions on plutonium separation from atmospheric krypton-85 measured at various distances from the Karlsruhe reprocessing plant". In: *Journal of Environmental Radioactivity* 73.2 (2004), pp. 203–222. ISSN: 0265-931X. DOI: `https://doi.org/10.1016/j.jenvrad.2003.09.002`. URL: `https://www.sciencedirect.com/science/article/pii/S0265931X03002534`.

[40] B.A. Fries. "Krypton-85. A versatile tracer for industrial process applications". In: *The International Journal of Applied Radiation and Isotopes* 28.10 (1977), pp. 829–832. ISSN: 0020-708X. DOI: `https://doi.org/10.1016/0020-708X(77)90022-9`. URL: `https://www.sciencedirect.com/science/article/pii/0020708X77900229`.

[41] Kelly Jones, Mike Harvey, and Tracey Anderson. *Assessment of the Radiological Impact of the Recycling and Disposal of Light Bulbs containing tritium, krypton-85 and radioisotopes of thorium.* June 2011. DOI: `10.13140/RG.2.2.11960.34561`.

[42] R. Purtschert, R. Yokochi, W. Jiang, Z.-T. Lu, P. Mueller, J. Zappala, E. Van Heerden, E. Cason, M. Lau, T.L. Kieft, C. Gerber, M.S. Brennwald, and T.C. Onstott. "Underground production of 81Kr detected in subsurface fluids". In: *Geochimica et Cosmochimica Acta* 295 (2021), pp. 65–79. ISSN: 0016-7037. DOI: `https://doi.org/10.1016/j.gca.2020.11.024`. URL: `https://www.sciencedirect.com/science/article/pii/S0016703720306992`.

[43] N. C. Sturchio, X. Du, R. Purtschert, B. E. Lehmann, M. Sultan, L. J. Patterson, Z.-T. Lu, P. Müller, T. Bigler, K. Bailey, T. P. O'Connor, L. Young, R. Lorenzo, R. Becker, Z. El Alfy, B. El Kaliouby, Y. Dawood, and A. M. A. Abdallah. "One million year old groundwater in the Sahara revealed by krypton-81 and chlorine-36". In: *Geophysical Research Letters* 31.5 (2004).

DOI: https://doi.org/10.1029/2003GL019234. eprint: https://agupubs.onlinelibrary.wiley.com/doi/pdf/10.1029/2003GL019234. URL: https://agupubs.onlinelibrary.wiley.com/doi/abs/10.1029/2003GL019234.

[44]   Christo Buizert, Daniel Baggenstos, Wei Jiang, Roland Purtschert, Vasilii V. Petrenko, Zheng-Tian Lu, Peter Müller, Tanner Kuhl, James Lee, Jeffrey P. Severinghaus, and Edward J. Brook. "Radiometric 81Kr dating identifies 120,000-year-old ice at Taylor Glacier, Antarctica". In: *Proceedings of the National Academy of Sciences* 111.19 (2014), pp. 6876–6881. ISSN: 0027-8424. DOI: 10.1073/pnas.1320329111. eprint: https://www.pnas.org/content/111/19/6876.full.pdf. URL: https://www.pnas.org/content/111/19/6876.

[45]   Marlan O. Scully and M. Suhail Zubairy. *Quantum Optics*. 6th ed. Cambridge: Cambridge University Press, 2008.

[46]   Harold J. Metcalf and Peter van der Straten. *Laser Cooling and Trapping*. Springer, 2012.

[47]   Wolfgang Demtröder. *Experimentalphysik 3*. Springer, 2010.

[48]   Hermann Haken and Hans Christoph Wolf. *Atom- und Quantenphysik. Einführung in die experimentellen und theoretischen Grundlagen*. ger. Achte, aktualisierte und erweiterte Auflage. Springer-Lehrbuch. Mit 307 Abbildungen, 32 Tabellen, 177 Aufgaben und vollständigen Lösungen. Berlin ; Heidelberg: Springer, 2004, XX, 531 Seiten. ISBN: 3-540-02621-5 and 978-3-540-02621-1 and 978-3-642-62142-0. DOI: 10.1007/978-3-642-18519-9.

[49]   B.H. Bransden and C.J. Joachain. *Physics of Atoms and Molecules*. 01. Aufl. Amsterdam: Pearson Education, 2003. ISBN: 978-0-582-35692-4.

[50]   Christoph Kaup. "Single-Atom Detection of ^{39}Ar". Diploma Thesis. Universität Heidelberg, 2011.

[51]   Joachim Welte. "Atom Trap Trace Analysis of ^{39}Ar". PhD Thesis. Universität Heidelberg, 2011.

[52]   Zhongyi Feng. "Quantum technological dating of glacier ice from the last millennium and a new self-contained facility for routine measurements". PhD Thesis. Universität Heidelberg, 2018.

[53]   Jake C. Zappala. "Atom Trap Trace Analysis: Developments and Applications". PhD Thesis. University of Chicago, 2017.

[54]   Jeremias Gutekunst. "Towards the realization of a laser system for cooling and trapping of ^{85}Kr and ^{83}Kr for Atom Trap Trace Analysis". Bachelor Thesis. Universität Heidelberg, 2020.

[55]   Florian Ritterbusch. "Realization of a collimated beam of metastable atoms for ATTA of Argon 39". Diploma Thesis. Universität Heidelberg, 2009.

[56] Markus Kohler. "Vakuum-Ultra-Violette-Lichtquelle und Konzeption für die Ultraspurenanalyse von seltenen Kryptonisotopen". PhD Thesis. Universität Hamburg, 2011.

[57] Michael E. Wieser Michael Berglund. "Isotopic compositions of the elements 2009 (IUPAC Technical Report)". In: *Pure and Applied Chemistry* 83.2 (2011), pp. 397–410.

[58] L Young, D Yang, and R W Dunford. "Optical production of metastable krypton". In: *Journal of Physics B: Atomic, Molecular and Optical Physics* 35.13 (June 2002), pp. 2985–2992. DOI: `10.1088/0953-4075/35/13/311`. URL: `https://doi.org/10.1088/0953-4075/35/13/311`.

[59] Xu Du. "Realization of Radio-Krypton Dating with an Atom Trap". PhD Thesis. Northwestern University, 2003.

[60] J. R. Brandenberger. "Landé g_J values in atomic argon: A measurement of the ratio $g_J(2p_9)/g_J(1s_5)$ by saturation spectroscopy". In: *Phys. Rev. A* 60 (2 Aug. 1999), pp. 1336–1340. DOI: `10.1103/PhysRevA.60.1336`. URL: `https://link.aps.org/doi/10.1103/PhysRevA.60.1336`.

[61] Jack Sugar and Arlene Musgrove. "Energy Levels of Krypton, Kr I through Kr XXXVI". In: *Journal of Physical and Chemical Reference Data* 20.5 (1991), pp. 859–915. DOI: `10.1063/1.555896`. eprint: `https://doi.org/10.1063/1.555896`. URL: `https://doi.org/10.1063/1.555896`.

[62] A. Klein, B.A. Brown, U. Georg, M. Keim, P. Lievens, R. Neugart, M. Neuroth, R.E. Silverans, L. Vermeeren, and ISOLDE Collaboration. "Moments and mean square charge radii of short-lived argon isotopes". In: *Nuclear Physics A* 607.1 (1996), pp. 1–22. ISSN: 0375-9474. DOI: `https://doi.org/10.1016/0375-9474(96)00192-3`. URL: `https://www.sciencedirect.com/science/article/pii/0375947496001923`.

[63] Włodzimierz Makulski. "83Kr nuclear magnetic moment in terms of that of 3He". In: *Magnetic Resonance in Chemistry* 52.8 (), pp. 430–434. DOI: `https://doi.org/10.1002/mrc.4083`. eprint: `https://onlinelibrary.wiley.com/doi/pdf/10.1002/mrc.4083`. URL: `https://onlinelibrary.wiley.com/doi/abs/10.1002/mrc.4083`.

[64] M. Keim, E. Arnold, W. Borchers, U. Georg, A. Klein, R. Neugart, L. Vermeeren, R.E. Silverans, and P. Lievens. "Laser-spectroscopy measurements of 72–96Kr spins, moments and charge radii". In: *Nuclear Physics A* 586.2 (1995), pp. 219–239. ISSN: 0375-9474. DOI: `https://doi.org/10.1016/0375-9474(94)00786-M`. URL: `https://www.sciencedirect.com/science/article/pii/037594749400786M`.

[65] B Ohayon and G Ron. "New approaches in designing a Zeeman Slower". In: *Journal of Instrumentation* 8.02 (Feb. 2013), P02016–P02016. DOI: 10.1088/1748-0221/8/02/p02016. URL: https://doi.org/10.1088/1748-0221/8/02/p02016.

[66] Sven Ebser. "Dating of Ice and Ocean Samples with Atom Trap Trace Analysis of ^{39}Ar". PhD Thesis. Universität Heidelberg, 2018.

[67] Bahaa E. A. Saleh and Marvin Carl Teich. *Fundamentals of Photonics*. 2nd ed. Wiley, 2007.

[68] E. A. Donley, T. P. Heavner, F. Levi, M. O. Tataw, and S. R. Jefferts. "Double-pass acousto-optic modulator system". In: *Review of Scientific Instruments* 76.6 (2005), p. 063112. DOI: 10.1063/1.1930095. URL: https://doi.org/10.1063/1.1930095.

[69] Christopher C. Davis. *Lasers and Electro-Optics, Fundamentals and Engineering*. Cambridge University Press, 2014.

[70] K. Różański. "Krypton-85 in the atmosphere 1950–1977: a data review". In: *Environment International* 2.3 (1979), pp. 139–143. ISSN: 0160-4120. DOI: https://doi.org/10.1016/0160-4120(79)90071-0. URL: https://www.sciencedirect.com/science/article/pii/0160412079900710.

[71] Andreas Bollhöfer, Clemens Schlosser, Sabine Schmid, Martina Konrad, Roland Purtschert, and Roman Krais. "Half a century of Krypton-85 activity concentration measured in air over Central Europe: Trends and relevance for dating young groundwater". In: *Journal of Environmental Radioactivity* 205-206 (2019), pp. 7–16. ISSN: 0265-931X. DOI: https://doi.org/10.1016/j.jenvrad.2019.04.014. URL: https://www.sciencedirect.com/science/article/pii/S0265931X19300888.

[72] Xiang-yang Zhang, Zhong-yu Chen, Guo-min Yang, Le-yi Tu, and Shui-ming Hu. "Krypton-85 dating of shallow aquifer in Hebei Plain". In: *Journal of Groundwater Science and Engineering* 4 (2016), pp. 328–332.

[73] Arne Kersting, Sofia Brander, and Axel Suckow. "Modelling 85Kr datasets with python for applications in tracer hydrology and to investigate atmospheric circulation". In: *MethodsX* 8 (2021), p. 101245. ISSN: 2215-0161. DOI: https://doi.org/10.1016/j.mex.2021.101245. URL: https://www.sciencedirect.com/science/article/pii/S2215016121000388.

[74] A. Kersting, C. Schlosser, A. Bollhöfer, and A. Suckow. "Evaluating 5 decades of atmospheric 85Kr measurements in the southern hemisphere to derive an input function for dating water and ice with implications for interhemispheric circulation and the global 85Kr emission inventory". In: *Journal of Environmental Radioactivity* 225 (2020), p. 106451. ISSN: 0265-931X. DOI: https:

//doi.org/10.1016/j.jenvrad.2020.106451. URL: https://www.sciencedirect.com/science/article/pii/S0265931X20306974.

[75] Yannis Arck. "Development of a Krypton Separation Setup for Dating with Atom Trap Trace Analysis". Master Thesis. Universität Hamburg, 2019.

[76] Maurus Hans. "Optisches Pumpen zur Erhöhung der Dichte von metastabilem Argon in einer RF-Gasentladung". Bachelor Thesis. Universität Heidelberg, 2014.

[77] Anika Frölian. "Optisches Pumpen über das transiente 2p6-Niveau zur Erhöhung der Dichte von metastabilem Argon in einer RF-Gasentladung". Bachelor Thesis. Universität Heidelberg, 2015.

[78] Lisa Ringena. "Optimization of ^{39}Ar-ATTA with new Laser System and a Double-Frequency Magneto-Optical Trap". Master Thesis. Universität Heidelberg, 2016.

[79] Zhongyi Feng. "Observation and Characterization of the Bichromatic Force on Metastable Argon-40". Master Thesis. Universität Heidelberg, 2014.

[80] Z. Feng, S. Ebser, L. Ringena, F. Ritterbusch, and M. K. Oberthaler. "Bichromatic force on metastable argon for atom-trap trace analysis". In: *Phys. Rev. A* 96 (1 July 2017), p. 013424. DOI: 10.1103/PhysRevA.96.013424. URL: https://link.aps.org/doi/10.1103/PhysRevA.96.013424.

[81] L. Ricci, M. Weidemüller, T. Esslinger, A. Hemmerich, C. Zimmermann, V. Vuletic, W. König, and T.W. Hänsch. "A compact grating-stabilized diode laser system for atomic physics". In: *Optics Communications* 117.5 (1995), pp. 541–549. ISSN: 0030-4018. DOI: https://doi.org/10.1016/0030-4018(95)00146-Y. URL: https://www.sciencedirect.com/science/article/pii/003040189500146Y.

[82] C. J. Hawthorn, K. P. Weber, and R. E. Scholten. "Littrow configuration tunable external cavity diode laser with fixed direction output beam". In: *Review of Scientific Instruments* 72.12 (2001), pp. 4477–4479. DOI: 10.1063/1.1419217. eprint: https://doi.org/10.1063/1.1419217. URL: https://doi.org/10.1063/1.1419217.

[83] Arno Trautmann. "Feshbach Spectroscopy of Sodium and Sodium-Lithium Mixtures". Diploma Thesis. Universität Heidelberg, 2011.

[84] Matthias Henrich. "Design and Realization of a Laser System for ATTA of Argon 39". Diploma Thesis. Universität Heidelberg, 2010.

[85] *Toptica: Products: Laser Diodes*. Website. online https://www.toptica.com/products/laser-diodes/; 15.02.21.

[86] Y. Xiong, S. Murphy, J.L. Carlsten, and K. Repasky. "Design and characteristics of a tapered amplifier diode system by seeding with continuous-wave and mode-locked external cavity diode laser". In: *Optical Engineering* 45.12 (2006), pp. 124205–124205.

[87] Florian Nicolai. "Design and construction of a fiber-coupled tapered amplifier system". Master Thesis. Universität Heidelberg, 2017.

[88] T.J. Hall, R. Jaura, L.M. Connors, and P.D. Foote. "The photorefractive effect—a review". In: *Progress in Quantum Electronics* 10.2 (1985), pp. 77–146. ISSN: 0079-6727. DOI: `https://doi.org/10.1016/0079-6727(85)90001-1`. URL: `https://www.sciencedirect.com/science/article/pii/0079672785900011`.

[89] *Eospace component handling*. Personal communication. via mail, 05.08.2020.

[90] J. C. Zappala, K. Bailey, Z.-T. Lu, T. P. O'Connor, and W. Jiang. "Note: Efficient generation of optical sidebands at GHz with a high-power tapered amplifier". In: *Review of Scientific Instruments* 85.4 (2014), p. 046104. DOI: `10.1063/1.4870412`.

[91] Gabriele Ferrari, Marc-Oliver Mewes, Florian Schreck, and Christophe Salomon. "High-power multiple-frequency narrow-linewidth laser source based on a semiconductor tapered amplifier". In: *Opt. Lett.* 24.3 (Feb. 1999), pp. 151–153. DOI: `10.1364/OL.24.000151`. URL: `http://ol.osa.org/abstract.cfm?URI=ol-24-3-151`.

[92] Arne Kersting. "Dating of groundwater and ocean sampleswith noble gas radioisotopes –sample preparation and field applications". PhD Thesis. Universität Heidelberg, 2018.

[93] Stefan Beyersdorfer. "Argon extraction from glacier ice andocean water for dating with ^{39}Ar - ATTA". Master Thesis. Universität Heidelberg, 2016.

[94] J. C. Zappala, K. Bailey, P. Mueller, T. P. O'Connor, and R. Purtschert. "Rapid processing of 85Kr/Kr ratios using Atom Trap Trace Analysis". In: *Water Resources Research* 53.3 (2017), pp. 2553–2558. DOI: `https://doi.org/10.1002/2016WR020082`. eprint: `https://agupubs.onlinelibrary.wiley.com/doi/pdf/10.1002/2016WR020082`. URL: `https://agupubs.onlinelibrary.wiley.com/doi/abs/10.1002/2016WR020082`.

[95] A.G.M. Ferreira and L.Q. Lobo. "The sublimation of argon, krypton, and xenon". In: *The Journal of Chemical Thermodynamics* 40.12 (2008), pp. 1621–1626. ISSN: 0021-9614. DOI: `https://doi.org/10.1016/j.jct.2008.07.023`. URL: `https://www.sciencedirect.com/science/article/pii/S0021961408001778`.

[96] D. Acosta-Kane, R. Acciarri, O. Amaize, M. Antonello, B. Baibussinov, M. Ceolin, C.J. Ballentine, R. Bansal, L. Basgall, A. Bazarko, et al. "Discovery of underground Argon with low level of radioactive ^{39}Ar and possible applications to WIMP dark matter detectors". In: *Nuclear Instruments and Methods in Physics Research Section A: Accelerators, Spectrometers, Detectors and Associated Equipment* 587.1 (2008), pp. 46–51.

[97] Niccolò Rigi-Luperti. "Inverstigation and improvement of metastable Argon densities in a helical resonator driven plasma for the ArTTA experiment". Bachelor Thesis. Universität Heidelberg, 2020.

[98] Kenneth Rudinger, Zheng-Tian Lu, and Peter Mueller. "The role of carrier gases in the production of metastable argon atoms in a rf discharge". In: *Review of Scientific Instruments* 80.3 (2009), p. 036105. DOI: 10.1063/1.3105722.

[99] Mark Csele. *Fundamentals of Light Sources and Lasers, Chapter 3 Notes*. Website. online http://archive.is/pwve; 09.05.2021.

Acknowledgments